UNIVERSITY OF ALBERTA

LNAPL MIGRATION AND TRAPPING IN HETEROGENEOUS POROUS MEDIA

by

Tannis Lynn Marie Sharp ©

A thesis submitted to the Faculty of Graduate Studies and Research in partial fulfillment of the requirements for the degree of Master of Science.

DEPARTMENT OF EARTH AND ATMOSPHERIC SCIENCES

Edmonton, Alberta

Fall, 2001

National Library of Canada
Acquisitions and Bibliographic Services
395 Wellington Street
Ottawa ON K1A 0N4
Canada

Bibliothèque nationale du Canada
Acquisitions et services bibliographiques
395, rue Wellington
Ottawa ON K1A 0N4
Canada

Your file Votre référence

Our file Notre référence

The author has granted a non-exclusive licence allowing the National Library of Canada to reproduce, loan, distribute or sell copies of this thesis in microform, paper or electronic formats.

L'auteur a accordé une licence non exclusive permettant à la Bibliothèque nationale du Canada de reproduire, prêter, distribuer ou vendre des copies de cette thèse sous la forme de microfiche/film, de reproduction sur papier ou sur format électronique.

The author retains ownership of the copyright in this thesis. Neither the thesis nor substantial extracts from it may be printed or otherwise reproduced without the author's permission.

L'auteur conserve la propriété du droit d'auteur qui protège cette thèse. Ni la thèse ni des extraits substantiels de celle-ci ne doivent être imprimés ou autrement reproduits sans son autorisation.

0-612-69593-X

Canada

UNIVERSITY OF ALBERTA

LIBRARY RELEASE FORM

NAME OF AUTHOR: TANNIS LYNN MARIE SHARP

TITLE OF THESIS: LNAPL MIGRATION AND TRAPPING IN HETEROGENEOUS POROUS MEDIA

DEGREE: MASTER OF SCIENCE

YEAR THIS DEGREE GRANTED: 2001

Permission is hereby granted to the University of Alberta Library to reproduce single copies of this thesis and to lend or sell such copies for private, scholarly or scientific research purposes only.

The author reserves all other publication and other rights in association with the copyright in the thesis, and except as hereinbefore provided neither the thesis nor any substantial portion thereof may be printed or otherwise reproduced in any material form whatever without the author's prior written permission.

(Signed) Tannis Sharp

Tannis Lynn Marie Sharp
#204-10808-84 Avenue
Edmonton, Alberta
CANADA, T6E 2J2

Date: Sept 25/01

UNIVERSITY OF ALBERTA

FACULTY OF GRADUATE STUDIES AND RESEARCH

The undersigned certify that they have read, and recommend to the Faculty of Graduate Studies and Research for acceptance, a thesis entitled **LNAPL Migration and Trapping in Heterogeneous Porous Media** submitted by **Tannis Lynn Marie Sharp** in partial fulfillment of the requirements for the degree of Master of Science.

Dr. Carl Mendoza

Dr. Ben Rostron

Dr. Kevin Biggar

Date: 25 Sept 2001

Abstract

Migration and trapping of light non-aqueous phase liquids (LNAPLs) in heterogeneous porous media was examined using two two-dimensional finite-element numerical models, with partial to full hysteresis. Modelling LNAPL migration in the Nordegg fractured sandstone aquifer necessitated modifications to the conceptual model to allow for numerical implementation. Results illustrate LNAPL is constrained in the fracture network by capillarity. Migration occurs both up and down dip, spreading laterally and vertically away from the source. The Hermite Collocation method employed cannot accurately represent three-phase flow in fractured porous media.

Porous media simulations illustrate LNAPL migrating laterally along the water table, and spreading vertically downward as the water table falls. The water table properties affect the extent of lateral and vertical migration, and subsequently the trapped distribution. Lenses are shown to act as either capillary barriers or sinks for LNAPL, depending on the contrast between water saturation across the lens interface.

Acknowledgements

Firstly, I would like to thank Dr. Carl Mendoza for all his support and assistance through the process of my Master's program. I certainly could not have completed this program without your aid and encouragement. Thank you to Dr. Kevin Biggar for your time and feedback on my thesis and to Dr. Ben Rostron, for the inspiration to enter the field of hydrogeology, all those years ago in Saskatoon, and for the support, focus, and encouragement you've provide through this process.

I would like to thank all the hydrogeology group at the University of Alberta: Melody, Darlene, Jenn, Heather I., Dan, Trevor, and Brian for their support and friendship. And a special appreciation to Kristine and Heather v. for the moral support, listening to complaints, and editing. Thank you to Brent for the reassurance and aid in completing my thesis and moving from student life into a professional career.

And finally, I must thank my parents and sister for the lifetime of support and encouragement. You always have faith that I can accomplish anything I set my mind to.

TABLE OF CONTENTS

Chapter 1 Introduction 1

1.1 Research Objectives 2

1.2 LNAPLs in Fractured Porous Media 3

1.3 LNAPLs in Porous Media 6

1.4 Literature Review 8

1.4.1 Behaviour of LNAPL in Fractured Aquifers 8

1.4.2 Light Non-Aqueous Phase Liquids in Porous Media 9

1.4.3 Water Table Fluctuations 10

1.4.4 Dense Non-Aqueous Phase Liquids in Fractured Porous Media 12

Chapter 2 Theoretical Development 16

2.1 Capillarity 16

2.2 Multiphase Flow Formulation 18

2.3 Mass Continuity 19

2.4 Constitutive Relationships 20

2.4.1 Capillary Pressure and Saturation 20

Dimensionless Capillary Pressure *22*

Three-Phase Capillary Pressure and Saturation *23*

2.4.2 Relative Permeability and Saturation 24

Three Phase Relative Permeability *25*

2.4.3 Treatment of Trapped Fluid Phases 26

2.4.4 Hysteresis 27

Capillary Pressure-Saturation *28*

Relative Permeability-Saturation *31*

2.5 Treatment of Fracture and Fracture Networks 32

2.5.1 Equivalent Porous Media 33

2.5.2 Dual Porosity 34

2.5.3 Discrete Fracture Models 35

2.6 Numerical Model Specifics 37

2.6.1 NAPL Simulator 37

2.6.2 MOFAT 38

Chapter 3 LNAPL Migration in Fractures 40

3.1 Nordegg Gas Plant 40

3.2 Numerical Implementation 42
3.2.1 Dimensionality 42
3.2.2 Fracture Sets 42
3.2.3 Fracture Property Representation 43
Permeability and Porosity 43
Capillary Pressure Curve 44
3.2.4 Matrix Properties 45
3.2.5 Aspect Ratio 46

3.3 Base Case Simulations 50
3.3.1 Grid Discretization 50
3.3.2 Boundary Value Problem 50
3.3.3 Base Case Properties 52

3.4 Results 56
3.4.1 Drainage 56
3.4.2 Injection 56
3.4.3 Redistribution 62
3.4.4 Mass Balance Issues 64

3.5 Numerical Model Issues 66

3.6 Summary 68

Chapter 4 Heterogeneous Porous Media Simulations **69**

4.1 Base Case Simulation 70
4.1.1 Grid Discretization 70
4.1.2 Boundary Value Problem 70
4.1.3 Initial Water Distribution 72
4.1.4 Porous Media Properties 73
4.1.5 Infiltration and Initial Redistribution Phase 77
4.1.6 Falling Water Table 80
4.1.7 Trapped LNAPL Distribution 82

4.2 Sensitivity Analysis 85
4.2.1 Numerical Model: NAPL Simulator 85
Initial Water Distribution 85
Infiltration 87
Redistribution 87
4.2.2 Non-Zero Residual Water Saturation 92
Initial Water Distribution 92
Results 93
4.2.3 Water Table Gradient 96
4.2.4 Water Table Fluctuation 98
4.2.5 Heterogeneity 101

Fine-Grained Lens *104*
Coarse-Grained Lenses *110*

4.3 Discussion 113
Heterogeneity Implications *114*
Direction of Water Table Fluctuation *115*
Repetitive Cycles of Water Table Fluctuation *116*

CHAPTER 5 Conclusions and Recommendations **117**

Recommendations 122

References **123**

TABLE OF FIGURES

Chapter 1 Introduction

1.1 LNAPL behaviour in fracture network subjected to water table fluctuations 5

1.2 Conceptual model of LNAPL migration in heterogeneous porous media system.....7

Chapter 2 Theoretical Development

2.1 Schematic empirical drainage relationships for capillary pressure-saturation 22

2.2 Hysteretic capillary pressure-saturation curves. 29

2.3 Relative permeability-saturation curves for primary drainage and imbibition.....32

Chapter 3 LNAPL Migration in Fractures

3.1 Block diagram of aquifer/aquitards at Nordegg Gas Plant. 41

3.2 Fracture LNAPL-water capillary pressure-saturation curve.....45

3.3 Node numbering and fracture orientation.....47

3.4 Convergence behaviour for rotated and non-rotated grid simulations.....49

3.5 Convergence for equal grid spacing simulations, original NAPL Simulator 49

3.6 Boundary value problem for LNAPL migration in fractured aquifer.....51

3.7 Capillary pressure-saturation curves, base case.....54

3.8 Relative permeability-saturation curves, base case 55

3.9 Water saturations prior to LNAPL injection.....57

3.10 LNAPL distribution in fracture network during injection, 5000 seconds 58

3.11 LNAPL distribution in fracture network during injection, 10,000 seconds 60

3.12 LNAPL distribution in fracture network after injection, 20,000 seconds.....61

3.13 LNAPL distribution across fracture plane at injection location, 20,000 seconds.....62

3.14 LNAPL distribution in fracture network after redistribution, 100,000 seconds.....63

3.15 LNAPL mass balance error during redistribution period, NAPL Simulator.....65

Chapter 4 Heterogeneous Porous Media Simulations

4.1 Boundary value problem for base case model.....71

4.2 Initial water distribution base case simulation, x = 20 m.....72

4.3 Capillary pressure-saturation curves, base case model.....75

4.4 Relative permeability-saturation curves, base case model.....76

4.5 Base case simulation, LNAPL and water saturations.....78, 79

4.6 Base case simulation, breakdown of trapped LNAPL distribution.....81

4.7 Base case simulation, trapped LNAPL distribution.....83, 84

4.8 Initial water distribution for NAPL Simulator case.....86

4.9 NAPL Simulator results, LNAPL and water saturations.....88, 89

4.10 Comparison between base case results and NAPL Simulator results, 25 days.....90

4.11 Comparison between base case results and NAPL Simulator results, 45 days.....91

4.12 Initial water distribution residual water saturations of 0.2 case.....93

4.13 Comparison between base case and residual saturation of 0.2, 25 days.....94

4.14 Comparison between base case and residual saturation of 0.2, 45 days.....95

4.15 Comparison between base case and flat water table, 45 days.....97

4.16 Comparison between base case and stable water table, 25 days.....99

4.17 Comparison between base case and stable water table, 45 days.....100

4.18 Orientation of gravity and capillary force vectors adjacent to lenses.....102

4.19 Capillary pressure-saturation curve, fine and coarse-grained materials 105
4.20 Comparison between base case and fine-grained lens, 45 days.....106
4.21 Fine-grained lens far above the water table, LNAPL and water saturation.....108
4.22 Initial water distribution: lenses.....109
4.23 Coarse-grained lens near the water table, LNAPL and water saturation.....111
4.24 Coarse-grained lens high above the water table, LNAPL and water saturation.....112
4.25 Differential upward movement of the water saturated region 116

TABLE OF TABLES

Table 3.1 van Genuchten parameters for water-gas capillary pressure-saturation ...45
Table 3.2 Base Case Properties, LNAPL migration in fractured aquifer 53
Table 4.1 Base Case Properties, LNAPL migration in porous media..... 74

FLOW NOTATION

k	permeability	$[L^2]$	m^2
ϕ	porosity	$[L^3]/[L^3]$	-
μ	viscosity	$[M]/[LT]$	$N{\cdot}s/m^2$
ρ	density	$[M]/[L^3]$	kg/m^3
g	gravity	$[L]/[T^2]$	m/s^2
P	fluid pressure	$[M]/[LT^2]$	N/m^2
Q	volumetric flux	$[L^3]/[T]$	m^3/s
q	darcy flux	$[L^3]/[T]/[L^2]$	$m^3/s/m^2$
v	average linear velocity	$[L^3]/[T]/[L^2]$	$m^3/s/m^2$
R_e	reynolds number	-	-
d	characteristic length scale	$[L]$	m
S	fluid saturation	$[L^3]/[L^3]$	-
t	time	$[T]$	s or d
r	effective pore radius	$[L]$	m
b	fracture aperture	$[L]$	m
Δx, Δy, Δz	grid discretization in 3 directions	$[L]$	m
x	x coordinate	$[L]$	m
y	y coordinate	$[L]$	m
z	z-coordinate	$[L]$	m
h_{pw}	water pressure head, boundary condition	$[L]$	m

CAPILLARY PRESSURE-SATURATION-RELATIVE PERMEABILITY NOTATION

k_r	relative permeability	-	-
θ	contact angle	-	-
σ	interfacial tension	$[M]/[LT^2]$	N/m^2
P_C	capillary pressure	$[M]/[LT^2]$	N/m^2
P_d	displacement pressure	$[M]/[LT^2]$	N/m^2
P'_C	dimensionless capillary pressure	-	-
a	van Genuchten scaling parameter	[L]	m
n	van Genuchten scaling parameter	-	-
m	van Genuchten scaling parameter	-	-
λ	Brooks-Corey pore size distribution index	-	-
S_{Wr}	residual water saturation	$[L^3]/[L^3]$	-
S_{Nr}	residual NAPL saturation	$[L^3]/[L^3]$	-
S_{Nnr}	residual NAPL as non-wetting phase	$[L^3]/[L^3]$	-
S_{Nwr}	residual NAPL as -wetting phase	$[L^3]/[L^3]$	-
S_{Gr}	residual gas saturation	$[L^3]/[L^3]$	-
S_{Nt}	trapped NAPL saturation	$[L^3]/[L^3]$	-
S_{Wt}	trapped water saturation	$[L^3]/[L^3]$	-
$\bar{S}$	effective saturation	$[L^3]/[L^3]$	-
$\bar{\bar{S}}$	apparent saturation	$[L^3]/[L^3]$	-

SUBSCRIPTS

α	phase subscript, refers to water, gas, or NAPL
D	drainage
I	imbibition
ij	two coordinate directions
n	non-wetting phase
w	wetting phase
W	water phase
N	NAPL phase
G	gas phase
T	total wetting phase, water + NAPL
GN	gas-NAPL
NW	NAPL-water
GW	gas-water
r	residual
t	trapped

SUPERSCRIPTS

max	maximum
min	minimum

Chapter 1

Introduction

Subsurface contamination by non-aqueous phase liquids (NAPLs) is a pervasive problem throughout the industrialised world. Dense non-aqueous phase liquids (DNAPLs), such as chlorinated solvents, and light non-aqueous phase liquids (LNAPLs), such as natural gas condensate, have a significant negative impact on the quality of shallow groundwater and surface water resources. As a result, substantial research activity is being devoted to their study (Mayer et al., 1995). NAPLs are unique subsurface contaminants because their low aqueous solubilities cause them to remain in the subsurface for long periods of time, acting as sources for dissolved phase contamination, which in turn will move with the natural groundwater flow. NAPLs may also vapourize and migrate in the unsaturated zone. Furthermore, many NAPL constituents are highly toxic, having drinking water standards many orders of magnitude lower than their solubility limits. As such, NAPL contaminants present a distinct problem in the subsurface as contaminant mass is transported in the free phase, dissolved phase, and vapour phase (Mercer and Cohen, 1990). Each mechanism of transport is dominated by different gradients, resulting in discrete flow fields for the dissolved phase, free phase, and vapour phase in the subsurface.

LNAPLs are free-phase contaminants with densities less than water. As a result, these contaminants will float on and depress the water table, and migrate along the water table. Consequently, the location of the water table through time is critical in understanding

LNAPL migration and trapping behaviour. Seasonal or artificially induced changes in the water table elevation will move the free-phase contaminants in the subsurface, spreading them both vertically and laterally.

Migrating free-phase NAPL leaves a trail of immobile, or residual, fluid behind. This residual NAPL is effectively trapped in portions of the pore space, where it can partition to the aqueous and/or vapour phases. The presence of heterogeneities, be they lenses, layers or fractures, complicates these transport mechanisms, and results in substantially different free-phase and residual-phase contaminant distributions compared to homogeneous porous media situations. In saturated formations, fractures and high permeability lenses act as conduits, causing non-aqueous fluids to bypass much of the pore volume. Lower permeability lenses act as barriers, diverting the NAPL. Fractures in particular allow large vertical columns of NAPL to develop from relatively small volumes of released NAPL, causing deep penetration into the subsurface and potentially large plumes of dissolved contamination.

Analysis of LNAPL flow and transport problems in the unsaturated zone are further complicated by the presence of three separate fluid phases: NAPL, water, and air. The presence of these multiple fluid phases complicates flow within a homogeneous medium and the presence of lenses or fractures adds significant complexity to the problem. Heterogeneities may act as either conduits or barriers when three active phases are present in the domain, contrary to the behaviour in water saturated conditions discussed above. The conceptual models for LNAPL migration and trapping behaviour in fractured and heterogeneous porous media are discussed below.

1.1 Research Objectives

This study addresses the free-phase migration and trapping behaviour of LNAPL contaminants in groundwater systems subjected to water table fluctuations. The objectives of the project are to use numerical models to:

- examine LNAPL migration and trapping in the subsurface;

- evaluate the impacts of lowering water table conditions, including initial water table location;
- evaluate the effect of water table gradients; and,
- assess the influence of heterogeneities (fractures and lenses) on migration and trapping.

A particular case, fashioned after documented field evidence of LNAPL infiltration and migration within a fracture network, is examined. Numerical modelling of LNAPL migration in a fracture network incorporating three-phase hysteretic flow has not been reported in the literature to date. Conclusions are drawn regarding the numerical difficulty ant the extensive simplifications required of modelling such a problem, as well as the applicability of the selected numerical model. Consequently, simpler cases of fine and coarse-grained lenses located in porous media are examined with two numerical models. Conclusions are drawn regarding the importance of water table fluctuations, water table gradient, lens permeability relative to surrounding porous media, and lens location relative to water table elevation. The results show that the distribution of free-phase and residual-phase contaminants is highly dependent on the above factors, which has significant implications for free-phase, dissolved-phase, and vapour-phase migration, and for remediation programs.

1.2 LNAPLs in Fractured Porous Media

The case of LNAPL contamination in fractured porous media is one of the numerous conceptual models for subsurface contamination by NAPLs. Unlike porous media situations, free-phase migration of LNAPL is expected to be much less dependent on the water table gradient in fracture networks. Rather, the magnitude and frequency of water table fluctuations, fracture properties (*e.g.*, aperture, roughness, degree of contact), and fracture network properties (*e.g.*, orientation, spacing, and interconnectedness) are the dominant controls (Hardisty, 1996).

A conceptual model, presented in Figure 1.1, predicts that following a surface spill of LNAPL, the free-phase contaminant will migrate down through the unsaturated zone, confined within fractures, under the effects of gravity (Figure 1.1a). Vertical migration occurs most effectively through large-aperture, sub-vertical fractures (Hardisty, 1996). As long as the LNAPL column remains connected to the source area, the pressure at the leading edge of the plume will continue to increase as LNAPL migrates further into the subsurface. Thus, fractures with smaller and smaller apertures can be invaded as the depth of penetration increases. Migration of LNAPL through fractures in the unsaturated zone is analogous to DNAPL migration through saturated fractures.

Once the LNAPL reaches the top of the saturated zone, it begins to depress the water table, until resisting forces balance the forces driving the LNAPL deeper, similar to LNAPL behaviour in porous media. The force acting to drive LNAPL further below the water table is the weight of the column of LNAPL above. Forces resisting deeper migration are buoyancy (due to differences in fluid densities) and the fracture entry pressure. The capillary pressure between the LNAPL and water phases is a maximum at the water table. It decreases downwards through the water column to the fracture entry pressure at the leading edge of the LNAPL stringer (Hardisty, 1996).

Reinitiation of migration will occur when the natural variations in regional recharge cause the water table to move. A decrease in the elevation of the water table, Figure 1.1b, will cause deeper vertical migration of the LNAPL. When the water table stabilizes some distance below its initial position, the LNAPL will be able to penetrate further below the new water table elevation as a result of the increased LNAPL pressure head.

As the water table subsequently rises (Figure 1.1c) LNAPL within the saturated zone is driven upwards through the fractures. On encountering fracture intersections, the LNAPL can enter previously uninvaded subhorizontal fractures. In this way, lateral migration of LNAPL occurs, independent of the water table gradient. Beneath the water table, LNAPL within sub-horizontal fractures can be isolated at mobile saturations, illustrated as black fracture segments beneath water table in 1.1c. Further changes in the

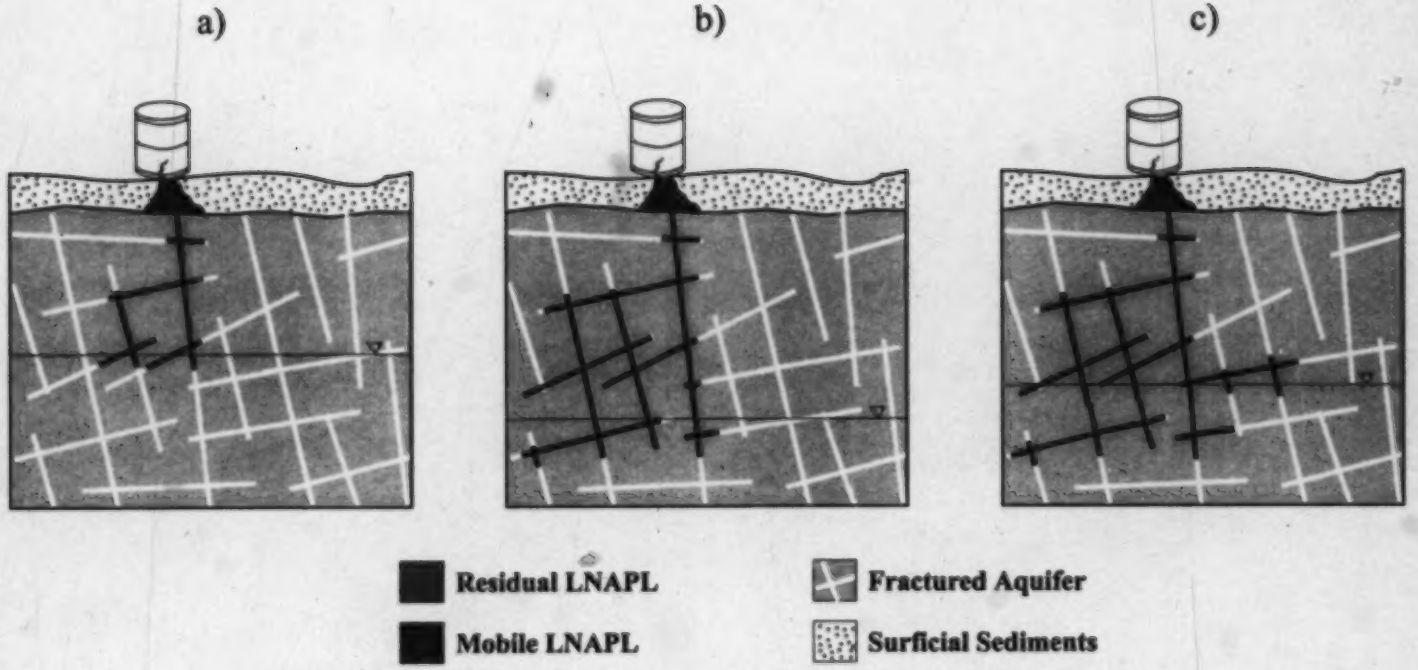

Figure 1.1. LNAPL behaviour in fracture network subjected to fluctuating water table conditions: a) Initial pattern of LNAPL infiltration into fracture network; b) LNAPL distribution as a result of dropping water table conditions; c) LNAPL distribution as a result of subsequent water table rising.

pressure regime caused by pumping or lowering of the water table can remobilize these trapped blobs.

1.3 LNAPLs in Porous Media

The free-phase migration of LNAPL contaminants in homogeneous porous media and porous media containing lenses is different from the situation presented above for fractured porous media. In this situation, the porous media properties and water table fluctuations are still important, but the water table gradient is also crucial.

A conceptual model for the migration of LNAPL in a domain containing lenses subjected to water table fluctuations is shown in Figure 1.2. Once a spill occurs, LNAPL infiltrates from the ground surface, downwards through the unsaturated zone, Figure 1.2a. Lenses present can act as either conduits or barriers to migration. In Figure 1.2a, a clay lens is illustrated to act as a barrier, diverting the LNAPL along the upper interface and down the sides. Depending on the water table location, this lens could also act as a sink for LNAPL migration with respect to the surrounding medium. Once the LNAPL encounters the water table, it depresses the water saturated region, forms a pool, and migrates down gradient (Abdul, 1988). A zone of trapped LNAPL is illustrated to develop (grey shaded area in Figure 1.2a) once the source region is depleted, and the LNAPL has drained from the pores, leaving an immobile residual saturation.

Dropping of the water table, Figure 1.2b, causes the LNAPL to again migrate vertically, as well as laterally. The region previously containing mobile LNAPL has drained, and a larger region of trapped LNAPL saturation forms (Fetter, 1999). The vertically migrating LNAPL encounters a sand lens, which, in this scenario, acts as a conduit for LNAPL migration. The LNAPL is funnelled through the sand lens and pools at its base, prior to re-entering the silt. Once in the silt, the LNAPL front migrates downward to the water table, and again depresses the water saturated region, pools, and migrates laterally down gradient.

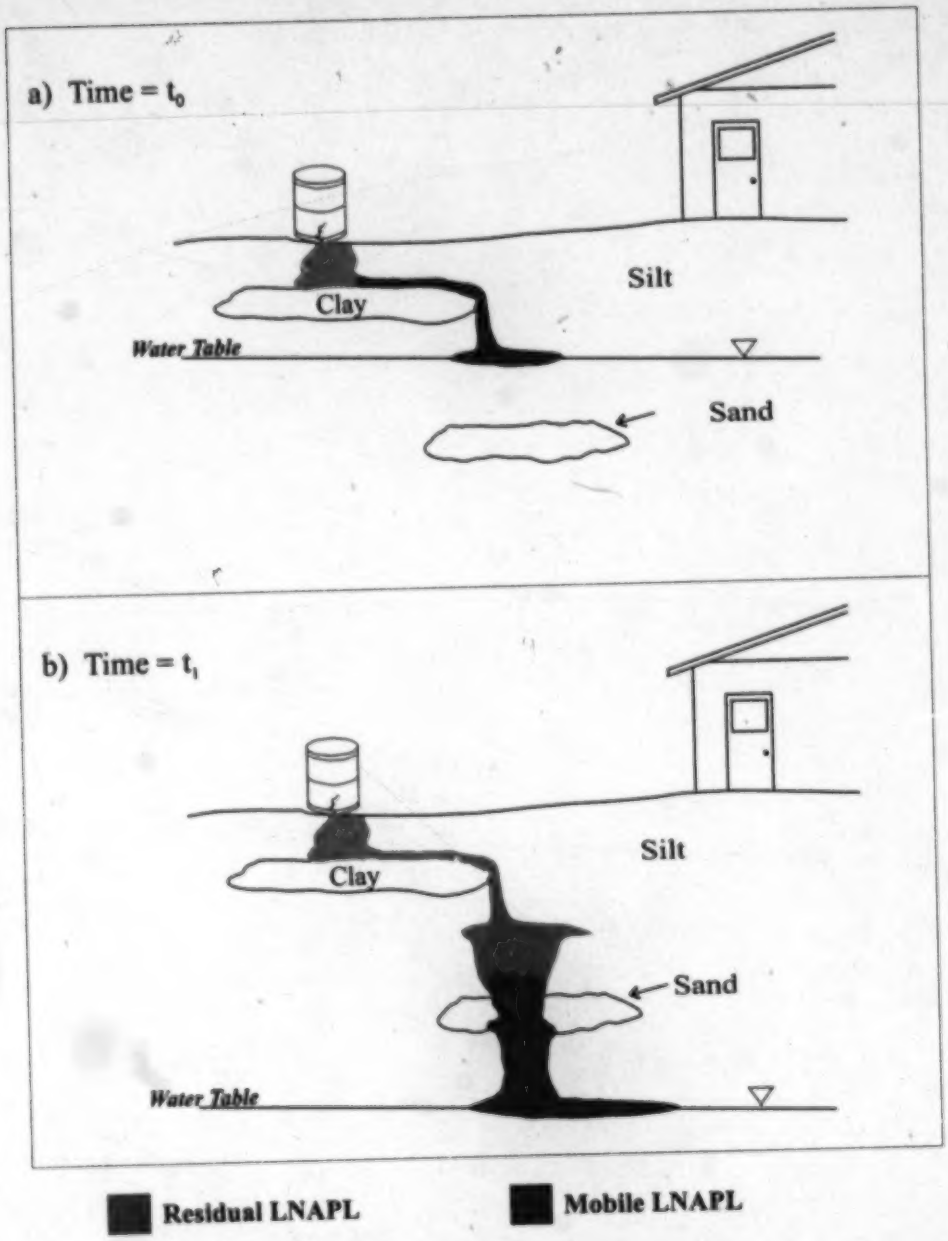

Figure 1.2 Conceptual model of LNAPL migration in porous media heterogeneous system: a) from point source to the water table; b) subsequently subjected to a dropping water table.

The water saturation of lenses, controlled by the capillary pressure-saturation relationship, and their lateral and vertical positions, is crucial in the predicted LNAPL migration pathway and trapped LNAPL profile. Trapping of LNAPL as an immobile phase is controlled by the interplay of these heterogeneities with the characteristics of the source and naturally induced water table fluctuations. Correctly understanding the interplay of these factors is central to an accurate representation of flow behaviour at a contaminated site.

1.4 Literature Review

Numerous aspects of research in contaminant hydrogeology and petroleum engineering are relevant to the study of LNAPL migration and trapping in porous and fractured porous media. Although relatively little research has been conducted into the problem of light non-aqueous phase liquids in fractured aquifers, LNAPLs in porous media have been studied extensively. Of particular focus in this literature review is three-phase experimental and field studies, hysteresis, water table fluctuations and heterogeneity. DNAPL migration in fractured media is also addressed.

1.4.1 Behaviour of LNAPL in Fractured Aquifers

Work by Hardisty (1996) and Hardisty et al. (1993; 1995; 1994a; 1994b; 1998) appears to constitute the majority of published research on the problem of LNAPL migration in fractured, near surface aquifers. Hardisty (1996) was the first to propose a conceptual model for LNAPL migration in fractured rock based on field investigations made at the Nordegg Gas Plant in Nordegg, Alberta. This LNAPL conceptual model incorporates the significant influences of groundwater table fluctuations on the distribution of contaminant, but does not include the effects of capillarity or spatial variation in fracture properties.

Field studies by David et al. (1999) of a gasoline spill in a fractured sedimentary bedrock setting found that LNAPL was primarily constrained to the fractures, and that much of the surrounding mudstone matrix contained no LNAPL. Free-phase flow was concluded

to occur through sub-vertical fractures and sandy laminae within the matrix. Vacuum enhanced recovery techniques were employed to mitigate gasoline vapour accumulation and provide hydraulic containment. McCrory (1997) found that foliation within metamorphosed, folded, and faulted rock in the vicinity of a gasoline spill controlled the migration of free-phase product away from the spill site. The results of these studies show that relying on the slope of the potentiometric surface for predicting free-phase migration pathways resulted in erroneous assessments of LNAPL distributions.

1.4.2 Light Non-Aqueous Phase Liquids in Porous Media

A significant amount of research has been performed on the problem of light non-aqueous phase liquids in porous media, both within the hydrogeology field and the petroleum engineering field. The concepts of multiphase flow are equally applicable in both areas, although the relative importance of the various processes is slightly different.

Experiments by Abdul (1988) on the migration potential of oil through variably saturated media showed that the response of the capillary fringe and the water table depend on whether the water table is rising or falling. For small to medium spills in sandy material, oil would likely reach the capillary fringe and migrate laterally along the top. For larger spills in sandy material, the LNAPL would penetrate the capillary fringe to the water table and beneath. Conversely, in finer grained material, capillary forces are increased, and oil would likely pancake on the capillary fringe, even for large spill volumes.

Essaid et al. (1993) used a hysteretic capillary pressure–saturation numerical model to analyse a ten year old oil spill, where a detailed oil distribution had been determined using wells and soil cores. The three-phase relative permeability functions from Parker et al. (1987) were used. The oil body was laterally asymmetric with a very localized region in the centre where NAPL saturations exceeded 0.60. In this region, the water-saturated zone was significantly depressed, and the maximum oil saturations were found at the apparent water table (extrapolated elevation of the zero water pressure surface). Surrounding this core region was a large area where NAPL saturations were less than 0.20. Away from the core region, maximum NAPL saturations were found at the top of

the capillary fringe, indicating insufficient NAPL head to exceed the displacement pressure of the porous media. Numerical results illustrated the importance of incorporating hysteresis into the numerical solution – the large-scale features of the oil body could only be reproduced when hysteresis and heterogeneity were included. Their results show that the oil distribution is most sensitive to the spatial correlation structure of the permeability, capillary pressure versus saturation curves, and the mean permeability.

Oostrom and Lenhard (1998) used experimental data to examine the suitability of two capillary pressure-saturation-relative permeability parametric models (Brooks and Corey, (1964), and van Genuchten, (1980)) for LNAPL migration. They found that the Brooks and Corey model provided the best representation of the experimental data. The van Genuchten model over-estimated NAPL penetration speed and distance in the unsaturated and saturated regions; adding hysteresis to the van Genuchten model did not provide a substantially improved numerical result. These results were attributed to two factors. First, the lack of a definitive entry pressure in the van Genuchten parametric models means that the LNAPL pressure need only exceed the water pressure at a given point for LNAPL to continue migrating. Second, the two different pore-size distribution models used in the relative permeability functions showed that, for a given LNAPL saturation, the Brooks and Corey model always calculated a lower relative permeability to LNAPL.

Experimental work of Schroth et al. (1998) showed that infiltration of LNAPL into higher permeability lenses in the unsaturated zone is dependent on the water saturation in the lens. At low water saturations (less than 0.45) LNAPL was diverted along the sloping edge of the lens. Similar diversion behaviour was observed for lenses having water saturations exceeding 0.90. In the water saturation range of 0.45 to 0.90, LNAPL partially penetrated the coarser sand lens and was partially diverted along the sloping textural interface.

1.4.3 Water Table Fluctuations

Water table fluctuations are an extremely important component of many hydrogeologic systems, but are often ignored in analyses of LNAPL migration. In particular, fractured

systems can be especially sensitive to changes in the water budget because of contrasts in hydraulic properties between the fractures and matrix. Typically, the small pore size of the matrix causes much of it to remain saturated for a significant distance above the water table. Furthermore, the fracture porosity is small. Thus, for any given volume of recharge, the water table will rise much more dramatically than in porous media. The response time to recharge events is short due to the significant permeability of the fracture network.

In the case of a fractured aquifer contaminated by light non-aqueous phase liquids, water table fluctuations play a critical role in the migration of the contaminant. As the LNAPL sits on the water table, fluctuations force the NAPL up and down in the fracture network, acting as the forcing mechanism for lateral migration of the contaminant, constained by the fractures.

Research into the implications of water table fluctuation on fractured aquifers has been limited to that by Hardisty (1996); however, substantial work has been done on the water table fluctuations in LNAPL contaminated porous media. Kemblowski and Chiang (1990) proposed an inverse correlation between water table fluctuations and the product thickness in a well, based on field data and theoretical development. This inverse correlation was also observed in the fractured sandstone at a condensate spill (Hardisty, 1996). The two mechanisms proposed for this inverse correlation are trapping/remobilization of residual NAPL and short circuiting of the low permeability formation by the well. Remobilization and trapping of NAPL will occur in a fractured aquifer, but play a much more minor role than proposed for porous media (Hardisty, 1996).

Lenhard et al. (1993) experimentally analyzed trapping of NAPL due to water table fluctuations. They demonstrated trapped LNAPL saturations of 0.33 and LNAPL plus air saturations of 0.40 beneath the water table. They also showed that the trapping of both NAPL and air beneath the water table are reproducible through cyclic changes in water table elevation. White and Lenhard (1993) used a one-dimensional, three-phase

hysteretic numerical model to model the same experimental data. Their work showed that incorporating hysteresis, both in terms of nonwetting phase occlusion and differences in the imbibition and drainage saturations paths, was key to adequate calibration to the experimental data. The non-hysteretic numerical results predicted larger saturation responses to the water table movement than observed during the experimental phase.

Experimental results of Minssieux (1994) illustrate the importance of considering hysteresis during alternating rising and falling water tables in porous media, both in the two-phase air-water system and with residual NAPL present at approximately 0.25. Field studies of LNAPL behaviour above a fluctuating water table were carried out by Steffy et al. (1995). They found that a 1 m thick smeared zone of contamination developed at the site where the water table fluctuates 0.5 m over a year. Increases in NAPL pore pressure were observed in the formation two weeks before an increase in product thickness in the well, potentially as a result of low NAPL relative permeability. Over the course of the year, the well and formation were almost never in equilibrium, discounting previous work (Sullivan et al., 1988) that relies on the assumption of equilibrium. Steffy et al. (1995) also found markedly different NAPL profiles above rising and falling water tables. Above a falling water table, NAPL saturations increased with depth, to a maximum of 0.20 at the air-LNAPL interface. In contrast, above the rising water table, a relatively uniform NAPL saturation of 0.06 to 0.08 was observed.

Parker et al. (1991) used an areal flow model to simulate a site over a three-year period. Field data showed that water table fluctuations had a major influence on the distribution, migration, and recovery of the free-phase contaminant. Both recovery rates and NAPL spreading rates were decreased by the fluctuations. The amount of lateral spreading was found to be dependent on the gradient on the water table.

1.4.4 Dense Non-Aqueous Phase Liquids in Fractured Porous Media

The vast majority of research on NAPL migration in fractured rock has focused on the problem of dense non-aqueous phase liquids (DNAPL). Because of the dense nature and propensity to accumulate above low permeability strata (Kueper and McWhorter, 1991),

fractures present in these materials provide pathways to allow for deeper contamination. Prior to the mid 1980s, it was thought that low permeability aquitards would provide protection for deeper aquifers (Feenstra et al., 1996). However, there are cases where DNAPL has penetrated through numerous sequences of aquifers and aquitards (Feenstra et al., 1996). DNAPL compounds have been observed at several hundred metres depth, and it has been postulated that, given sufficient volumes, they could penetrate in excess of 1000 m (Feenstra et al., 1996). As with LNAPLs, the migration and ultimate distribution of the DNAPLs is controlled by fracture network properties or orientation and interconnectedness (Feenstra et al., 1996).

The main difference between DNAPL migration in fractured rock and LNAPL migration in fractured rock is that DNAPL problems generally involve only two phases, while LNAPL problems involve three phases. In addition, DNAPL migration does not show the same dependence on water table fluctuations. However, DNAPL migration studies are concerned with the constitutive relations for capillary pressure-saturation-relative permeability, the trapping of residual fluids, fracture network properties, and as a result can provide information for LNAPL studies.

Examining multiphase behaviour in individual fractures, rather than fracture networks, is the focus of most research (Kueper and McWhorter, 1996). Schwille (1988) performed the first physical experiments on DNAPL infiltration and migration through a single, partially water saturated fracture. These experiments demonstrated the importance of fracture roughness, or aperture variability. In the smooth fracture model, DNAPL migrated straight downwards as a thin core in both the unsaturated and saturated zones, with minor pooling at the capillary fringe. This is in contrast to the behaviour in the rough fracture, where the DNAPL migrated in broad, finely veined pathways, and significantly more residual was trapped. Lowering the water table was shown to cause trapped flecks to be remobilized as the top of the saturated zone dropped past them. Kueper and McWhorter (1991) present a derivation for the entry pressure of a single fracture aperture region, with a generalized overview of migration. A single fracture plane was modelled as a two-dimensional porous medium, using traditional porous media

capillary pressure versus saturation and relative permeability versus saturation constitutive relationships. Their work predicted a significant degree of channeling of DNAPL and water within the fracture as a result of the variable aperture distribution. Some regions of the fracture remained free of DNAPL for the entire simulation. Each fluid caused significant flow interference of the other fluid. Penetration of the DNAPL into regions of the fracture plane was shown to be controlled by the entry pressure at the advancing front. Results from this single fracture study were used to make generalized extrapolations of migration within fracture networks (Kueper and McWhorter, 1996).

Esposito and Thompson (1999) conducted numerical experiments on a single rough walled fracture to examine the influence that dissolution, transport, and matrix diffusion had on the flow of DNAPL within a single vertical rough-walled fracture. They used a numerical model that explicitly defines phase locations within the domain, eliminating the need for constitutive relations for capillary pressure, saturation, and relative permeability. For the given DNAPL properties, it was shown that during the period of DNAPL infiltration and equilibration, dissolution had little effect on the flow solution. As with the work of Kueper and McWhorter (1991), the distribution of DNAPL within the fracture was controlled by the aperture and capillary pressure at the advancing front.

Heise (1999) conducted similar numerical experiments using the multiphase flow formulation, constitutive relations and coupling between the flow and transport solutions in a single rough-walled fracture. For the given solubilities, the coupling between the flow and transport phenomena was found to be weak. The DNAPL distribution within the fracture was most sensitive to the NAPL density, the properties of the aperture field, and the initial water gradient over the fracture.

The use of numerical models to examine the DNAPL migration in fracture networks is relatively rare. Slough et al. (1999) examined the effects of matrix entry pressure on the migration and distribution of DNAPL within a fracture network, with specific emphasis on carbonate rocks. They showed that the matrix entry pressure significantly affected both the lateral and vertical distribution on DNAPL. High entry pressures caused most

DNAPL to be excluded from the matrix, increasing the volume and mobility of DNAPL within the fracture network, compared to the case of lower matrix entry pressure. They also showed that the hydraulic conductivity of the fracture network was most important in the total volume of DNAPL transmitted into the subsurface from a fixed pool at surface.

Chapter 2

Theoretical Development

The physics of subsurface LNAPL migration and trapping are complex. Consequently, representing these physical processes in a numerical model is difficult. This chapter presents a theoretical development of the important processes involved in, and controls on, LNAPL migration and trapping. The causes of capillarity and its relation to saturation and relative permeability, the origin and numerical treatment of hysteresis, and multiphase flow representation are presented. Subsequently numerous methods of representing fractures within numerical models are addressed. The two numerical models used in the study, MOFAT and NAPL Simulator, are presented and necessary modifications to the codes are outlined.

2.1 Capillarity

Leverett (1941) first discussed the theory of capillarity in porous media for static and dynamic problems. The theory is based on thermodynamic and physical principles. Along the interface between two immiscible fluids, a tension is present, causing the interface to contract to minimize the free surface energy. This tension, termed interfacial tension or surface tension, is a result of the imbalance between cohesive forces acting on fluid molecules on either side of the interface. A force balance along the curved interface

shows that, at equilibrium, a pressure difference must exist between two immiscible fluids (Corey, 1994). The fluid on the concave side of the interface is at a higher pressure than the fluid on the convex side. Within a porous medium this pressure difference is referred to as the capillary pressure, P_C:

$$P_C = P_n - P_w = \frac{2\sigma\cos\theta}{r} \tag{2.1}$$

where P_n is the pressure in the non-wetting phase; P_w is the pressure in the wetting phase; σ is the interfacial tension between the two phases; θ is the contact angle; and r is the effective pore radius. These terms are explained further below.

In the subsurface, the presence of the solid porous media further complicates the two-fluid system. An interfacial tension is present along the contact between any one fluid and the solid porous medium. Differences in the interfacial tensions for the each fluid phase and the solid result in the preferential coating of the solid by one of the fluids. This phenomenon is termed wettability, and is represented by the contact angle, θ, in Equation 2.1. The contact angle is the angle at which the fluid-fluid interface contacts the solid phase, measured through the denser phase. If the angle, measured through a given phase, is less than 70° that phase is the wetting phase. If the angle is greater than 120° the media is oil-wet. Contact angles between 70° and 120° represent intermediate wettability (Mercer and Cohen, 1990).

Usually in a two-phase system, water will preferentially coat the solid, and is the wetting phase. Air is typically the non-wetting fluid and is generally separated from the solid by a thin film of water. If a non-aqueous phase liquid is present, its wettability is generally found to be less than water, but more than air, termed intermediate wettability.

2.2 Multiphase Flow Formulation

The movement of each separate phase in the subsurface can be described by a modified version of Darcy's Law. Modifications are made to account for the reduced area for flow available for each phase caused by the presence of additional fluid phases in the pore space. This reduction in flow capacity is quantified by the relative permeability term, k_r, in Darcy's Law. Bear (1972) gives the generic flow equation for any phase, α, as:

$$q_{\alpha i} = -k_{r\alpha} \frac{k_{ij}}{\mu_\alpha} \left(\frac{\partial P_\alpha}{\partial x_j} + \rho_\alpha g \frac{\partial z}{\partial x_j} \right) \qquad i, j = 1,2,3 \qquad (2.2)$$

where α represents the phase of interest, water, gas, or NAPL (W,G, or N); q is the darcy flux in the i coordinate direction; k_r is the relative permeability; k_{ij} is the intrinsic permeability tensor; μ is the dynamic viscosity; P is the fluid pressure; x_j is the coordinate direction; ρ is the fluid density; g is the gravitational acceleration; and z is the vertical direction, defined as positive upwards.

The direct proportional relationship present in Darcy's Law between hydraulic gradient and Darcy flux becomes less valid as the volumetric flux increases. The limit for the applicability of Darcy's Law is based on the Reynolds number, R_e, the ratio of the inertial forces acting on the fluid to the viscous forces:

$$R_e = \frac{v d \rho}{\mu} \qquad (2.3)$$

where v is the average linear groundwater velocity (equal to q/ϕ, where ϕ is the porosity) and d is a characteristic length scale, often taken as some representative dimension of the grains (Bear, 1972). At Reynolds numbers below the range of 1 to 10 viscous forces are dominant, and Darcy's Law is valid. At higher Reynolds numbers flow becomes nonlinear and does not adhere to Darcy's Law because inertial forces become significant. At high enough Reynolds numbers flow can become turbulent. In typical groundwater settings, the natural groundwater velocities are sufficiently slow that Reynolds numbers

fall below the lower limit and Darcy's Law is valid. There are certain situations where non-Darcian flow in the subsurface is conceivable. These include karst aquifers, larger aperture fractures, and very rough fractures.

2.3 Mass Continuity

Within a domain of interest, conservation of mass must hold for each constituent of the system. The change in mass of a particular constituent over time within the representative elemental volume, REV, must equal the difference between the flow out and the flow in, plus any source or sink terms. Source/sink terms can be used to represent removal or injection from a well, partitioning to other phases, or degradation processes. Parker (1989) states the law of mass conservation for each fluid phase as:

$$\phi \frac{\partial \rho_\alpha S_\alpha}{\partial t} = -\frac{\partial \rho_\alpha q_{\alpha i}}{\partial x_i} + Q_\alpha \qquad i = 1,2,3 \qquad (2.4)$$

where ϕ is the effective porosity; S_α is the phase saturation; t is time; and Q_α is the source/sink term, as a mass flux. Each fluid phase must adhere to this mass continuity relationship. Mass conservation of the solid porous media is usually ensured by assuming incompressibility of the skeletal framework.

The Darcy flux for each phase in the above equation can be removed from consideration by substitution of Darcy's Law, Equation 2.2, into Equation 2.4, This results in the mass continuity equation for each phase:

$$\phi \frac{\partial \rho_\alpha S_\alpha}{\partial t} = \frac{\partial}{\partial x_i}\left[\rho_\alpha \frac{k_{r\alpha} k_{ij}}{\mu_\alpha}\left[\frac{\partial P_\alpha}{\partial x_j} + \rho_\alpha g \frac{\partial z}{\partial x_j} \right] \right] + Q_\alpha \qquad i,j = 1,2,3 \qquad (2.5)$$

The differential equations for each phase are coupled through the phase saturation conservation relationship and the capillary pressure definitions:

$$S_W + S_G + S_N = 1 \tag{2.6}$$

$$P_{C_{GW}} = P_G - P_W \tag{2.7}$$

$$P_{C_{NW}} = P_N - P_W \tag{2.8}$$

$$P_{C_{GN}} = P_G - P_N \tag{2.9}$$

where *W* represents the water phase; *N* represents the NAPL phase; and *G* represents the gas phase. In this formulation, the order of wettabiiity, from highest to lowest, is assumed to be water, then NAPL, and finally gas.

Additional constraints on the system are provided by constitutive relationships linking capillary pressure, saturation and relative permeability terms, as described in the following section.

2.4 Constitutive Relationships

Constitutive relationships provide a method of linking the fluid saturation to the capillary pressure and relative permeability. Initially, these relationships are considered from the viewpoint of two-phase primary drainage, where a non-wetting fluid invades into a wetting fluid-saturated media. Next three-phase concepts are outlined. Finally, hysteresis is considered, where flow directions change from drainage conditions to imbibition conditions. Imbibition is the term applied to the condition of a wetting fluid displacing a non-wetting fluid.

2.4.1 Capillary Pressure and Saturation

Capillary pressure at a given point is related to the saturation of each fluid. Equation 2.1 shows an inverse relationship between capillary pressure, P_C, and pore radii, r, or fracture aperture. Thus, as capillary pressure is increased, successively smaller pores can be invaded by the non-wetting fluid. Based on the pore size distribution for a given porous media, or the aperture distribution for a fracture, a relationship between capillary pressure and saturation can be determined. This constitutive relationship can be measured using

various methods, or, as is typical in hydrogeology, estimated through one of a number of empirical relationships. The two most common empirical relations used in hydrogeology are those of van Genuchten (1980) and Brooks and Corey (1964). Both methods use the concept of effective saturation. Effective saturations are used to scale the phase saturation values by the endpoints, or maximum saturation range possible, which is dependent on the residual saturation (van Genuchten, 1980; Brooks and Corey, 1964):

$$\overline{S}_a = \frac{S_a - S_m}{1 - S_m} \tag{2.10}$$

where $\overline{S}_a$ is the effective fluid saturation for the phase; S_a is the total saturation of phase; and S_m is the residual water saturation. The van Genuchten (1980) relationship for saturation as a function of capillary pressure, during the drainage process, is:

$$\overline{S}_a = \left[\frac{1}{1+(aP_C)^n}\right]^m \tag{2.11}$$

where a and n are fitting parameters and $m = \left(1 - \frac{1}{n}\right)$. The corresponding Brooks and Corey (1964) equation is:

$$\overline{S}_a = \left(\frac{P_C}{P_d}\right)^{-\lambda} \tag{2.12}$$

where λ is a fitting parameter, termed the pore-size distribution index; and P_d is the displacement pressure. The displacement pressure is a non-zero pressure difference that must be achieved for non-wetting phase to invade a porous medium occupied by wetting phase. Effectively, it represents the largest pore throat in the porous media.

Although these two relationships approximate the same phenomena, they have slightly different characteristics. The Brooks and Corey model has a distinct displacement pressure, P_d, as shown in Figure 2.1. In contrast, the van Genucthen model calculates a non-wetting phase saturation greater than 0 as soon as P_n exceeds P_w. This is the most critical distinction between these two mathematical models.

The Brooks and Corey model has been suggested to provided a better representation of the experimental data for LNAPL migration (Oostrom and Lenhard, 1998). In their experiments, the van Genuchten model over-estimated LNAPL penetration speed and distance in the unsaturated and saturated regions. One of the reasons for the inferior representation is the lack of a definitive entry pressure in the van Genuchten parametric model: the non-wetting phase pressure need only exceed the wetting phase pressure for invasion.

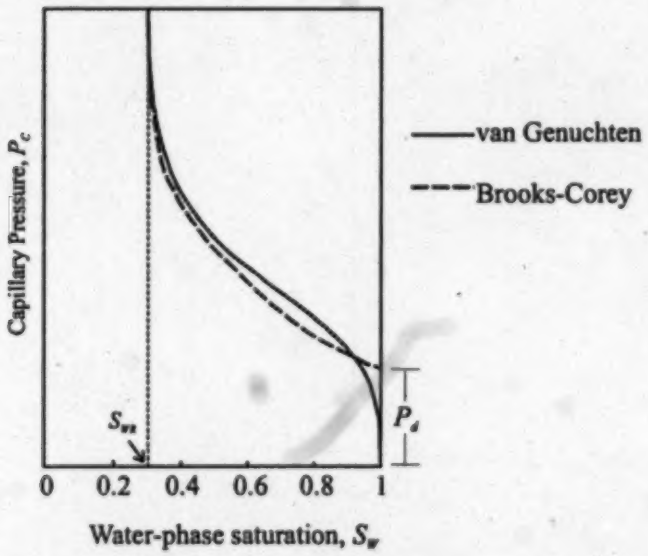

Figure 2.1. Schematic empirical drainage relationships for capillary pressure – saturation using van Genuchten and Brooks and Corey functions.

Dimensionless Capillary Pressure

Leverett (1941) found that when plotted in a dimensionless form, the capillary pressure-saturation curves for comparable porous media are similar. The capillary pressure relationship can then be scaled for different media and fluid pairs based on the

permeability, the porosity, and the interfacial tension through the use of a dimensionless capillary pressure, P'_C:

$$P'_C = \frac{P_C}{\sigma_{\alpha\beta}}\left(\frac{k}{\phi}\right)^{\tau} \tag{2.13}$$

where τ is dimensionally correct equal to 0.5 (Leverett, 1941). This concept is employed in the following section for three-phase capillary pressure-saturation relations.

Three-Phase Capillary Pressure and Saturation

The experimental determination of capillary pressure-saturation functional relationships for three-phase systems is extremely difficult and as such is rarely attempted. The reasons are two-fold. Firstly there are many more possible fluid displacement combinations; twelve possibilities compared to the two possibilities in the two-fluid system. Secondly, it is difficult to measure phase saturations and pressures in a three-phase system. The most common method producing a three-phase capillary pressure-saturation relationship in porous media is an extension of the two-phase systems, first proposed by Leverett (1941). It was shown by Leverett (1941) that the term for dimensionless capillary pressure, Equation 2.13, is equally applicable to LNAPL-water, water-gas, or gas-LNAPL fluid pairs.

Parker et al. (1987) presented a parametric model for three-phase capillary pressure-saturation-relative permeability for monotonic drainage based on the work of Leverett (1941) and the van Genucthen (1980) functional relationship. The model assumes that the water saturation in a three-phase system is dependent on the water-NAPL capillary pressure curve only:

$$\overline{S}_W = \left[\frac{1}{1+(a_{NW}P_{C_{NW}})^n}\right]^m \quad for \;\; P_{C_{NW}} > 0 \tag{2.14}$$

$$\overline{S}_W = 0 \quad for \;\; P_{C_{NW}} \le 0 \tag{2.15}$$

where the effective water saturation, $\overline{S}_W$, is defined as:

$$\overline{S}_W = \frac{S_W - S_{Wr}}{1 - S_{Wr}} \tag{2.16}$$

The second capillary pressure curve of interest is that for the gas-NAPL system. In a three phase setting, the total wetting saturation, the sum of NAPL and water saturations, is a function of the gas-NAPL curve.

$$\overline{S}_T = \left[\frac{1}{1+(a_{GN}P_{C_{GN}})^n}\right]^m \quad for\ P_{C_{GN}} > 0 \tag{2.17}$$

$$\overline{S}_T = 0 \quad for\ P_{C_{GN}} \leq 0 \tag{2.18}$$

where S_T refers to the total wetting saturation, as the sum of the water and LNAPL saturations; and the effective total wetting saturation, $\overline{S}_T$, is defined as:

$$\overline{S}_T = \frac{S_T - S_{Wr}}{1 - S_{Wr}} \tag{2.19}$$

The implicit assumption in the above equations is that water is most wetting, followed by NAPL, and then by gas. As a result, no interfaces between the water and gas phases exist until the NAPL phase goes to residual saturation. In the portions of the domain where NAPL is not present, Equation 2.17 is replaced with the two-phase term for water-gas capillary pressure, Equation 2.11. A single capillary pressure-saturation curve is often used in numerical models and scaled for the various phases through the interfacial tensions.

2.4.2 Relative Permeability and Saturation

The relative permeability term incorporated into the multiphase flow form of Darcy's Law, Equation 2.2, quantifies the influence of the reduced pore area available for flow of each individual phase, due to the presence of other fluids in the pore space. Relative

permeabilities range from 0.0 when no hydraulically connected fluid is present, to 1.0, when no other fluids are present to impede flow. Because the reduction in permeability is due to other fluids, the magnitude of the relative permeability term is tied to the saturation. This relationship can be measured experimentally, with difficulty. Numerous empirical relationships have been proposed for the continuous function in porous media. Again, the most common are Brooks and Corey (1964) and van Genuchten (1980). The van Genuchten (1980) expressions for wetting phase and non-wetting phase relative permeability, respectively, are:

$$k_{rw} = \bar{S}_w^{1/2}\left[1-(1-\bar{S}_w^{1/m})^m\right]^2 \tag{2.20}$$

$$k_{rn} = (1-\bar{S}_n)^{1/2}\left[1-(1-\bar{S}_n)^{1/m}\right]^{2m} \tag{2.21}$$

The corresponding Brooks and Corey (1964) expressions are:

$$k_{rw} = \bar{S}_w^{(2+3\lambda)/\lambda} \tag{2.22}$$

$$k_{rn} = \left(1-\bar{S}_n\right)^2 \cdot \left(1-\bar{S}_n^{(2+\lambda)/\lambda}\right) \tag{2.23}$$

Oostrom and Lenhard (1998) found that the Brooks and Corey model provided the best representation of the experimental data flow behaviour for the LNAPL phase. The van Genuchten model over-estimated NAPL penetration speed and distance in the unsaturated and saturated regions. One of the reasons for this difference is that two different pore-size distribution models were used in the relative permeability function derivations, and consequently the Brooks and Corey model will always calculate a lower relative permeability to LNAPL.

Three-Phase Relative Permeability

As with the capillary pressure-saturation relationship, laboratory measurements of three-phase relative permeability is difficult. Parker et al. (1987) presented a method for

estimating three phase relative permeabilities from two-phase system measurements, based on work by Leverett and Lewis (1941) and the van Genuchten (1980) formulation.

Water relative permeability in a three-phase system is generally taken as a function solely of the water saturation. Therefore, Equation 2.20, with the wetting phase, w, equal to water, W, is appropriate to determine the water relative permeability, k_{rW}. Gas relative permeability is also assumed to be strictly a function of the gas saturation, and Equation 2.21 is used, with n equal to G, to calculate gas relative permeability, k_{rG}. The NAPL relative permeability is a function of both the water and oil phase saturations (Katyal et al., 1991 and Guarnaccia et al., 1997):

$$k_{rN} = (\bar{S}_T - \bar{S}_W)^{1/2} \cdot \left\{ \left[1 - \bar{S}_W^{\,1/m} \right]^m - \left[1 - \bar{S}_T^{\,1/m} \right]^m \right\}^2 \qquad (2.24)$$

2.4.3 Treatment of Trapped Fluid Phases

Suitably representing the trapped saturation is important to represent the impact it has on fluid volumes and on the capillary pressure-saturation-relative permeability functions. Some studies have treated the trapped saturation, S_{at}, of some or all phases as a constant value, equal to the maximum residual saturation, S_{ar}. However, the trapped saturation should be dependent on the maximum amount of that phase that has been present in the pores, scaled as a function of maximum and current saturations (Guarnaccia et al., 1997). Land (1968) presented a method to calculate a scaled non-wetting phase trapped saturation at the end of the imbibition process:

$$\bar{S}_{Nt} = \frac{1 - \bar{S}_W^{\min}}{1 + R_{NW}\left(1 - \bar{S}_W^{\min}\right)} \qquad (2.25)$$

$$\text{where:} \quad R_{NW} = \frac{1}{S_{Nr}} - 1$$

All terms in the above equation are time and location dependent. In the above equation $\bar{S}_{Nt}$ is the calculated trapped oil saturation, $\bar{S}_W^{min}$ is the minimum water effective water saturation obtain, $\bar{S}_{Nr}$ is the maximum, theoretical residual oil saturation, assuming the drainage process ran to completion prior to imbibition.

This expression was modified by Kaluarachchi and Parker (1992) to account for trapping during the process of imbibition:

$$\bar{S}_{Nt}=\left\{\frac{1-\bar{S}_W^{min}}{1+R_{NW}(1-\bar{S}_W^{min})}\;\frac{1-\bar{\bar{S}}_W}{1+R_{NW}(1-\bar{\bar{S}}_W)}\right\}\quad for\ \bar{\bar{S}}_W>\bar{S}_W^{min} \tag{2.26}$$

$$\text{where:}\quad R_{NW}=\frac{1}{S_{Nr}}-1$$

where $\bar{\bar{S}}_W$ is the apparent water saturation, equal to the sum of the effective water saturation and the effective LNAPL saturation.

2.4.4 Hysteresis

The above constitutive relationships for capillary pressure-saturation-relative permeability are actually hysteretic, or path-dependent, in nature. This implies that the capillary pressure and relative permeability are dependent on the historical saturation pathway. With hysteresis, the capillary pressure (or relative permeability) at a given saturation is different depending on whether the LNAPL is entering an initially water saturated region (drainage) or if water is re-entering a region that is partially saturated with LNAPL (imbibition). Changes in the direction of NAPL migration caused by water table fluctuations make this an important factor in quantifying NAPL behaviour in the subsurface. As there are twelve possible flow path combinations, where each phase can either be undergoing imbibition or drainage, or remaining at a constant saturation, hysteresis is potentially much more significant in three-phase systems (Parker and Lenhard, 1987). Therefore ignoring hysteresis in three-phase systems is likely to produce greater errors.

Typically hysteresis is a concept that is ignored in numerical studies, as most models do not account for the complex process. Implementation of hysteresis in a numerical model requires a significant amount of bookkeeping in regards to the saturation histories of each phase at each nodal location. Lenhard and Parker (1987) and Parker and Lenhard (1987) developed a general theoretical method to determine hysteretic capillary pressure-saturation-relative permeability relations for two- and three-phase systems.

Capillary Pressure-Saturation

The two end member cases for displacement of fluids are primary drainage and primary imbibition (PDC and PIC, respectively, on Figure 2.2). Primary drainage refers to the non-wetting phase displacing the wetting phase out of a system initially saturated with wetting phase. Primary imbibition refers to wetting phase displacing the non-wetting phase out of a system initially saturated with non-wetting phase. These two curves are the upper and lower boundary curves for the capillary pressure versus saturation relationship. Between these two end-member curves are an infinite number of scanning curves, which describe the relationship when only partial imbibition or drainage occur prior to flow reversal. The main imbibition curve (MIC) describes the relation between capillary pressure and saturation when imbibition occurs after complete primary drainage occurs, and the wetting phase is reduced to residual saturation. The primary imbibition curve, PIC, describe the relation between capillary pressure and saturation when non-wetting phase initial saturates the porous media, and wetting-phase imbibes. With respect to NAPL contaminants in the subsurface, primary imbibition will likely never occur as the porous media will never contain 100% NAPL or 100% air, the two possible non-wetting phases.

For the drainage of wetting fluids there are three major reasons for the observed hysteresis in multiphase flow scenarios. These are: fluid entrapment, pore morphology, and differences in contact angle depending on the advancing fluid. Contact angle hysteresis occurs because the advancing angle is significantly larger that the receding angle, most likely because the properties of the solid surface are altered by the fluids

contacting it. This is a manifestation of surface roughness and immobility of fluids on a macromolecular scale on the solid surface (Dullien, 1992).

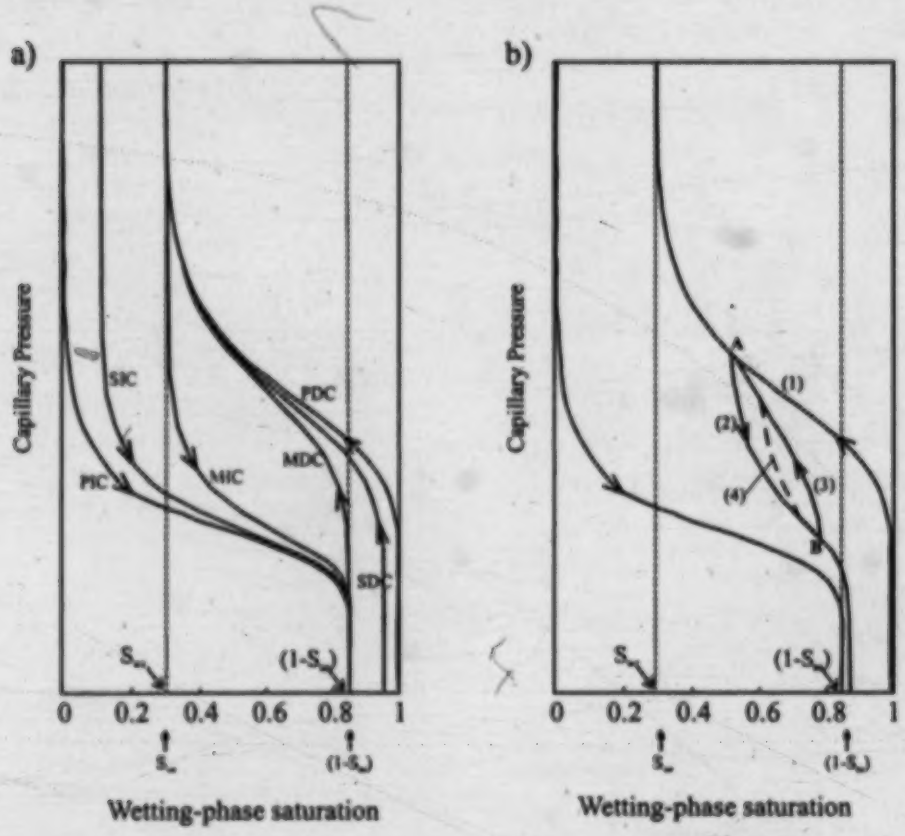

Figure 2.2 Hysteretic capillary pressure-saturation curves, showing the definition of drainage and imbibition; primary, secondary, and scanning curves. a) definition of curve types: PDC is the primary drainage curve, PIC is the primary imbibition curve, MDC and SDC are a main and secondary drainage curves, MIC and SIC are a main and secondary imbibition curves; b) illustration of scanning curve spawning, where (1) is the PDC and (2), (3), and (4) are scanning curves (after Guarnaccia et al., 1997).

Parker and Lenhard (1987) present a method to extend the three-phase capillary pressure-saturation algorithm to incorporate hysteresis instead of simply monotonic drainage. Within Equations 2.14 and 2.19 the scaling parameter, a, is treated as path dependent and two main values are specified, one for drainage, a_D, and one for imbibition, a_I. These two curves correspond to the PDC and PIC curves on Figure 2.2a, respectively.

In the hysteretic case, the functional relationship uses apparent saturations, rather than effective saturations. The apparent water saturation is the sum of the effective water saturation and the effective saturations of the phases trapped by water:

$$\overline{\overline{S}}_W = \overline{S}_W + \overline{S}_{Nt} + \overline{S}_{Gwt} \tag{2.26}$$

where $\overline{S}_{Gwt}$ is the effective saturation of gas trapped by the water phase.

The apparent total wetting phase saturation is equal to the sum of the effective water saturation, effective NAPL saturation, and effective saturation of gas trapped by the water and NAPL phases:

$$\overline{\overline{S}}_T = \overline{S}_W + \overline{S}_N + \overline{S}_{Gt} \tag{2.27}$$

The other modification required for a hysteretic solution is a procedure to move between drainage and imbibition curves as the flow conditions change. Scanning curves, illustrated in Figure 2.2b, are used. To illustrate, consider a case of primary drainage, moving along the PDC curve in Figure 2.2a and Line 1 in Figure 2.2b. At the point noted A, a flow reversal occurs from drainage conditions to imbibition conditions. Line 2 is a scanning curve, describing the capillary pressure-saturation behaviour as the non-wetting phase exits the pores. If a second flow reversal occurred at point B, Line 3 would be followed until the minimum wetting phase saturation reached during primary drainage is again obtained, at which point the primary drainage curve, PDC, Line 1 would be applied. An infinite number of scanning curves are possible, with the primary drainage

curve, PDC, as the theoretical upper boundary, and the primary imbibition, PIC, curve as the theoretical lower boundary.

Relative Permeability-Saturation

Hysteresis in the relative permeability-saturation relationship is derived from fluid entrapment effects (Lenhard and Parker, 1987). It is typically accounted for within the effective saturation terms. As a result, the three phase relative permeability terms, as shown in Equations 2.20, 2.21, and 2.24, are utilized in the hysteretic solution. Different implementations (Guarnaccia et al., 1997; Lenhard and Parker, 1987) use various definitions of effective and apparent saturations, such as Equation 2.16 or 2.26.

Figure 2.3 illustrates the relative permeability versus saturation curves for a two-phase, hysteretic situation. In Figure 2.3a the wetting phase relative permeability is displayed for the primary drainage curve, PDC, and the primary imbibition curve, PIC. The PDC curve originates at a wetting phase saturation of 1.0, with the corresponding wetting phase relative permeability of 1.0. The relative permeability drops off dramatically as the wetting phase saturations are decreased, approaching 0.0 at the residual wetting phase saturation, S_{wr}, for complete drainage. The relative permeability for the non-wetting fluid (PDC curve on Figure 2.3b) during primary drainage rises from 0.0 at a wetting phase saturation of 1.0 to something less than 1.0 at the residual wetting phase saturation, S_{wr}.

For the primary imbibition process, PIC, the relative permeability for the wetting phase (Figure 2.3a) and the relative permeability for the non-wetting phase (Figure 2.3b) show the opposite behaviour. The primary imbibition curve originates at a wetting phase saturation of 0.0, or non-wetting phase saturation of 1.0. The relative permeability for the non-wetting phase starts at 1.0 and drops to 0.0 at the residual non-wetting phase saturation. The relative permeability for the wetting phase starts at 0.0 and rises to something less than 1.0 at the residual non-wetting phase saturation.

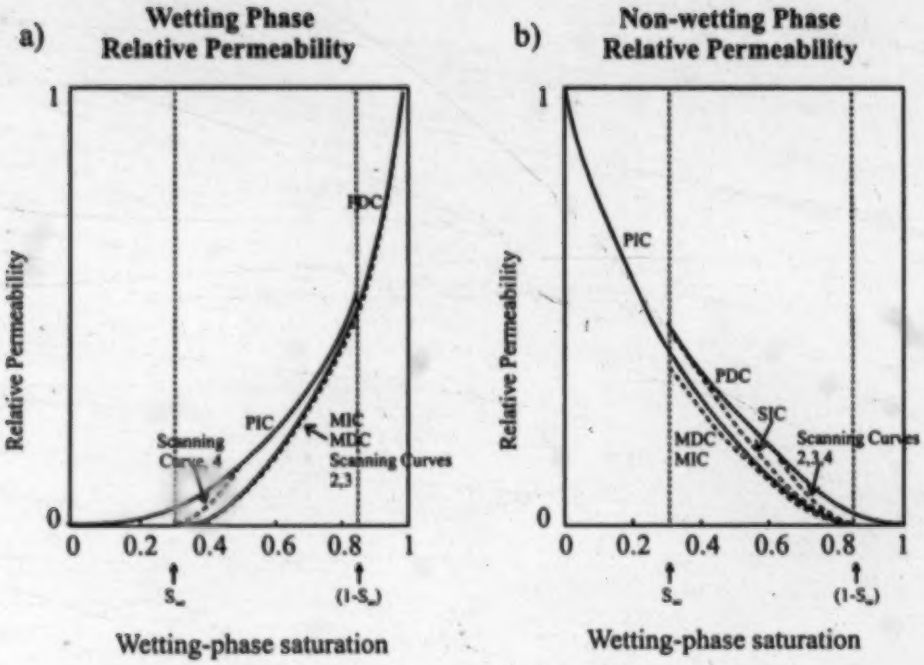

Figure 2.3. Relative permeability-saturation curves for primary drainage, PDC, and primary imbibition, PIC: a) for wetting phase; b) for non-wetting phase. Curve names and numbering is analogous to Figure 2.2 (after Guarnaccia et al., 1997).

2.5 Treatment of Fractures and Fracture Networks

Fractures are understood conceptually as roughly planar breaks in the rock mass of some random circular / elliptical shape. Their orientation changes over the fracture surface, but they can generally be described by some average strike and dip. Within a fracture network, there are sets of fractures with approximately similar orientations due to concurrent genesis. The fracture aperture can range over several orders of magnitude within a single plane but in some places the two sides of the fracture will be in contact.

It is extremely difficult to either measure fracture properties, to describe all fractures at a site in the above context, or to explicitly represent them within either a conceptual, analytical, or numerical model. One of the major challenges of working on fractured

sites is to adequately represent the fracture network without excessive information requirements. Numerous methods have been developed to aid in conceptualization of a fractured porous media. The choice of method depends on the scale of the problem, available data, computational time constraints, and characteristics of the various flow domains of interest. In general, methods require either gross simplification or detailed description of the aquifer properties (Andersson and Dverstorp, 1987). The commonly used methods are the equivalent porous media approach, dual porosity models, and discrete fracture models. Individual methods are also sometimes combined in a number of up-scaling stages to achieve a more realistic conceptual model for the problem and scale of interest (Andersson and Dverstorp, 1987).

2.5.1 Equivalent Porous Media

The equivalent porous media approach to simulating flow through fractured porous media represents the rock formation as a single continuum. The individual hydraulic properties, permeability and porosity, for the fracture and the matrix are replaced by a single set of hydraulic properties (and possible anisotropy to account for the directionality of the fracture network) that adequately represent the overall, or average, flow regime. Use of this method implies that a representative elementary volume (REV) can be defined. Such an REV will be large in comparison to any individual matrix block or fracture, but small in comparison with the domain of interest (Bear, 1993). Equivalent porous media methods are generally applied in regional scale models and where the fracture network is dense and extensive. Time scales of interest are usually long, so that averaging processes dominate over the discrete pathways of each fracture. These conditions are representative of the 'very far field' (Bear, 1993). Numerous researchers (*e.g.*, Long et al., 1982; Cacas et al., 1990a, 1990b) have noted the unacceptability for such methods at local scales. Long et al. (1982) demonstrated that as fracture density increases and larger sample sizes are considered, the equivalent porous media methods are more applicable. They also concluded that fractures with constant apertures and distributed orientations are more appropriate than aperture distributions and uniform orientations.

Multiphase flow systems illustrate another problem with the equivalent porous media approach. Capillarity effects amplify the effect of any heterogeneity in the subsurface. In the context of subsurface contamination by non-aqueous phase liquids, the flow of different phases may be dominantly contained within only the fractures or the matrix blocks. In a near surface contamination scenario, fractures act as preferential pathways for free-phase migration, and in many cases no significant NAPL enters the matrix. In the region of NAPL contamination, water is preferentially excluded from the fractures and groundwater flow will be chiefly through the matrix and areas of minimal fracture aperture. The same behaviour would be observed in the unsaturated zone where water flows preferentially through the matrix and across regions of small fracture aperture (Wang and Narasimhan, 1985). In these cases the flow behaviour, especially of the water phase, is dependent on saturation and/or capillary pressure. Equivalent porous media methods are unable to resolve such behaviour.

2.5.2 Dual Porosity

The dual porosity method conceptualizes the fractured porous media as having two distinct regions and types of porosity within a given representative elementary volume (Kazemi and Gilman, 1993). The REV contains regions that dominate the total pore volume but contribute negligibly to the flow capacity, the matrix, and regions which contribute negligibly to the total pore volume but dominate the flow capacity, the fractures (Warren and Root, 1963). Early work by Barenblatt et al. (1960) on dual porosity formulations dealt with single phase flow. The dual porosity method is the most common approach to simulation of naturally fractured reservoirs (Rossen and Shen, 1989) as evidenced by work by Peng (1990), Fung (1991) and others.

In the dual porosity approach the two separate regions, fracture and matrix, are treated as being distinct, but are allowed to interact with each other. The interaction between the regions is usually treated in one of two ways: either the matrix acts simply as a source / sink for the fractures or the system is treated as two overlapping continuum with flow

from matrix to fracture, fracture to fracture, or matrix to matrix (Bear, 1993). The fluid transfer between regions is proportional to a shape factor related to permeability and the surface area of the matrix-fracture interface. The dual porosity method treats the fractured porous media as a series of blocks of uniform size, although fracture spacing, length, and orientation all vary spatially. Generally, the fracture network is conceptualized as either a series of horizontal fractures, vertical fractures or a combination of both (Kazemi and Gilman, 1993). Dual porosity methods typically ignore transport within the matrix (Sudicky and McLaren, 1992).

Traditional dual porosity methods are implemented numerically with grid blocks larger than the individual matrix blocks. Therefore within each grid block, multiple fractures and matrix blocks are contained (Rossen and Shen, 1989). Typically these methods do not address fluid movement through matrix blocks across the model grid blocks (Rossen and Shen, 1989; Peng et al., 1990).

2.5.3 Discrete Fracture Models

Discrete fracture models explicitly represent each fracture within the area of interest. This method is most often used for near field or very near field studies (Bear, 1993), where a small number of well-defined fractures exist. Time scales of interest are typically shorter than those used in the equivalent porous media approach. Anderson and Woessner (1992) state that discrete fracture models are applied with the assumption of flow only through the fracture; however, the term discrete fracture model has come to mean models where the fracture planes are explicitly represented (Therrien and Sudicky, 1996; Slough et al., 1999), removing the constraint of flow solely within the fractures planes. Many areas of current research in fractured rock are concerned with flow and transport within the matrix adjacent to fractures (Wang and Narasimhan, 1985, Sudicky and McLaren, 1992; Parker et al., 1994, Tidwell and Glass, 1995; Heise, 1999). Discrete fracture models are much more computationally expensive than other methods for representing fractures (Anderson and Woessner, 1992).

For flow in a fracture Darct's Law, Equation 2.2, is used, with the permeability for the fracture, k, as a function of the fracture aperture (Pruess and Tsang, 1990), b:

$$k = \frac{b^2}{12} \tag{2.28}$$

It has been shown that the above equation is locally valid for small fracture lengths (Witherspoon et al., 1980; Brown, 1987; Ge, 1997). This implies that aperture variations in natural fractures can be represented numerically as a series of small, parallel plates, with varying aperture. The variable aperture is usually assumed to be correlated, with a log normal distribution. This aperture field is analogous to the pore size distribution in porous media.

Pruess and Tsang (1990) proposed that each individual fracture contained in the domain of interest can be treated as a heterogeneous porous medium. In this scenario, the fracture planes are represented as either two-dimensional heterogeneous porous medium, contained within a three-dimensional matrix, or a one-dimensional heterogeneous porous medium contained within a two-dimensional matrix. The method allows the use of multiphase porous media models, rather than more complex and less readily available fracture specific models. The constitutive relationships developed for porous media, primarily the capillary pressure-saturation-relative permeability relationships discussed previously, can then be manipulated and applied to two-dimensional fracture planes. This is the most desirable and representative method of treating multiphase flow in fractured porous or non-porous media.

Laboratory experiments of two-phase flow in a rough walled nature fracture by Persoff and Pruess (1995) were consistent with the treatment of fractures as two-dimensional heterogeneous porous media. Their work showed that significant phase interference occurred within the fracture plane, indicating that the relative permeability term, k_{ar}, is important in quantifying multiphase flow in fractures.

2.6 Numerical Model Specifics

Given the complexity of the problems to be addressed, the choice for a numerical model is limited. There are a very limited number of publicly available three-phase flow codes; even fewer accommodate any hysteresis. Fully hysteretic numerical codes are very rare, as the bookkeeping required is numerically intensive. NAPL Simulator (Guarnaccia et al., 1997) is a fully hysteretic code and was selected for this reason. MOFAT (Katyal et al., 1991) is a partially hysteretic code.

2.6.1 NAPL Simulator

One of the numerical models used in this study is NAPL Simulator (Guarnaccia et al., 1997), which is specifically designed to simulate the migration and fate of a single component non-aqueous phase liquid in the subsurface. It is a three-dimensional, three-phase numerical model based on the Hermite-collocation finite-element method, with rectangular elements and properties assigned at nodal points. It accounts for free-phase migration, dissolved-phase transport, and vapour-phase transport. Partitioning of NAPL between phases is addressed by a rate-limited interphase mass transfer model where NAPL phase dissolution, NAPL phase vapourization, dissolved NAPL phase vapourization are treated as first order reactions. Adsorption of dissolved phase NAPL onto soil particles is treated as a linear equilibrium partitioning process. The solution algorithm uses a successive substitution iteration scheme by the total velocity formulation. In the present study, only the multiphase flow portion of the model was used.

The constitutive relationships governing multiphase flow utilized in the simulator are based on the three-phase capillary pressure-saturation-relative permeability model presented in Section 2.4. The numerical model employs a modified version of the van Genuchten (1980) capillary pressure-saturation model and a modified version of Mualem (1975) relative permeability model. Trapping of all phases, water, gas, and LNAPL, is treated using the approach in Section 2.4.3, where the trapped phase saturation is a function of the maximum residual saturation, the maximum phase saturation achieved,

and the current phase saturation. The a fitting parameter term in the van Genuchten (1980) model is scaled between a_D and a_I, along the length of the scanning curves.

2.6.2 MOFAT

MOFAT is a finite element numerical model that considers two-dimensional planar or radially symmetric vertical sections, with properties assigned as nodal points (Katyal et al., 1991). Multiphase flow for water, NAPL, and gas and multicomponent dissolved-phase transport can be analyzed. The model allows for the gas phase to either be treated explicitly (three phase flow) or set to a constant pressure within the domain, resulting in the problem becoming one of two-phase flow where the gas saturation within the domain is solely a function of the NAPL and water flow solutions.

Three-phase constitutive relations for relative permeability-saturation-capillary pressure are represented by the van Genuchten model, as outlined in Section 2.4. A constant value of residual water saturation, S_{Wr} must be specified, and the residual gas phase saturation is assumed to be 0. Trapping of the LNAPL phase was originally represented by Equation 2.5. Modifications for the present study are detailed below.

MOFAT Modifications

The model for trapping of intermediate wetting phase fluid, Equation 2.5, initially employed in MOFAT was modified to better represent the trapping of the LNAPL phase as it moves through the unsaturated zone. The equations of Land (1968) and Kaluarchchi and Parker (1992) only result in trapping of the LNAPL phase as a non-wetting phase. As a result, trapping only occurs when the LNAPL first displaces water out of the pores, and then the water imbibes back in to fill the pores vacated by the migrating oil. However, during the process of infiltration from a surface source, LNAPL displaces gas as it migrates through the unsaturated zone, and to a lesser extent water, due the contrast in mobility of water and gas phases. Thus the original MOFAT equation, Equation 2.26, does not accurately quantify trapping of LNAPL.

To overcome this problem, the trapped LNAPL saturation was redefined based on maximum oil saturation obtained at any node and current oil saturation at that node. Equation 2.19 was rewritten in terms of LNAPL saturation as follows:

$$\bar{S}_{Nr}=\left\{\frac{\overline{S_N}^{max}}{1+R_{NW}\overline{S_N}^{max}}\;\frac{\overline{S_N}}{1+R_{NW}\overline{S_N}}\right\}\quad for\ \overline{S_N}<\overline{S_N}^{max} \tag{2.29}$$

$$\text{where:}\quad R_{NW}=\frac{1}{S_{Nr}}-1$$

In a two-phase, water and LNAPL system, the trapping of the LNAPL phase will be identical using Equations 2.26 or 2.29. However, in a three-phase system, significantly more LNAPL will be trapped through Equation 2.29 within the unsaturated zone. This modification represents the trapping in a similar conceptual manner as in the NAPL Simulator, although it was impossible to modify MOFAT to be quantifiably the same, as NAPL Simulator is fully-hysteretic and MOFAT is partially-hysteretic.

Chapter 3

LNAPL Migration in Fractures

This chapter presents the details of the numerical implementation of the conceptual model presented in Chapter 1 for LNAPL migration and trapping in a fracture aquifer using the NAPL Simulator numerical model. The Nordegg Gas Plant site (Hardisty, 1996) is used as the basis for model development. Firstly, the specifics of the Nordegg Gas Plant are discussed, followed by details on numerical implementation. Results from the base case simulation are then presented and numerical issues evolving from these results are discussed.

3.1 Nordegg Gas Plant

The Nordegg River Gas Plant, west central Alberta, is an sour gas processing plant where organic sludges and LNAPL have seeped from unlined excavations into the underlying bedrock aquifer. The bedrock aquifer consists of extensively fractured fine-grained sandstone of the Paskapoo Formation and is bounded laterally in a limb of an anticline by siltstones and shales, which act as aquitards (Hardisty, 1996). Surficial soils range from 2 to 5 m thick and consist of gravels and silty tills of glacial origin. The water table is located approximately 20 m below the ground surface.

The aquifer has three major joint sets, each set approximately perpendicular to the other two: one set parallel to bedding, one subvertical set parallel to strike; and a subvertical set perpendicular to the bed strike (Figure 3.1). The orientation of the fracture

sets results in matrix blocks that are cubic to rectangular in shape. The apparent length of the fracture planes ranges from 3 m to 5 m. The subvertical fracture sets have larger apertures than the subhorizontal bedding plane set. Results from fracture casting indicate an average aperture of 12.8 mm with a standard deviation of 7 mm.

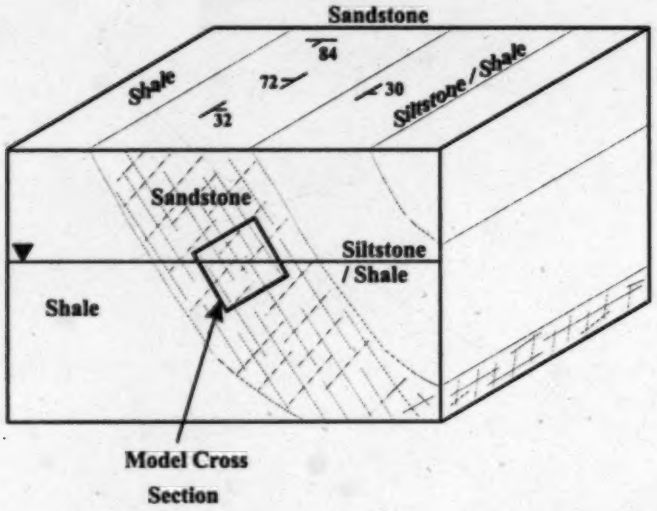

Figure 3.1. Block diagram of aquifer/aquitards at Nordegg Gas Plant, illustrating fractures sets within the aquifer and the cross section used in the numerical model, with strike and dip for the three joints sets and bedding shown.

A plume of free-phase LNAPL is present in the fracture network, constrained within the sandstone unit. Under the prevailing site conditions, LNAPL is not expected to enter the matrix (Hardisty, 1996). The LNAPL has migrated significant distances through the fracture network, with fractures along the Nordegg River discharging free-phase condensate in the past, 700 m down gradient of the spill location. Coring has shown LNAPL at depths of up to 35 m below the ground surface. The LNAPL is also present up to 200 m up gradient of the spill location. The maximum water table fluctuation observed between 1990 and 1996 was 9 m (Hardisty, 1996).

3.2 Numerical Implementation

A two-dimensional numerical model is created with NAPL Simulator to examine the migration of LNAPL within the fracture network at the Nordegg Gas Plant. A 4.8 m by 4.8 m cross-sectional domain is used to provide representative behaviour for the migration of LNAPL within the fractured aquifer (Figure 3.1). The cross-section runs through the sandstone unit, perpendicular to the strike direction.

The conceptual model, discussed in Chapter 1, illustrates how LNAPL migrating through a fractured aquifer is expected to behave. Due to the difficult nature of the problem being addressed, several simplifications of the conceptual model are required for implementation in a numerical model. These simplifications are presented below and include considerations for general numerical implementation and for issues specific to NAPL Simulator.

3.2.1 Dimensionality

A two-dimensional cross section is employed in the numerical simulations. Although the problem of LNAPL migration through a fracture network is inherently three-dimensional, constraining the system to two-dimensions greatly reduces both the implementation and computational time, and makes it possible to actually obtain a solution. A two dimensional model is adequate to qualitatively represent the migration pathways and trapping behaviour.

3.2.2 Fracture Sets

The fracture network beneath the Nordegg Gas Plant contains three fracture sets, as illustrated in Figure 3.1, essentially orthogonal to one another. In the two-dimensional numerical model, two sets of orthogonal fractures are used to represent the network. This simplification was adopted because the NAPL Simulator constrains elements to a rectangular shape. This dictates either orthogonal sets or fractures with steps in them. Hardisty (1996) suggested that incorporating the natural variability of the fracture properties, specifically orientation and length, using statistical distributions and conditioning to known individual fracture planes, may increase the predicted lateral

LNAPL migration distances. The regular nature of the fracture network in this study may therefore reduce that lateral migration observed within the model results.

3.2.3 Fracture Property Representation

Flow within fractures with the actual aperture distribution reported by Hardisty (1996), with a mean aperture of 12.8 mm and standard deviation of 7 mm, cannot be modelled with numerical model, as Darcy's Law, Equation 2.2, would not be valid. Consequently a smaller fracture aperture of 100 μm (0.1 mm) was chosen for the base case simulations. Because the fracture apertures are small compared to the size of the domain to be simulated, the nodal spacing must be significantly larger than actual fracture widths. Properties are assigned at each nodal location and applied over one half the width of each adjacent element. On a network scale, nodal spacing of even the maximum fracture width of 5 mm are unfeasible because representing an area of any significant size would necessitate millions of nodes. For instance, in the 4.8 m by 4.8 m domain used in this study, 5 mm spacing would require 921,600 nodes. The actual discretization used, with spacing of 150 mm, requires 1089 nodes, which results in reasonable simulation times of up to 96 hours.

Permeability and Porosity

Modifications to permeability and porosity terms are necessary because of the differences between the actual and modelled fracture width. These modifications will ensure that the model fractures are still representative of the actual fracture, in terms of fluid volumes and flow rates. Without modification, the model fracture would have a substantially larger pore volume, increasing the storage of fluid within a given element. The fracture width, b, is also a variable in the area term in the flow rate calculation, Equation 2.2, so lack of modifications would result in considerably larger flow rates.

The unmodified permeability, k, is calculated according to the power law (Pruess and Tsang, 1990), based on conceptualized fracture width, b:

$$k = \frac{b^2}{12} \tag{3.1}$$

This permeability term is then modified by the ratio of conceptualized fracture width, b, to actual grid spacing, Δx, to determine modified permeability, k_m, for use in numerical model. This modification also accounts for the area term, A, in Darcy's Law, Equation 2.2.

$$k_m = \frac{b^2}{12} \cdot \frac{b}{\Delta x} \tag{3.2}$$

The porosity term is modified in a similar manner. The actual fracture porosity, ϕ, is modified by the ratio of fracture width to the grid spacing, to determine modified porosity, ϕ_m, for use in numerical model.

$$\phi_m = \phi \cdot \frac{b}{\Delta x} \tag{3.3}$$

Capillary Pressure Curve

Typical fracture capillary pressure curves are substantially steeper, with a more dramatic change in saturation for a given capillary pressure change, than typical porous media curves. However, abrupt capillary pressure-saturation curves necessitate the use of fine discretization for accurate resolution of the fluid saturation distribution and changes in saturation. Less abrupt curves, at LNAPL saturations between 0.0 and residual water saturation, result in lower LNAPL saturations within a given pore volume and consequently lower trapped saturations. The LNAPL flow rates are also reduced due to the lower relative permeability. Thus, a balance is required to match a somewhat representative capillary pressure curve with a grid discretization coarse enough to allow for reasonable numerical solution times. Table 3.1 lists the van Genuchten parameters determined by Reistma and Kueper (1994) on an intact fracture, and the parameters used in this numerical study for the fractures and the matrix. Figure 3.2 shows Reistma and Kueper's (1994) capillary pressure-saturation curve. It is significantly steeper than the curve used to represent the fracture in the numerical model. The curve used for the matrix blocks is also displayed.

Table 3.1. van Genucthen parameters for water-gas capillary pressure-saturations curves in Figure 3.2

	a (m)	n	S_{wr}
Reistma and Kueper (1994)	25	5.4	0.04
Model Fracture	3.0	1.8	0.1
Model Matrix	0.09	1.6	0.1

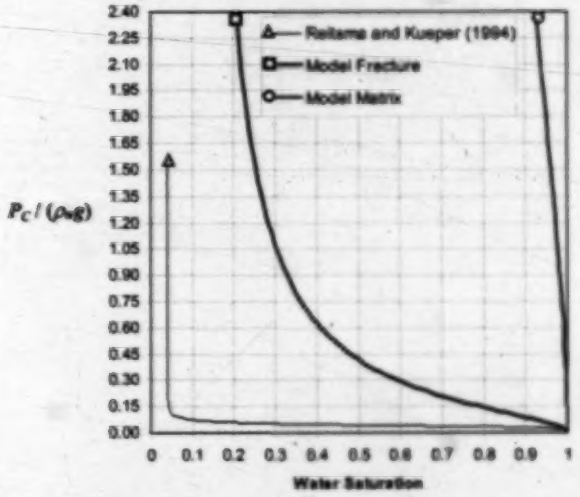

Figure 3.2. Measured fracture LNAPL-water capillary pressure-saturation curve, fracture and matrix LNAPL-water capillary pressure-saturation curves used in model.

3.2.4 Matrix Properties

The same porosity and permeability values are used for the matrix and fractures within this model, while different capillary pressure-saturation curves are used to keep LNAPL within the fractures. This simplification is employed for several reasons. Numerically, this simplifies the problem substantially, as it reduces the heterogeneity. With large matrix porosities, oscillations in the matrix water saturations are observed as water drainage fronts approached the top of matrix blocks. Representative values for the matrix porosity should be orders of magnitude greater than the modified porosity values for a

fracture; however the fractures are the crucial flow regions for LNAPL migration. In addition, for the problems considered, the matrix remains predominantly water saturated due to the capillary effects holding water in the pores above the high above water table. Therefore, little or no water is released into fractures or taken up by the matrix as the water table fluctuates. Water moving due to LNAPL migration in a fracture will be constrained primarily to the fractures. Thus, use of a uniform porosity has little impact on the results, but yields a smooth solution.

A uniform permeability is employed due to a problem with combination of permeability variation over fracture plane and direction of nodal numbering with respect to the fracture plane orientation, discussed with reference to the nodal spacing in the following section.

3.2.5 Aspect Ratio

The grid is required to have equal grid spacing because of the interaction between the fracture plane orientation and the node and collocation point numbering scheme. This constraint is necessary because extensive numerical experimentation showed that the numerical model does not converge when a fracture plane, with a different permeability, porosity, and capillary pressure-saturation-relative permeability curve from the matrix, is aligned with the direction of node numbering and the aspect ratio is not equal to 1.

To illustrate this effect, a simple numerical model is constructed to model a two-phase situation, water and gas, of the draining of an initially water saturated domain. The grid, Figure 3.3a, consists of a 0.20 m tall by 1.0 m wide domain. In this case, termed the Non-rotated Case, the nodal numbering is parallel to the fracture plane, and the maximum difference between node numbers occurs between adjacent fracture and matrix nodes. An aspect ratio of 5 is employed with 100 elements, or 121 nodes. A single, horizontal fracture is located through the domain, illustrated as the thick patterned line through nodes 56 to 66. To simulate the draining of the section, a fixed head boundary for the water phase is specified as the basal boundary, and a fixed gas head of 0.0 is specified from the top boundary. Both lateral boundaries are no-flow boundaries for the water and gas phases. The initial conditions are water saturation of 1.0 everywhere.

that the node numbering can be aligned perpendicular to the fracture plane, in which case convergence occurs.

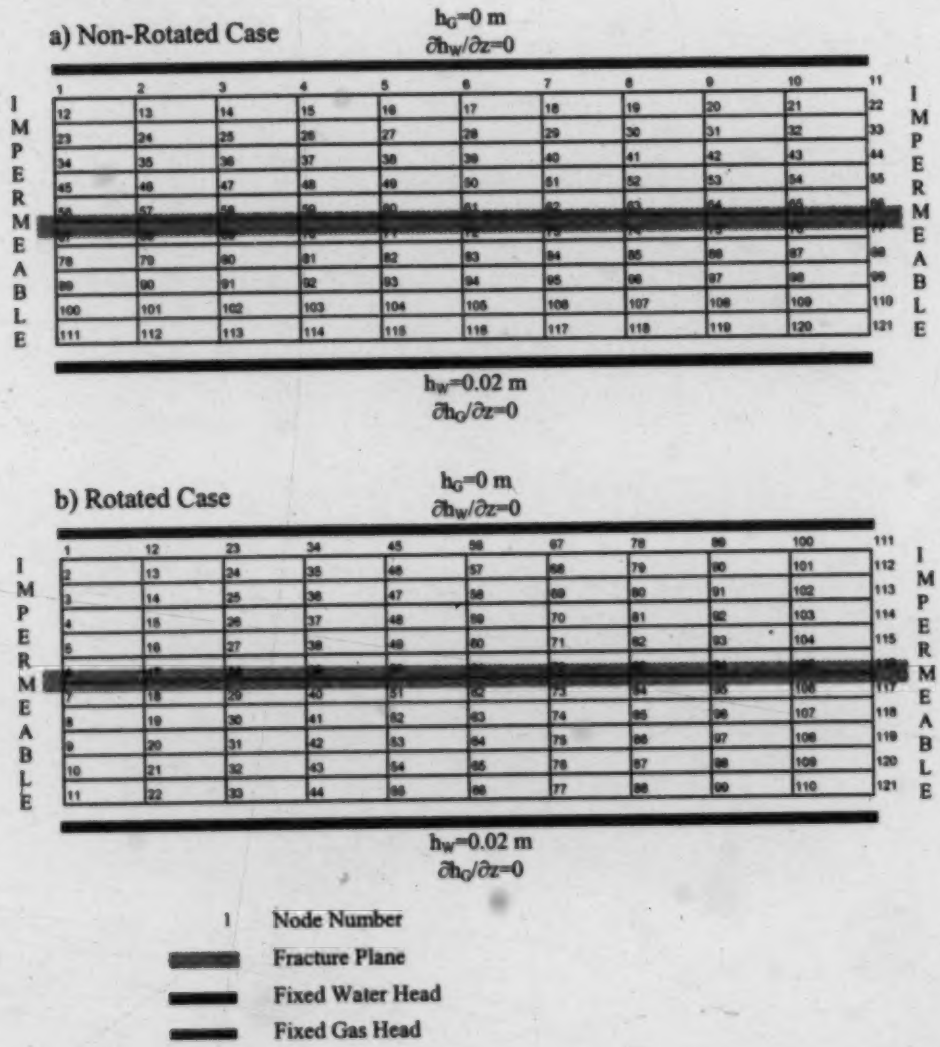

Figure 3.3. Node numbering and fracture orientation: a) non-rotated case, numbering parallel to fracture plane; b) rotated case, numbering perpendicular to fracture plane.(not to scale)

A similar model is constructed with the same physical configuration and the grid rotated by 90°, Figure 3.3b. In this case, termed the Rotated Case, the nodal numbering is perpendicular to the fracture plane, and the maximum difference between node numbers occurs between adjacent fracture nodes.

Figure 3.4 shows a comparison between convergence behaviour of the two cases on the first time step. In the Non-Rotated Case the percentage error in the pressure solution, plotted on the y-axis flattens off at 4.35×10^{-5} and does not converge in 300 iterations. The Rotated Case converges after 18 iterations. An additional, slightly modified version of the NAPL Simulator, Version 2, using a bi-Conjugate gradient solver, shows a similar variation between the solution behaviour, although the Non-rotated Case does eventually converge after 266 iterations. The Rotated Case converges in 10 iterations with Version 2.

Using an aspect ratio of 1 produces a convergent solution for a non-rotated grid in 113 iterations. Figure 3.5 shows the comparison between iteration behaviour in this case, the original Non-Rotated Case, and the original Rotated Case.

Due to the orientation of the two fracture sets within an orthogonal network, it is impossible for fracture planes to be specified that do not align with the node numbering. Using a uniform aspect ratio of 1 produces a convergent solution. Thus, a uniform permeability, k, and constant grid spacing is employed.

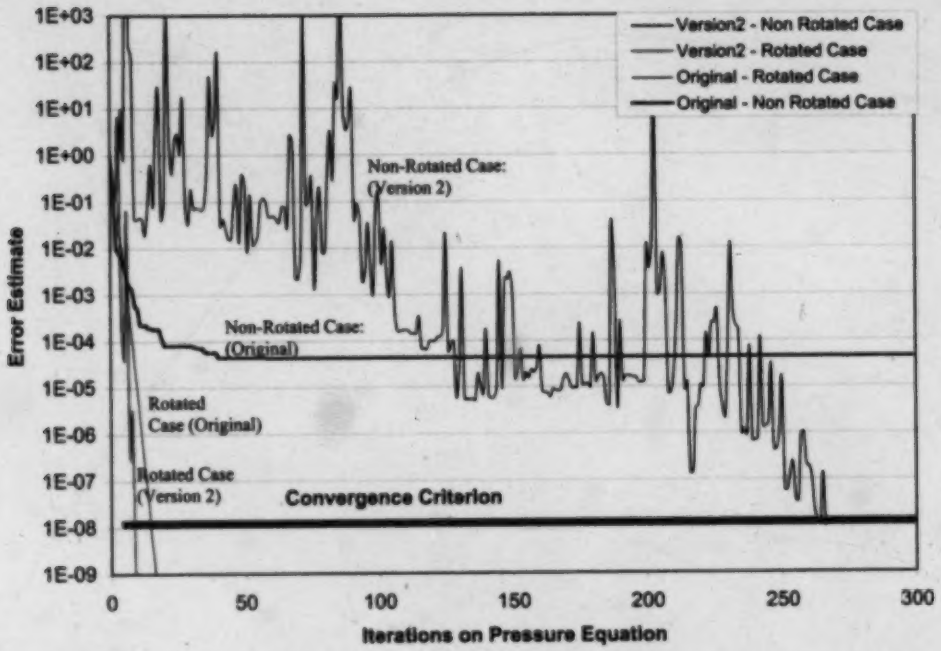

Figure 3.4 Convergence behaviour for Non-Rotated and Rotated Case simulations.

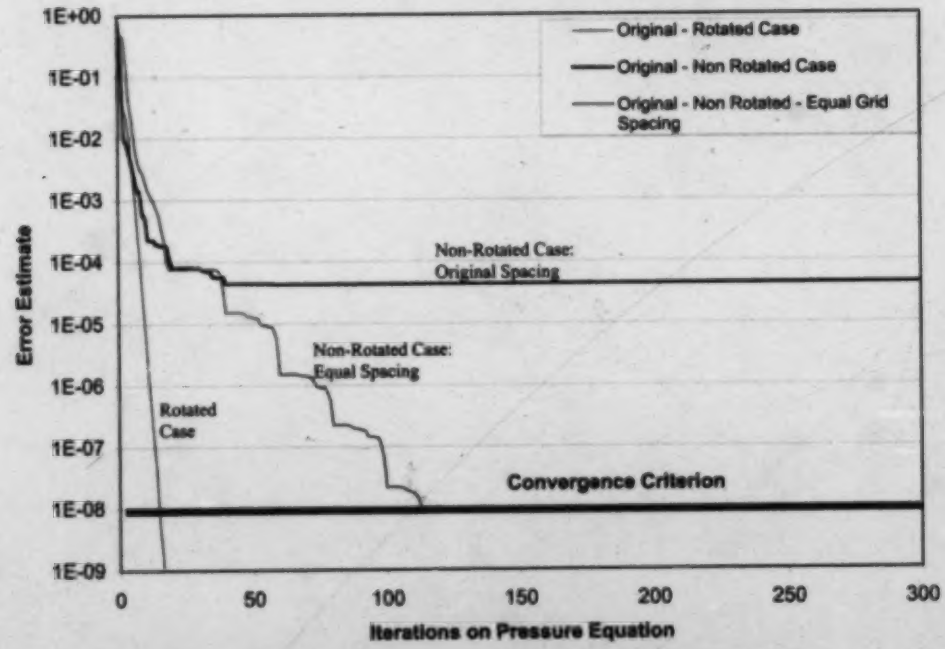

Figure 3.5 Convergence behaviour comparing, Non-Rotated, Rotated and Equal Grid Spacing simulations for original NAPL Simulator code.

3.3 Base Case Simulations

A base case simulation is developed to study the migration of a slug of LNAPL within a fracture network, based on a small cross-section of the Nordegg Gas Plant. The simulation strategy is to start with an initially water saturated domain, and apply boundary conditions such that the system partially drains and a water table develops through the middle of the domain. Once the water distribution reaches equilibrium, a slug of LNAPL is injected in to a fracture directly above the water table, and allowed to redistribute through the domain.

3.3.1 Grid Discretization

The domain, 4.8 m tall by 4.8 m wide, is discretized into 32 elements on each side, corresponding to 1089 nodal points. The grid employs a uniform element spacing of 0.15 m by 0.15 m.

3.3.2 Boundary Value Problem

The boundary value problem for this simulation is shown in Figure 3.6. The domain is 4.8 m by 4.8 m, rotated by 30° from horizontal. The matrix blocks are denoted by the grey blocks, with intervening fracture planes. The boundary conditions are displayed along the sides of the domain. The top boundary and portions of each side boundary are specified gas head pressure boundaries, with values assigned to create a gas head of 0.0 along the entire boundary and no-flow boundaries for the water and LNAPL phases. The bottom boundary is a specified water pressure head boundary, with values assigned to create a water head of 3.0 m along all three segments, and no flow boundaries for the LNAPL and gas phases. The water table location that develops from these boundary conditions is noted on Figure 3.6. The LNAPL is injected as a fixed rate source of 4.0×10^{-6} m^3/s, at the location noted with a dot, in a fracture segment directly above the water table

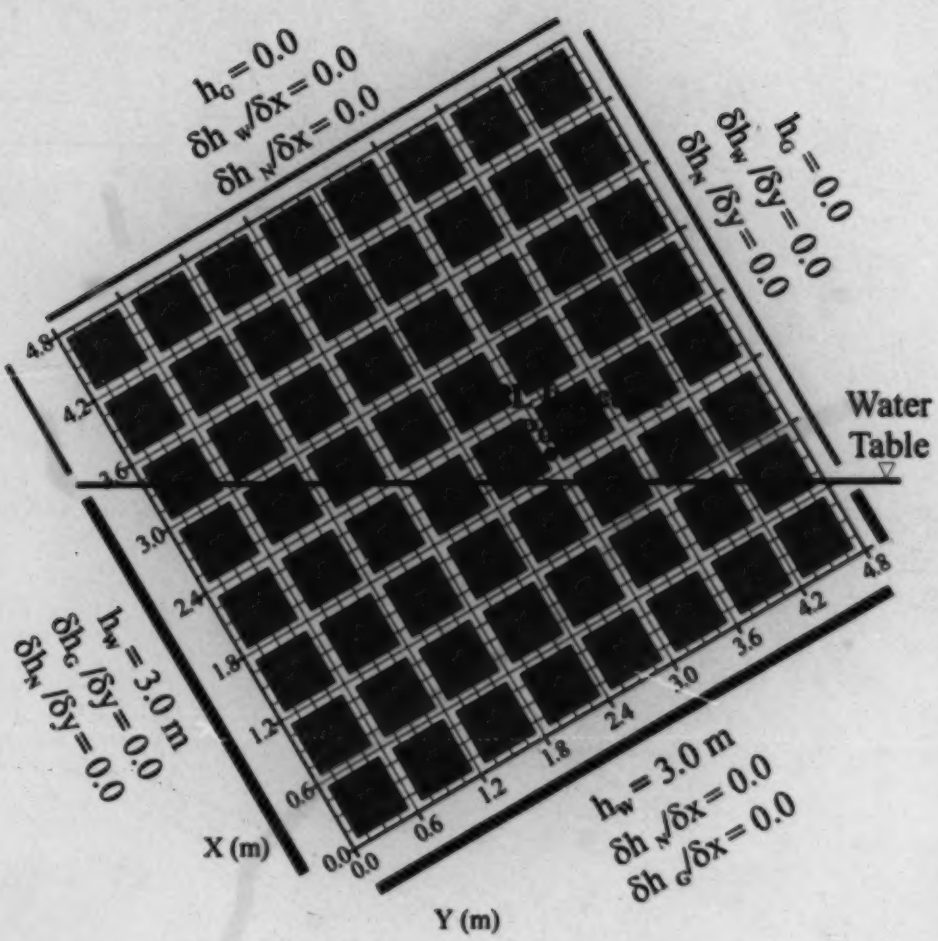

Figure 3.6. Boundary value problem for NAPL Simulator model of LNAPL migration in fractured aquifer. Grey squares represent matrix blocks.

3.3.3 Base Case Properties

The fluid, porous media, and fracture properties used in the base case simulation are shown in Table 3.1. The fracture aperture chosen as $1x10^{-4}$ m, or 100 μm, resulting in a fracture permeability, k, of $8.3x10^{-10}$ m^2, as per Equation 3.1, and a modified fracture permeability, k_m, of $5.5x10^{-13}$ m^2, as per Equation 3.2. A porosity of 0.33 was chosen for both the matrix and the fracture.

Van Genuchten parameters for the matrix were chosen so only minor amounts of LNAPL enter matrix. For the fracture, values were chosen that allowed significant volume of LNAPL to accumulate with relatively low capillary pressures, but also allowed for a relatively coarse discretization. The fracture and matrix primary drainage and main imbibition capillary pressure-saturation curves are shown in Figure 3.7 for both the gas-water, gas-LNAPL, and LNAPL-water phase combinations. The relative permeability curves for the water and gas phases are shown in Figure 3.8 for primary drainage.

Residual saturation for the water phase was chosen as a low value from the range given by Mercer and Cohen (1990). The residual saturation for the gas phase was set to 0.0, because gas is usually trapped in low quantities, and often, over time, reduces to zero due to dissolution into the aqueous phase. LNAPL residual saturations, as a non-wetting phase and as a wetting phase, were chosen so that the sum would fall within the middle of the range given by Mercer and Cohen (1990) for LNAPL in the near surface. Fluid densities, viscosities, and interfacial tensions were chosen as representative values for each phase.

Table 3.1. Base Case Properties, LNAPL migration in fractured aquifer.

Nodal Spacing - Δx and Δy		0.15 m
Grid Rotation		30°
Fracture aperture,	b	1.0×10^{-4} m
Fracture Permeability	k_m	5.5×10^{-13} m^2
Matrix Permeability	k	5.5×10^{-13} m^2
Fracture Porosity	ϕ	0.33
Matrix Porosity	ϕ	0.33
van Genuchten parameters - Fracture		
	a_I	3.0 m
	a_D	4.0 m
	n	1.8
van Genuchten parameters - Matrix		
	a_I	0.09 m
	a_D	0.09 m
	n	1.6
Residual Saturation		
Water	S_{Wr}	0.10
LNAPL (wet.)	S_{Nwr}	0.10
LNAPL (non-wet.)	S_{Nnr}	0.15
Gas	S_{Gr}	0.00
Fluid density		
Water	ρ_W	1000 kg/m^3
LNAPL	ρ_N	800 kg/m^3
Gas	ρ_G	1.22 kg/m^3
Fluid viscosity		
Water	μ_w	1.0×10^{-3} N·s/m^2
LNAPL	μ_o	8.0×10^{-4} N·s/m^2
Gas	μ_G	1.2×10^{-5} N·s/m^2
Interfacial Tension		
Gas-Water	σ_{GW}	7.2×10^{-2} N/m
Gas-LNAPL	σ_{GN}	3.6×10^{-2} N/m
LNAPL-Water	σ_{NW}	3.6×10^{-2} N/m

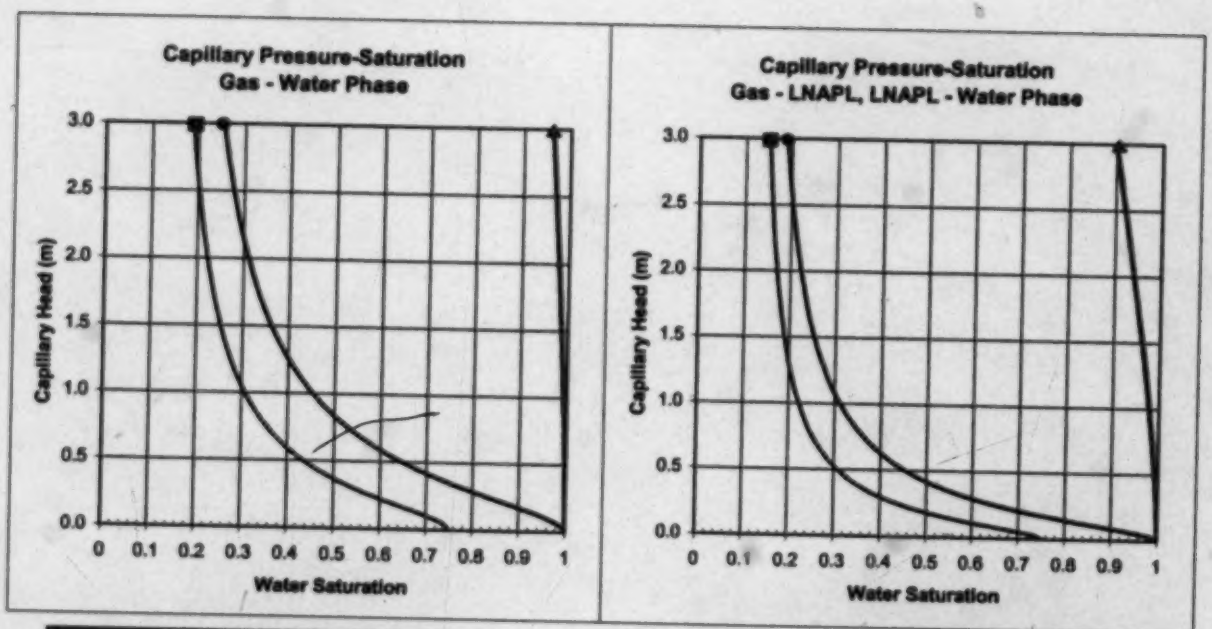

Legend
Fracture - Primary Drainage (PDC)
Fracture - Main Imbibition (MIC)
Matrix - Primary Drainage (PDC)

van Genuchten Parameters		
	Fracture	Matrix
a_d	3.0	0.09
a_i	4.0	0.09
n	1.8	1.6
S_{wr}	0.1	0.1
S_{lr}	0.25	0.25

Figure 3.7. Capillary pressure-saturation relationships for: a) gas-water phase; and b) gas-LNAPL or LNAPL-water phases, base case model.

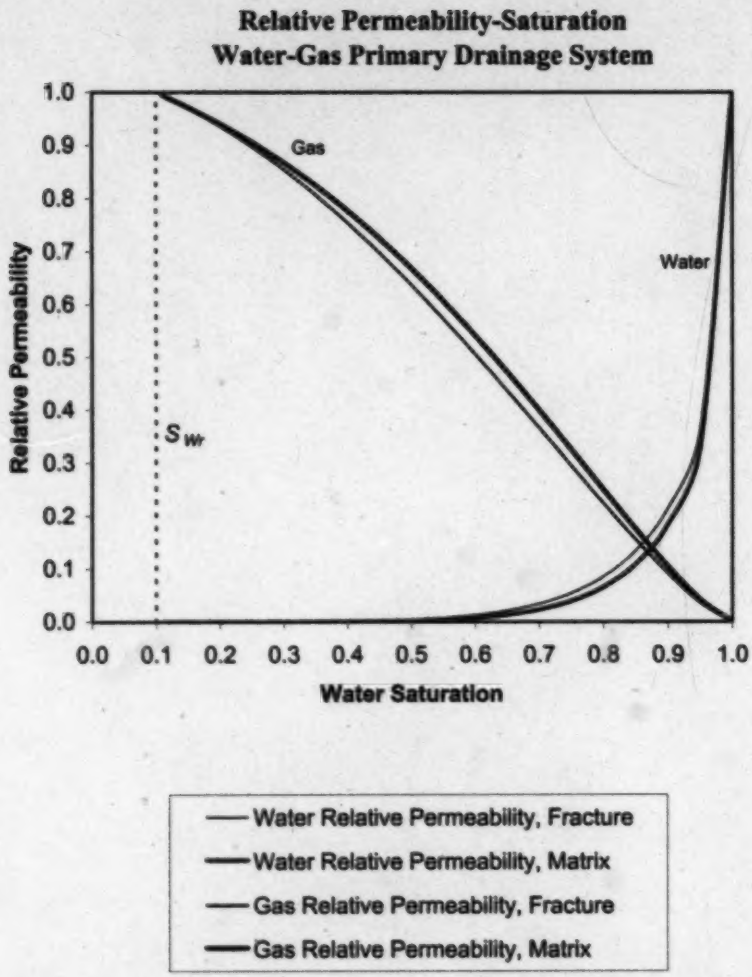

Figure 3.8. Fracture and matrix relative permeability-saturation curves for primary drainage, water and gas.

3.4 Results

3.4.1 Drainage

The domain is initially saturated with water. Fixed pressure head boundary conditions are prescribed for the water phase along the two lower sides of the grid and for the gas phase along portions of the upper two boundaries, as illustrated in Figure 3.6. The water table is allowed to drop through the domain and come to rest at 3.0 m above the bottom corner. Figure 3.9 illustrates the distribution of water in the system when drainage is complete. The matrix blocks are evidenced by the square regions of higher water saturation surrounded by the planar fractures. The water saturation in the matrix ranges from 0.95 in the upper corner to 1.0 at the water table. In the fractures, the water saturation ranges from 0.21 in the upper corner to 1.0 at the water table.

3.4.2 Injection

An injection well is used to place a slug of LNAPL in the fracture network, just above the water table. The point of injection is located at a fracture node where the initial water saturation is 0.89 and is noted with a circle on Figure 3.6 and 3.9. During this process, 0.0786 m^3 (78.6 L) of LNAPL are injected in 20,000 seconds, a somewhat arbitrary rate. The evolution of the LNAPL plume in the fracture network during injection is displayed in Figures 3.10, 3.11, and 3.12. For display purposes, only LNAPL in the fracture nodes is presented. Small volumes of LNAPL are present the adjacent matrix nodes, both due to the pressure build-up around the injection point and the use of the van Genuchten formulation for the capillary pressure-saturation relationship in the NAPL Simulator.

Figure 3.10 shows the LNAPL distribution after 5000 seconds of injection. The injection point has reached a LNAPL saturation of 0.71. The node immediately above also has a saturation of 0.71. Above this point the saturation drops to 0.11. The node immediately below the injection point, at intersection A on Figure 3.10, has a saturation of 0.46. In the near horizontal fracture, inclined 30° from horizontal, the LNAPL is migrating

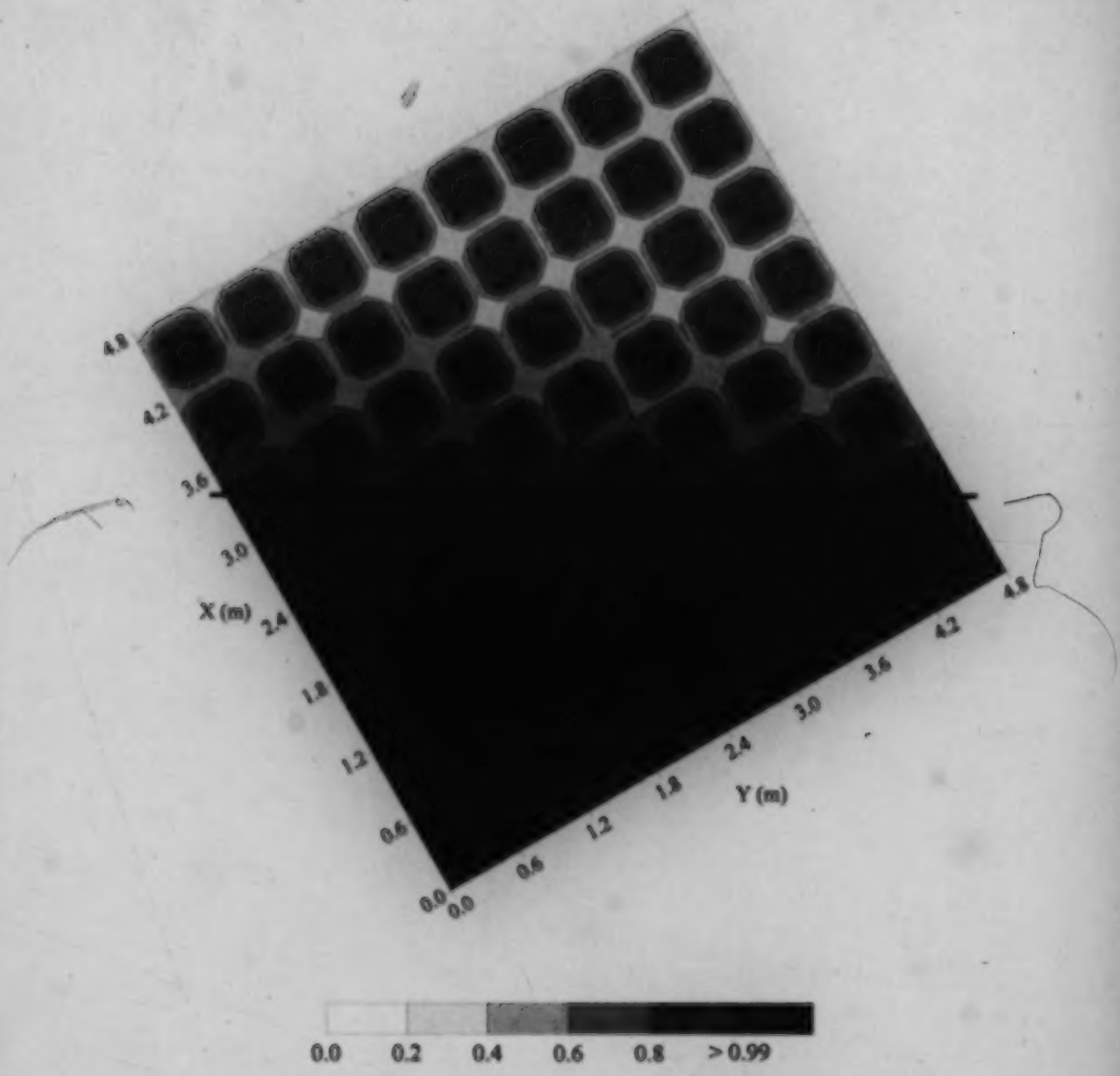

Figure 3.9. Water saturations prior to LNAPL injection. The node for LNAPL injection is marked with a circle.

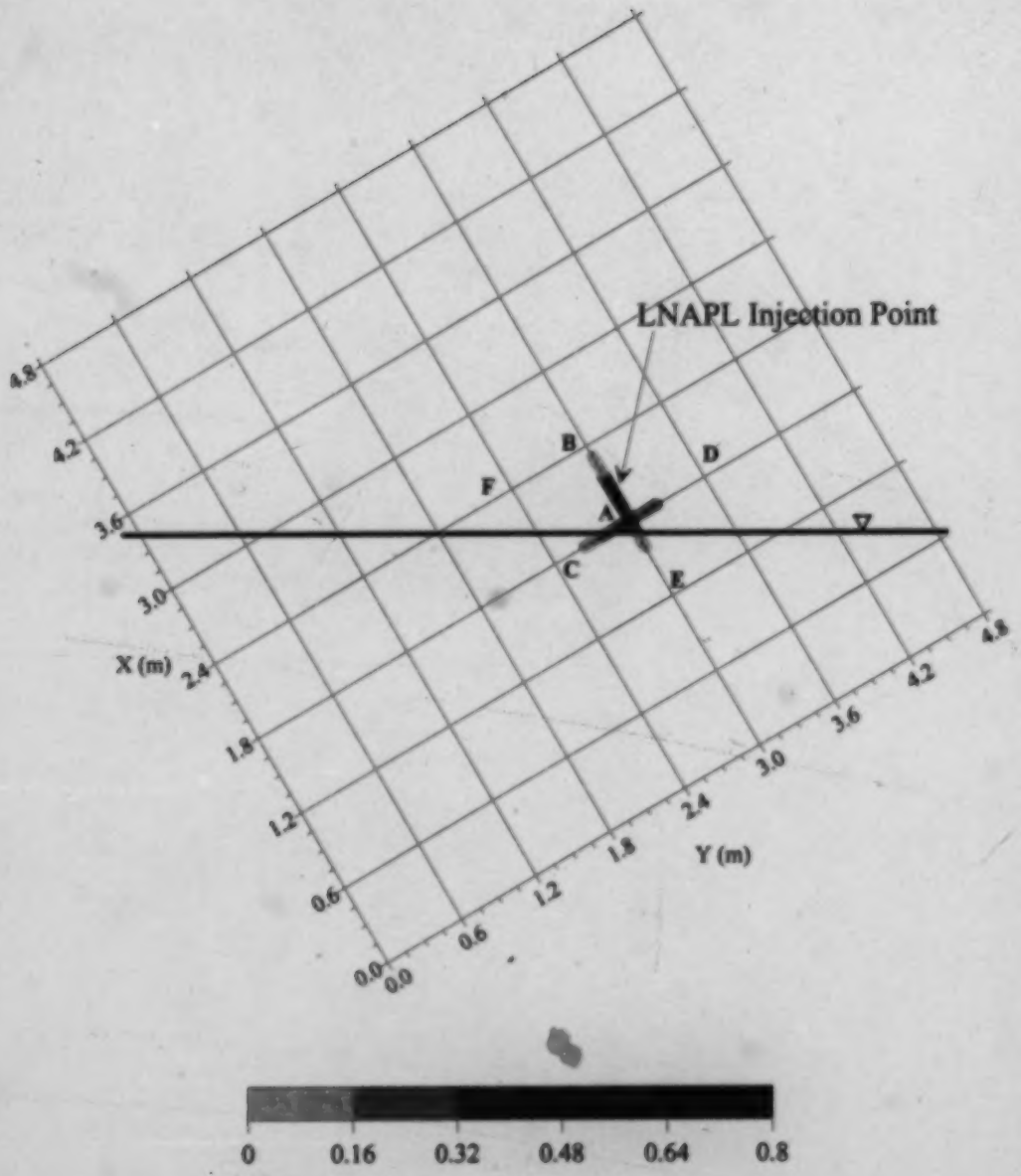

Figure 3.10. LNAPL distribution in fracture network during injection, 5,000 seconds. Letters A-F correspond to fracture intersection locations, discussed in the text.

down-dip under gravity effects to the adjacent node at a saturation of 0.28; however, the influence of the gravity force is reduced because the force vectors are rotated 60° from vertical. Up-dip migration is also occurring in this fracture due to capillary effects and pressure from the injection, as the region is slightly above the water table. The upward node saturation is 0.29. Capillary forces are not influenced by directional so the rotation of the fracture plane does not affect their influence. The up-dip migration is occurring against gravity, but with buoyancy.

The subvertical fracture present at this intersection also allows for down-dip migration away from the intersection. The LNAPL is only just starting to infiltrate into this node, and the saturation is 0.01. This node is just below the water table, so the water saturation prior to injection was 1.0.

At the end of 10,000 seconds of injection LNAPL has continued to migrate away from the injection point (Figure 3.11). The saturation at the injection point is 0.79. Directly above and below, the saturations are 0.79 and 0.72, respectively. The LNAPL has reached the upper intersection point, point B, above the injection point, and is spreading both down-dip and up-dip in the fracture segments. At intersection A, directly beneath the injection point, the LNAPL has fully penetrated the near vertical segment, and further up-dip and down-dip migration are occurring in the new-horizontal fracture segments. Along the near vertical down-dip fracture segment, the LNAPL has just reached the fracture intersection C at this time.

The final LNAPL distribution at the end of the injection period, 20,000 seconds, is shown in Figure 3.12. The saturation at the injection point is 0.81. The LNAPL has reached the fracture intersections C and D and is approaching E, adjacent to the primary intersection A located beneath the injection point. The LNAPL volume in the system is now 0.0786 m^3 (78.6 L).

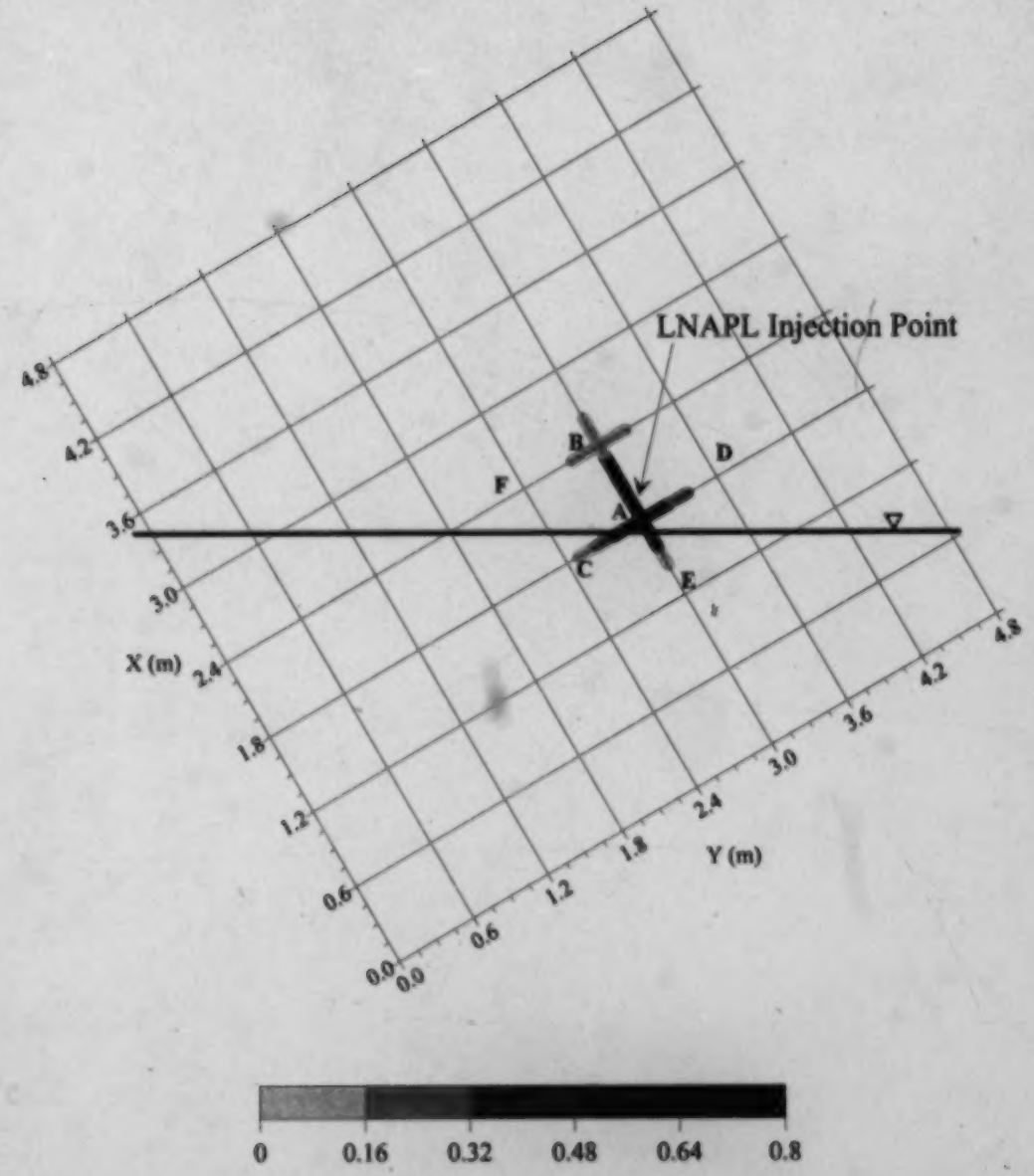

Figure 3.11. LNAPL distribution in fracture network during injection, 10,000 seconds. Letters A-F correspond to fracture intersection locations.

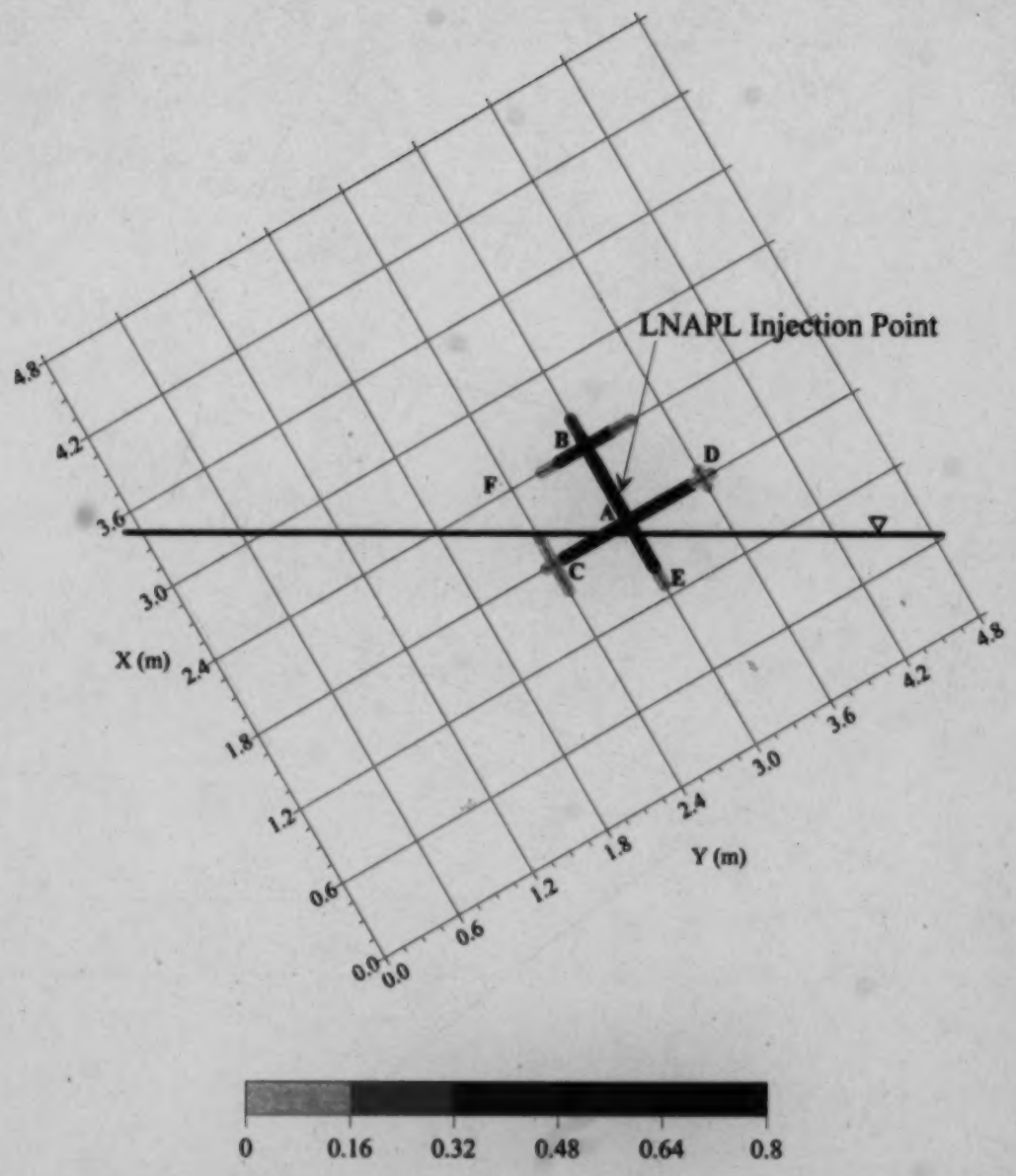

Figure 3.12. LNAPL distribution in fracture network after injection, 20,000 seconds. Letters A-F correspond to fracture intersection locations.

Figure 3.13 shows a comparison between saturations in the fracture and the adjacent matrix blocks around the injection point. LNAPL is present in the fracture at a saturation 0.81. The immediately adjacent matrix nodes have saturations of 0.08 and the next adjacent have saturations of 0.01. In the third matrix node away from the fracture the LNAPL saturation is only 0.003. Such low saturations are inconsequential to the overall solution behaviour.

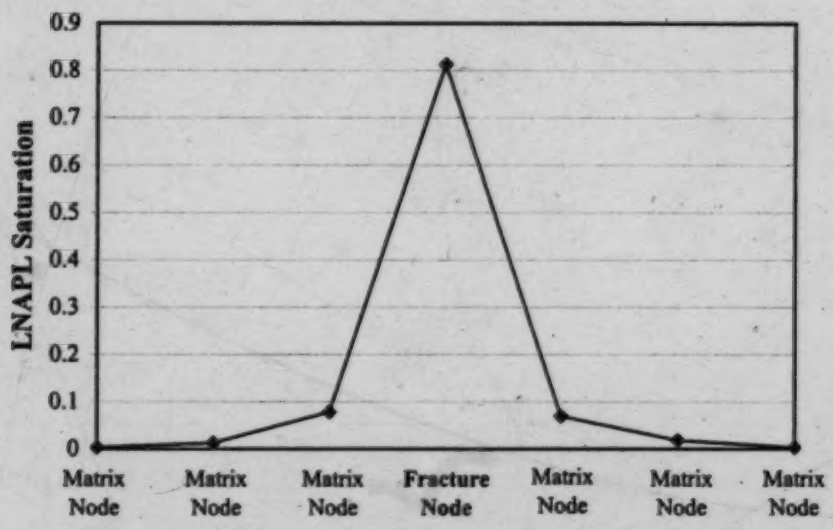

Figure 3.13. LNAPL distribution across a fracture plane at the injection location, 20,000 seconds.

3.4.3 Redistribution

Following the injection phase, the LNAPL is allowed to redistribute within the domain under the current gradients for a further 80,000 seconds. The distribution at the end of this time period is displayed in Figure 3.14. The saturation in the injection region has dropped to 0.61, as LNAPL has migrated through the fracture network.

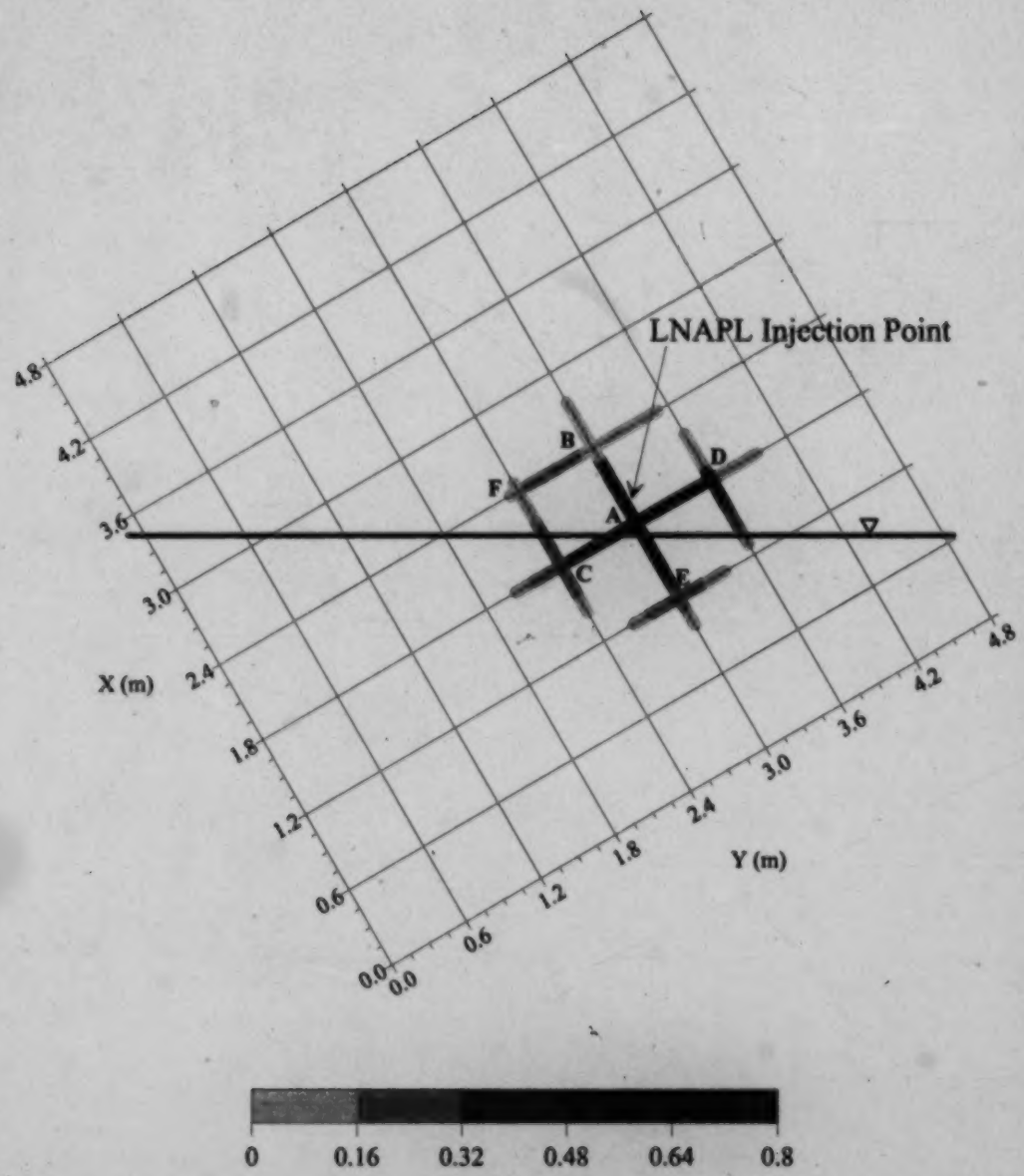

Figure 3.14. LNAPL distribution in fracture network after redistribution, 100,000 second
Letters A-F correspond to fracture intersection locations.

In the fracture containing the injection point, the LNAPL has penetrated 0.65 m beneath the water table, past intersection point E. At intersection E, the LNAPL has migrated into each of the three other fracture segments, moving downwards through the two segments an equal amount, and upwards through the third towards the water table. Additional LNAPL has penetrated beneath the water table through intersection point C, down both fracture segments.

In the unsaturated zone, additional LNAPL has migrated towards and past intersection D. Up-dip migration, due solely to capillary forces, through the two segments is less than the down dip migration away from the source area towards the water table. Similar behaviour is observed at intersection B, where further up dip migration is occurring through the two fracture segments, and down dip migration is occurring towards intersection F.

3.4.4 Mass Balance Issues

The time period simulated above for redistribution of LNAPL in the fractured aquifer is very short compared to simulation time desired to address rises and drops of the water table. It is expected that at least an order of magnitude more time would be required to simulate a single water table rise event. Although the migration results appear reasonable, during the redistribution period, 80,000 seconds of simulation time, a large oil mass balance error of 11.6% was generated, defined as the percentage change in oil mass in the domain between the end of the injection phase, t = 20,000, and the current time, t = 100,000. Figure 3.15 shows the oil mass error at each time step through this simulation period. It is evident that the error is systematic, in that it is of similar magnitude and the same sign through most of the period. It can be concluded that any further simulation time will result in an increased the oil mass error. Gradients expected during forcing water table movement would be much larger than those generated during passive migration, likely resulting in even larger mass errors.

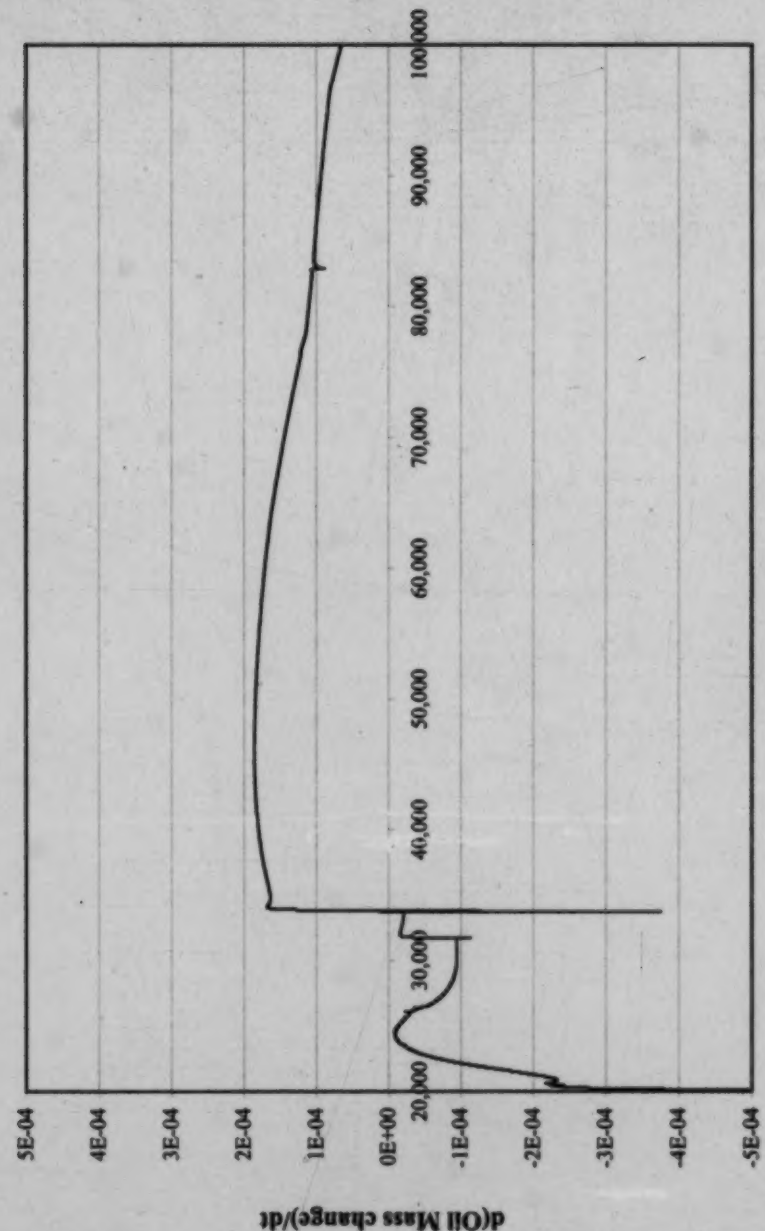

Figure 3.15. LNAPL mass balance error during redistribution period, NAPL Simulator.

3.5 Numerical Model Issues

The mass balance error observed in the base case simulation over the short time period simulated is substantial, and grows steadily. The numerical scheme appears to not be mass conservative in this implementation. Therefore, predictions from this model on migration and trapping of LNAPL in the fracture network subjected water table fluctuations may be misleading.

Extensive testing of the behaviour of the mass balance error was performed. It was observed that the sign as well as the magnitude of the mass balance error changed for slightly different, but not significantly steeper or shallower, capillary pressure-saturation relationships. Simpler conceptual problems, with less heterogeneity, still exhibit this systematic mass balance error, but the magnitude is reduced. Turning off the hysteretic algorithm, using the same drainage capillary pressure-saturation-relative permeability parameters as the base case, resulted in the error switching from persistently positive to persistently negative.

Results for the two versions of the numerical model available, one version employing the generalized minimum residual method (GMRES) and one version employing a bi-Conjugate gradient algorithm with ILU preconditioning, were compared. The results show that the error is slightly different, but to not significantly so, between the versions.

The error is also not associated with a non-converged solution. Tightening the convergence constraints on both the pressure and saturations solutions did not reduce the error. Modifications were made to the code to examine the influence of the value used as a small number cut-off, which altered the mass balance error, but did not substantially enhance or eliminate it.

It is postulated that the cause of this mass balance error is the particular numerical method used by NAPL Simulator. The structure of the system matrix is strongly dependent on the numbering scheme chosen (Guarnaccia *et al.*, 1997). The Hermite

Collocation method is not symmetric, positive definite, or diagonally dominant (Dyksen and Rice, 1986). It enforces continuous gradients in the solution. However, gradient discontinuities in the gradients are present: at interfaces between fluid phases, and at boundaries between matrix blocks and fractures (of which there are many). The Hermite Collocation method appears, under this implementation, to be inadequate for achieving an acceptable solution for the problem of water, LNAPL, and gas migration in a fractured aquifer.

3.6 Summary

A numerical model was developed using NAPL Simulator for the numerically difficult problem of LNAPL migration within a fractured porous media domain. Modifications were necessary to the original conceptual model, both from a numerical implementation perspective and from issues inherent to the NAPL Simulator code. These modifications include using an "easier" capillary pressure-saturation-relative permeability functions for the fractures and constraining the fracture network to orthogonal, infinite fractures.

Modifications made strictly to obtain a solution with NAPL Simulator include equal element spacing, and setting the matrix and fracture porosities and permeabilities the same. The LNAPL behaviour during and following injection was discussed. LNAPL was shown to migrate both up and down dip through the unsaturated fractures. Small amounts of LNAPL migrated into the matrix blocks due to the use of the van Genuchten model for capillary pressure-saturation-relative permeability. Migration into the matrix was particularly strong directly adjacent to the injection point due to the injection pressure.

The LNAPL migration results appear reasonable, but an unacceptably large LNAPL mass balance error was observed in the NAPL Simulator for this particular numerical configuration. During the 80,000 seconds following injection the LNAPL mass increased by 11% within the domain. The rate of artificial mass increase appears relatively uniform. Further simulation time would only increase the overall mass balance error.

The cause of this error was investigated and is determined to be a result of the use of the Hermite Collocation method, which is particularly sensitive to discontinuities in the derivatives. In this study, with three mobile phases and extreme heterogeneity, this sensitivity results in severe LNAPL mass balance errors.

Chapter 4

Heterogeneous Porous Media Simulations

The migration and subsequent trapping of LNAPL in porous media is controlled by multiple factors, a number of which are examined in this Chapter. The conceptual model for LNAPL migration in porous media containing lenses, as discussed in detail in Chapter 1, illustrates how LNAPL infiltrates from a surface spill into the subsurface, migrating down through the unsaturated zone. Lenses should act to either divert or focus the migrating LNAPL. Upon encountering the water table, the LNAPL pools and depresses the water saturation region, continuing down gradient. Water table fluctuations might reinitiate the vertical migration of LNAPL. As the body of free-phase LNAPL contaminant moves, it leaves behind a trail of immobile, trapped LNAPL, which acts as a source of dissolved-phase and vapour-phase contaminant.

In this Chapter, a number of scenarios are developed to examine the migration and trapping of LNAPL within porous media, and to illustrate the importance of water table fluctuations and heterogeneities on LNAPL migration. A homogeneous base case is first presented employing the MOFAT (Katyal et al., 1991) numerical model. This case provides a basis of comparison for various heterogeneous cases and results from the NAPL Simulator. Modifications to the water table location and gradient are investigated.

Subsequently, both coarse-grained and fine-grained lenses are introduced into the domain to illustrate the LNAPL migration behaviour as a of function of the water table location.

4.1 Base Case Simulation

A base case simulation was developed for the initial examination of LNAPL migration and trapping in a silty homogeneous porous media. This section presents the detail of the problem, including grid discretization, boundary value problem definition, porous media and fluid properties, and results of the base case simulation.

4.1.1 Grid Discretization

For the base case simulation, a 20 m wide by 9.5 m tall domain is discretized into a grid 40 elements wide and 19 elements tall, corresponding to 820 nodal points. The grid employs a constant spacing of 0.5 m by 0.5 m. Grid modifications for one series of simulations are introduced later.

4.1.2 Boundary Value Problem

Figure 4.1 shows the schematic diagram of the boundary value problem used in the initial, homogeneous simulations. The top boundary, representing the ground surface, is assigned a gas pressure, P_G, of 0.0, apart from the LNAPL source region. The side boundaries are no flow boundaries, except for the right boundary from immediately beneath the source region to the water table. Along this edge the gas pressure head is set to 0.0, preventing the gas phase from being trapped by the invading LNAPL above the water table along the boundary during the infiltration period and preventing numerical instabilities. The basal boundary is a specified water head boundary that is adjusted, in time and between simulations, to represent various water table locations.

The LNAPL source region consists of two nodes with a LNAPL head, h_N, of 1.1 m applied for the first 2 days of the simulation period, until a LNAPL volume of 0.8 m^3 infiltrates the domain. During the infiltration period, the water table is fixed, sloping linearly from an elevation of 6.6 on the right to 6.5 m on the left, a gradient of 0.005.

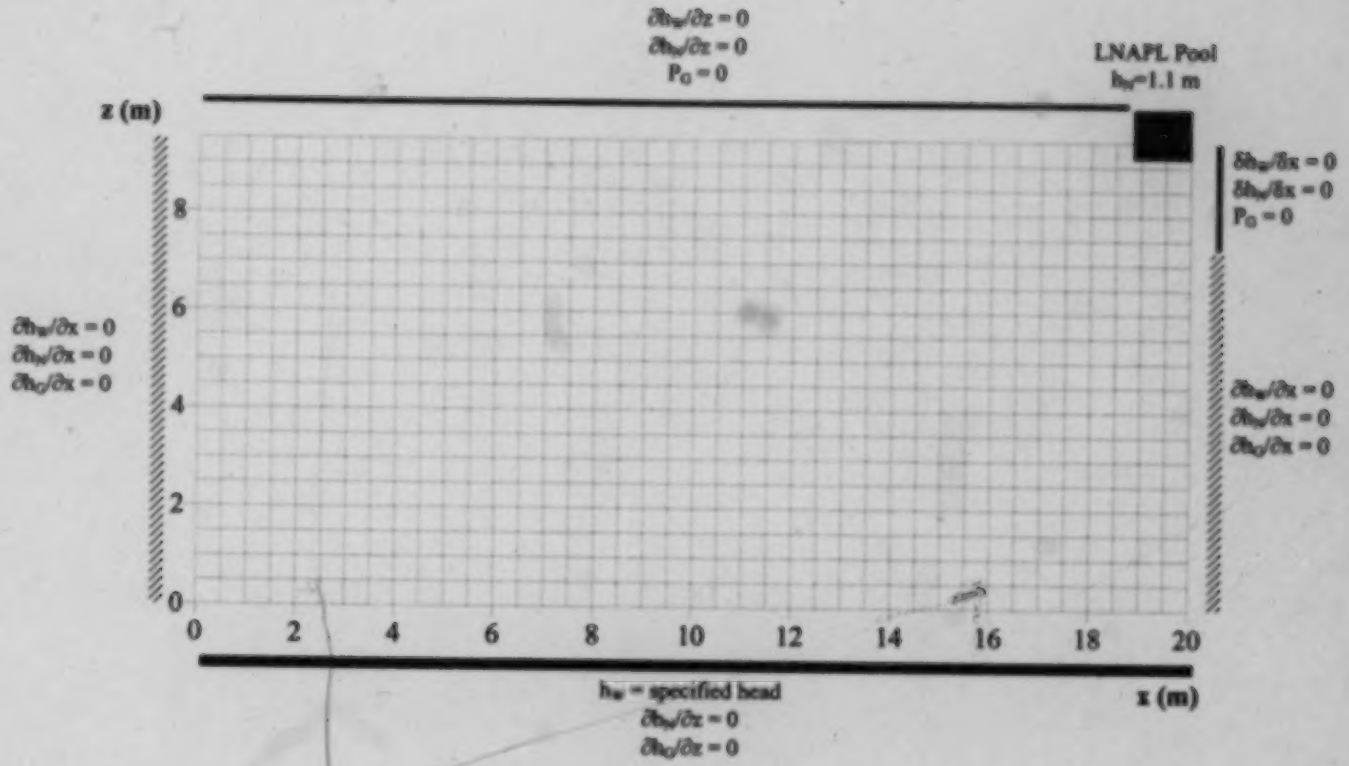

Figure 4.1. Boundary value problem for base case simulation of LNAPL migration and redistribution in homogeneous porous media.

After two days, the LNAPL source is removed and a three-day redistribution period is simulated, with the water table kept constant. Subsequently, the water table elevation was lowered at a rate of 0.05 m/day for 40 days, resulting in a total drop of 2.0 m. This shifting boundary condition was generated using an option in MOFAT for linearly scaling boundary conditions between two end members through time, with the new boundary conditions assigned at the beginning of each time step.

4.1.3 Initial Water Distribution

The initial water saturation distribution for the base case simulation is shown in Figure 4.2, prior to LNAPL infiltration, as a one-dimensional vertical section through the top portion of domain. The water saturation ranges from 0.48 at the top boundary to 1.0 at and below the water table. This distribution corresponds to the water-air capillary pressure-saturation curve for the host medium, shown in Figure 4.3 a.

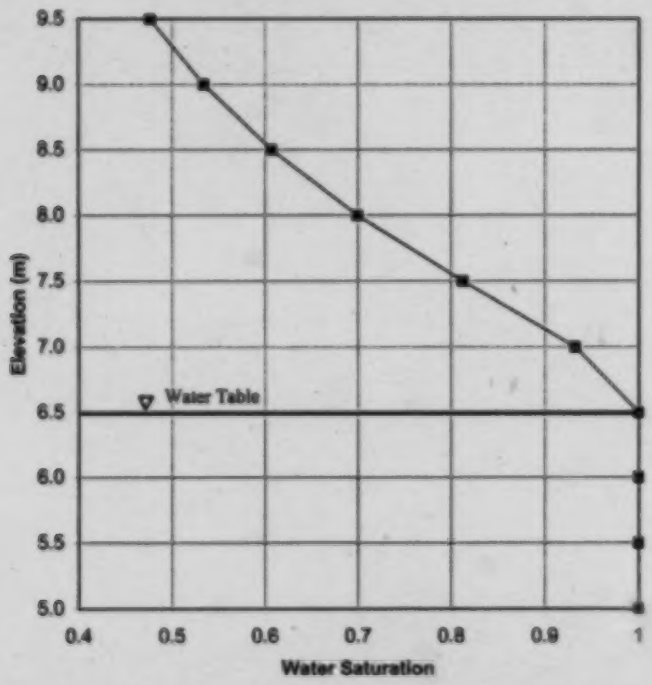

Figure 4.2. Initial water distribution for base case simulation, x = 20 m.

4.1.4 Porous Media Properties

Porous media and fluid properties for the base case simulation are presented in Table 4.1. For all subsequent simulations fluid properties and porosity remain constant. Modifications to other porous media properties are documented as necessary.

The van Genuchten model (1980) is used to represent the capillary pressure-saturation-relative permeability relationship. The scaling parameters and the permeability are representative of a silty soil (Freeze and Cheery, 1979). This soil choice, and subsequently the α and n parameters, results from the desire to have a relatively coarse discretization with an accurate definition of the capillary pressure-saturation curve. The capillary pressure-saturation curves for the water-gas system and the gas-LNAPL or LNAPL-water systems are shown in Figure 4.3. Both the primary drainage curve (PDC) and the main imbibition curve (MIC) are plotted; they represent the upper and lower bounding curves for problem addressed. The primary drainage curves for the relative permeability-saturation curves for the water and gas phases are plotted in Figure 4.4. The LNAPL curve is not shown, as it is a ternary diagram.

The water phase residual saturation is set to 0.0 in this base case simulation to allow for comparisons with NAPL Simulator results in the sensitivity analysis. The residual saturation for the gas phase is also set to 0.0, as gas is usually trapped in low quantities (Mercer and Cohen, 1990). The LNAPL residual saturation is chosen from the middle of the range given by Mercer and Cohen (1990) for LNAPL in the near-surface settings. The fluid densities, viscosities, and interfacial tensions are chosen as representative values for each phase (Mercer and Cohen, 1990).

Table 4.1. Base Case Properties, LNAPL migration in porous media.

Nodal Spacing - Δx, Δy	0.5 m
Permeability k	3.54×10^{-12} m^2
Porosity ϕ	0.2
van Genuchten parameters	
a	0.75 m
n	1.8
Residual Saturation	
Water S_{Wr}	0.0
NAPL S_{Nr}	0.2
Gas S_{Gr}	0.0
Fluid density	
Water ρ_W	1000 kg/m^3
NAPL ρ_N	800 kg/m^3
Gas ρ_G	1.22 kg/m^3
Fluid viscosity	
Water μ_W	1.0×10^{-3} N·s/m^2
NAPL μ_N	8.0×10^{-4} N·s/m^2
Gas μ_G	1.2×10^{-5} N·s/m^2
Interfacial Tension	
Gas-Water σ_{GW}	7.2×10^{-2} N/m
Gas-NAPL σ_{GN}	3.6×10^{-2} N/m
NAPL-Water σ_{NW}	3.6×10^{-2} N/m
Time step	
Initial	0.005 days
Maximum	0.05 days

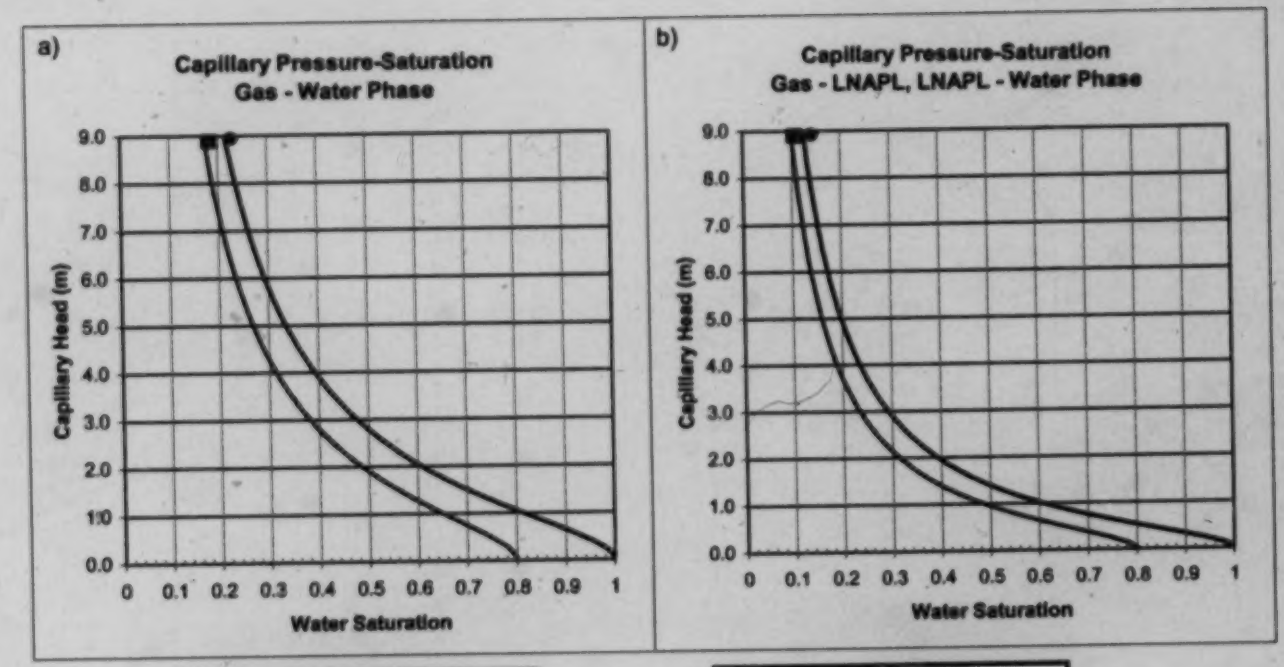

Figure 4.3. Base case capillary pressure-saturation relationship for: a) gas-water phases; and b) gas-LNAPL phases or LNAPL-water phases.

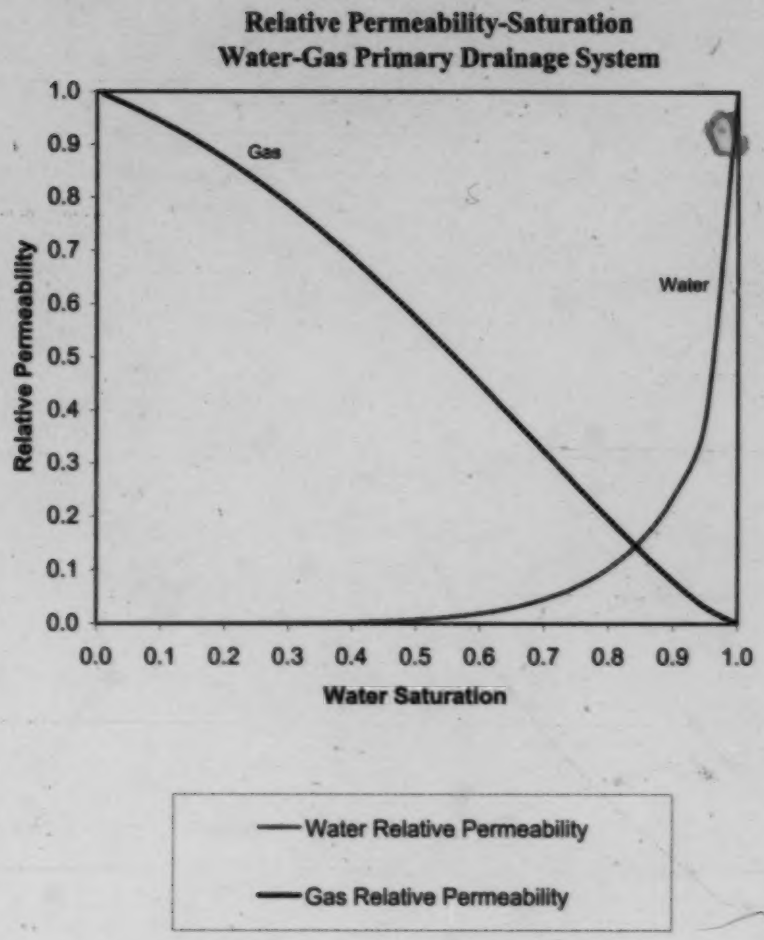

Figure 4.4. Base case relative permeability-saturation curves for primary drainage, water and gas phases.

4.1.5 Infiltration and Initial Redistribution Phase

During the first phase of the simulation, LNAPL infiltrates into the domain, through the boundary nodes designated as the source region in Figure 4.1. Figure 4.5a shows the water saturation (thick black contours), LNAPL saturation (thin shaded contours), and the water table location at the end of the infiltration period (2 days). During infiltration, water and predominantly gas are displaced from the pore space in the unsaturated zone. The maximum LNAPL saturation achieved during infiltration is 0.54, directly beneath the source zone.

Depression of the water saturated region under the source region at the end of the infiltration period is evident on Figure 4.5a. Note that although the water saturated region is depressed, the water table remains at a constant elevation. Directly beneath the source area, the water saturation at the water table, the line of water pressure equal to 0 kPa, has been reduced from 1.0 to 0.70. The location of the 1.0 water saturation contour is approximately 2.5 m lower than before LNAPL infiltration. The cause of this depression is the LNAPL pressure head generated by both the column of free-phase fluid extending up to the surface, 3.0 m, and the pool height of 1.1 m specified above the surface via boundary conditions. The extent of lateral and vertical penetration during the infiltration process is partially due to the lack of a distinct entry pressure in the van Genuchten formulation for the capillary pressure-saturation-relative permeability relationship.

At the end of the 2 day infiltration period, the LNAPL source region is removed and the LNAPL allowed to redistribute for 3 days. The distribution of phases at the end of 5 days of simulation is shown in Figure 4.5b. During the 3 day redistribution period, the LNAPL drains from the area directly underneath the source pool and migrates laterally along the water table. The body of free-phase contaminant becomes lenticular in shape.

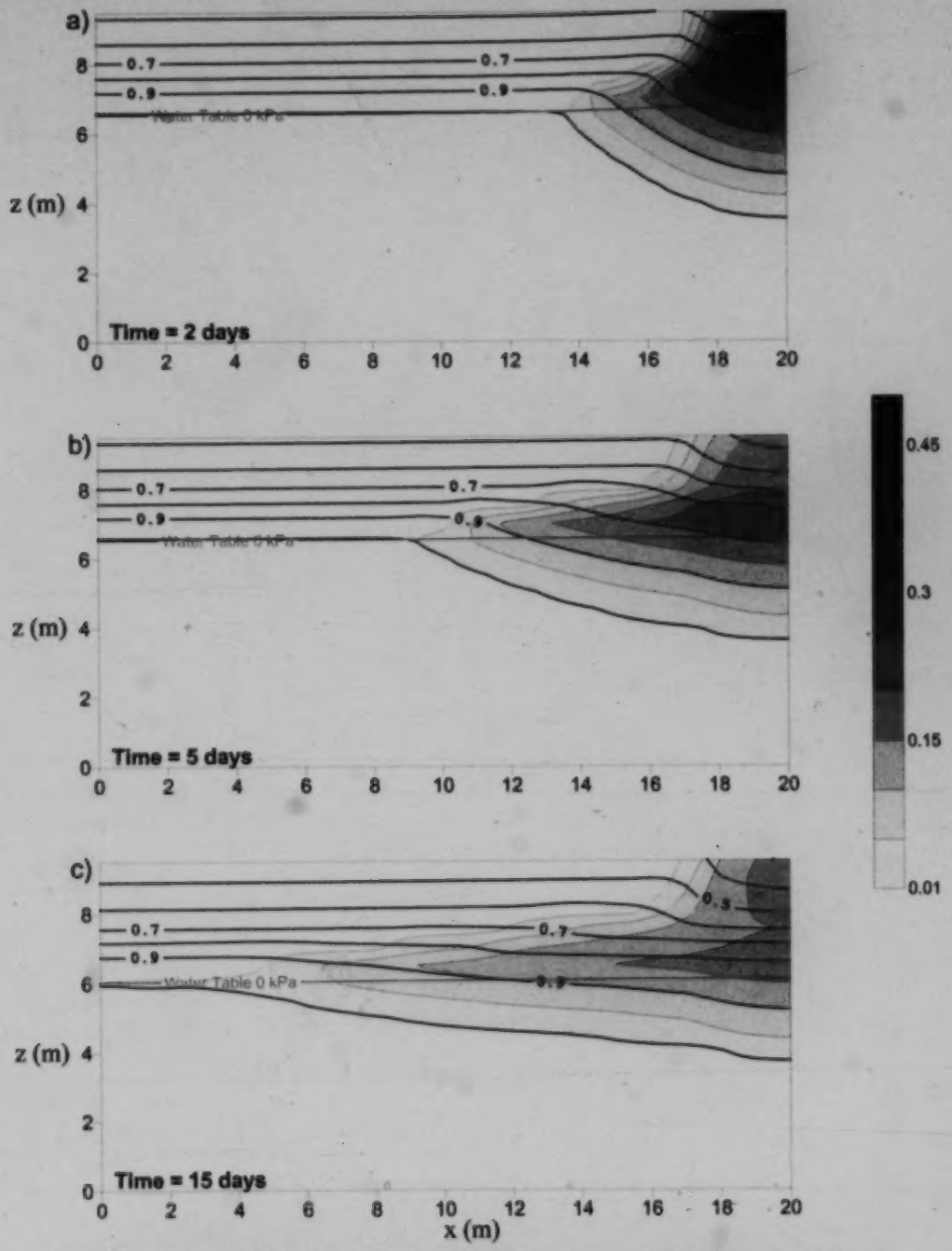

Figure 4.5. Base case simulation results, LNAPL and water saturations at a) 2 days; b) 5 days; c) 15 days. Water saturation is in thick black contours, LNAPL saturation is in thin shaded black contours, and the water table location is marked in grey.

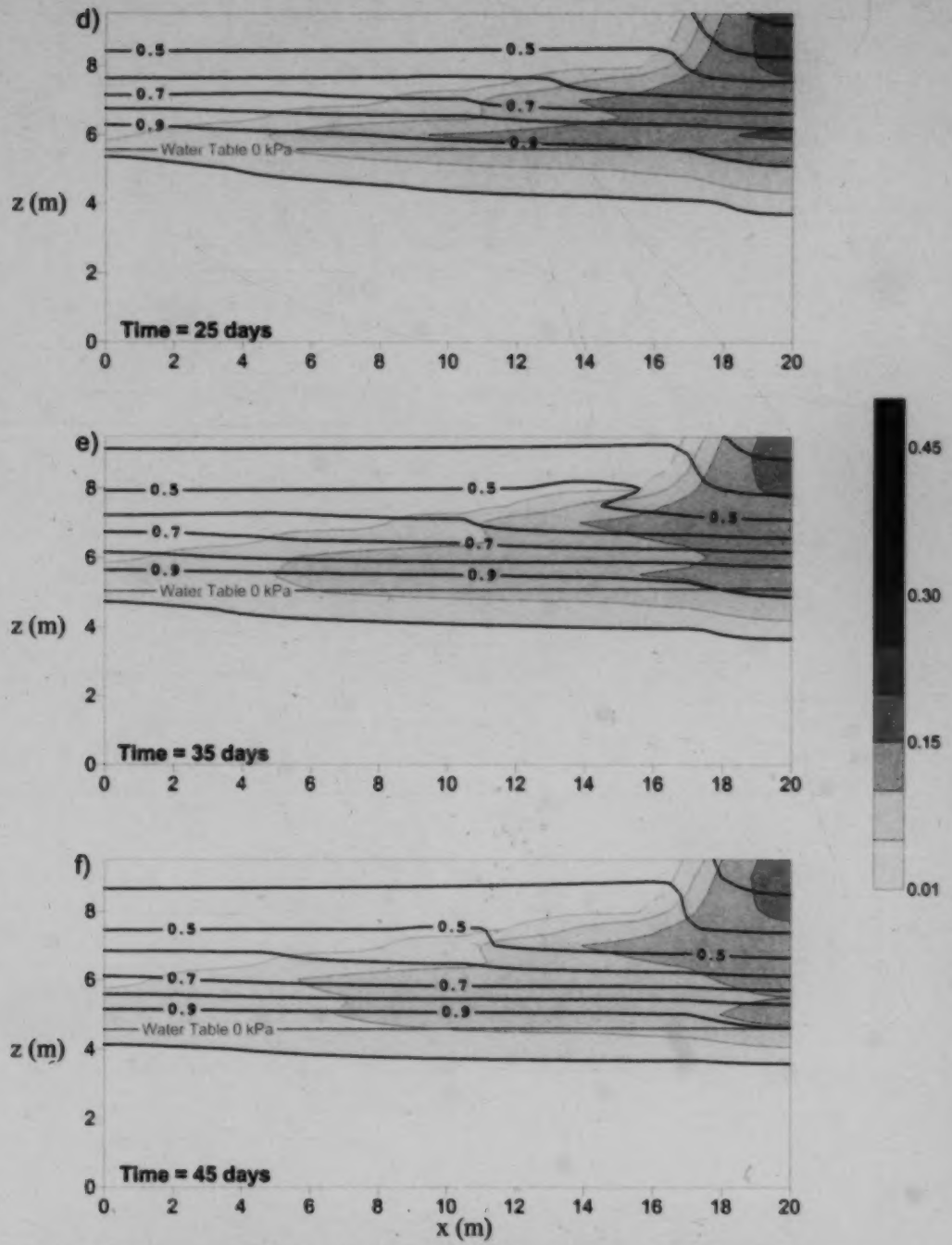

Figure 4.5. Base case simulation results, LNAPL and water saturations at d) 25 days; e) 35 days; f) 45 days. Water saturation is in thick black contours, LNAPL saturation is in thin shaded black contours, and the water table location is marked in grey.

4.1.6 Falling Water Table

At the simulation time of 5 days, the lowering of the water table is initiated at a rate of 0.05 m/d, for a total of 2 m over the course of 40 days. The phase distributions at intervals through this time period are plotted in Figure 4.5c, d, e, and f. The evolution of a large region of relatively low LNAPL saturation is apparent as the pulse of LNAPL spreads laterally along the water table and vertically downwards. Directly under the source area, the LNAPL is present from the surface to approximately 1 m below the water table. By 45 days, Figure 4.5f, the water table has dropped by the full 2.0 m and much of the domain has been occupied by free-phase LNAPL, at saturations ranging from 0.01 to 0.10.

Fingers are present in the total LNAPL distribution, Figure 4.5f. These fingers are a result of the interplay between the trapping process, the water table movement, and the lateral spreading. Figure 4.6 shows a comparison between the total LNAPL saturation, S_N, the trapped LNAPL saturation, S_{Nt}, and the mobile LNAPL saturation, where the mobile LNAPL saturation is defined as $S_N - S_{Nt}$. In the top finger, the total LNAPL saturation is predominantly composed of trapped LNAPL, S_{Nt}, where the total LNAPL saturation is 0.05 at the point and the trapped LNAPL saturation is 0.04. In the lower finger, however, the total LNAPL saturation is mostly composed of free LNAPL, where the free-phase saturation is 0.05 and no trapped saturation is present. At the end of the simulation period, the LNAPL mass in the system has increased by 13% over the initial mass infiltrated, due to numerical error.

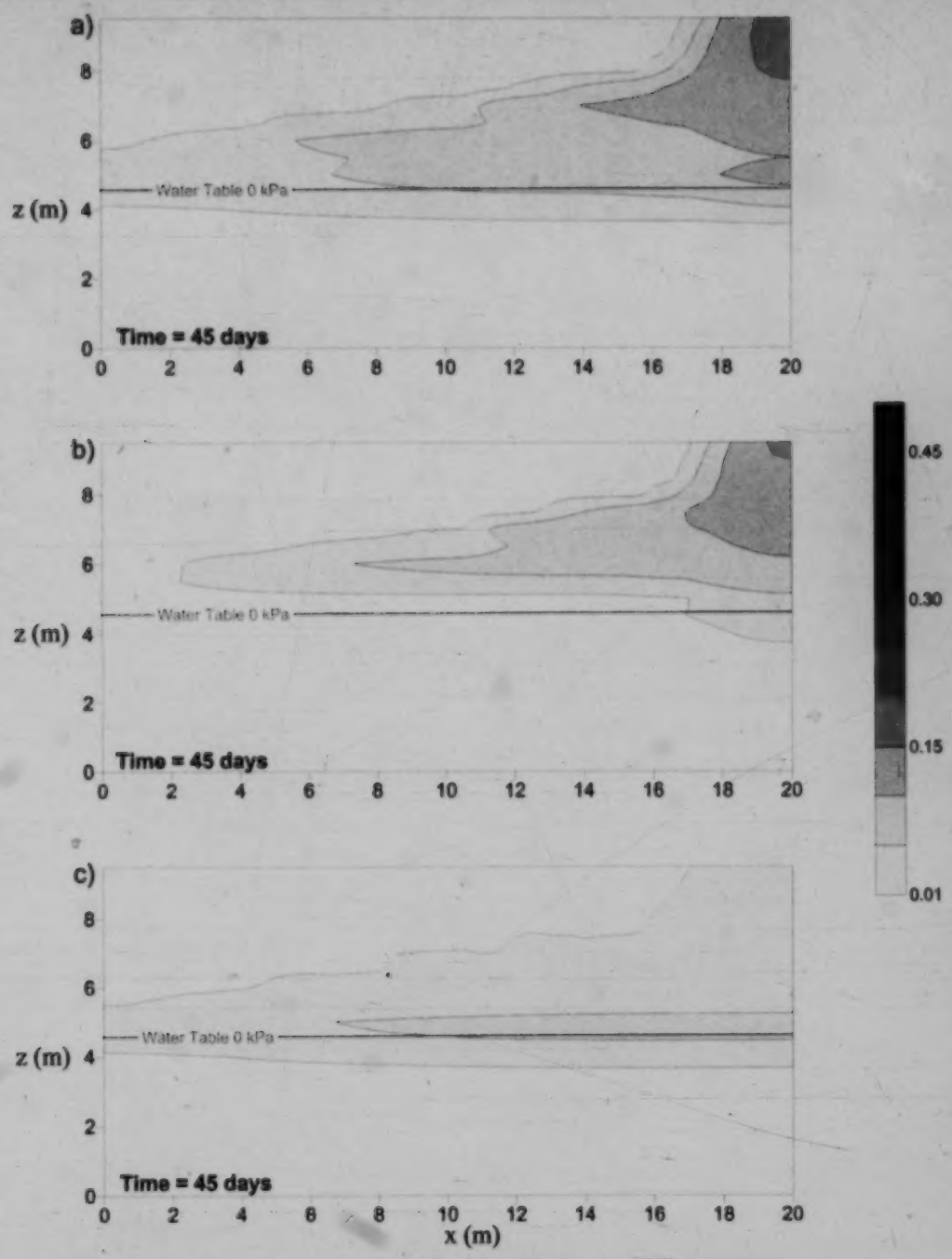

Figure 4.6. Base case simulation results, LNAPL distribution - a) Total LNAPL; b) Trapped LNAPL; and c) Free LNAPL at 45 days. Contours and shading as per Figure 4.5

4.1.7 Trapped LNAPL Distribution

Evolution of the plume of trapped LNAPL during redistribution is shown in Figure 4.8. Section 2.4.3 discusses how the trapped LNAPL saturation is determined as function of the residual LNAPL saturation, the maximum LNAPL saturation achieved at each point, and the current LNAPL saturation. Directly after the infiltration period, at 2 days, no trapped LNAPL is present because each point within the domain is at its maximum LNAPL saturation, S_N^{max}, in Equation 2.29. This means that S_N^{max} and S_N are the same at each nodal location and $S_{Nr}(x,y)$ is zero.

At 5 days, following the static water table redistribution period, trapped LNAPL saturations have evolved within the domain (Figure 4.8b). Most of the trapped LNAPL is present beneath the source area, as the LNAPL drains away from where the pool was present during infiltration. In this area, the trapped saturation ranges from less than 0.02 to greater than 0.08. A small region of trapped saturation is also present in the 4 m to 6 m elevation range, directly beneath the source. This is the location of maximum depression of the water saturation region during infiltration. Once the source area is removed, the LNAPL heads decreased, allowing the water saturated region to rise, trapping LNAPL. The trapped saturation within this region is about 0.02.

As the water table moves downward, from 5 to 45 days, the distribution of trapped LNAPL moves downward and laterally, away from the source region, Figure 4.8c, d, e, and f. By the end of the simulation period, 45 days, the trapped LNAPL distribution has extended down to an elevation of approximately 5 m due to the dropping water table. It has also extended laterally along the sloping water table approximately 17 m down gradient of the source region.

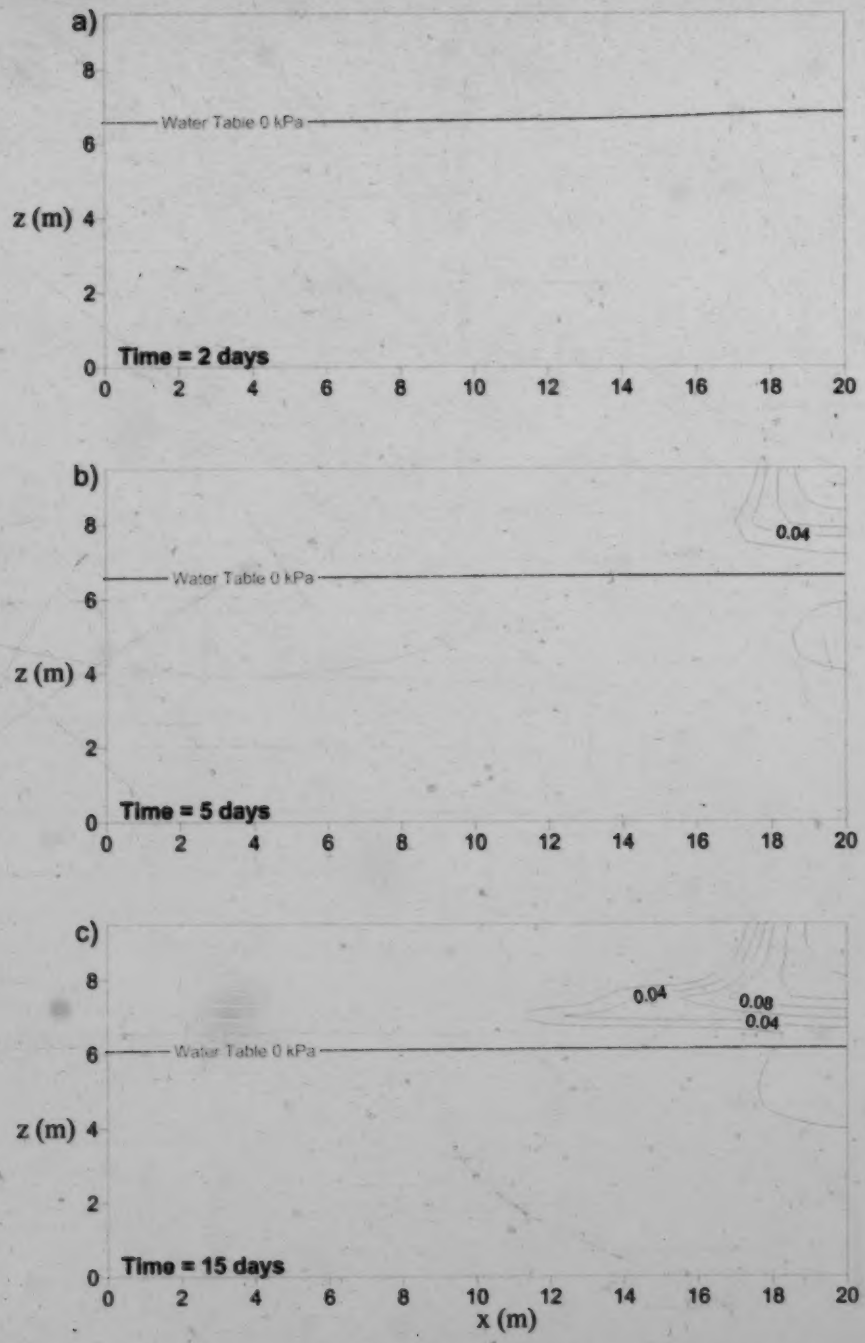

Figure 4.7. Base case simulation results, trapped LNAPL saturation at: a) 2 days; b) 5 days; c) 15 days. Contour interval is 0.02

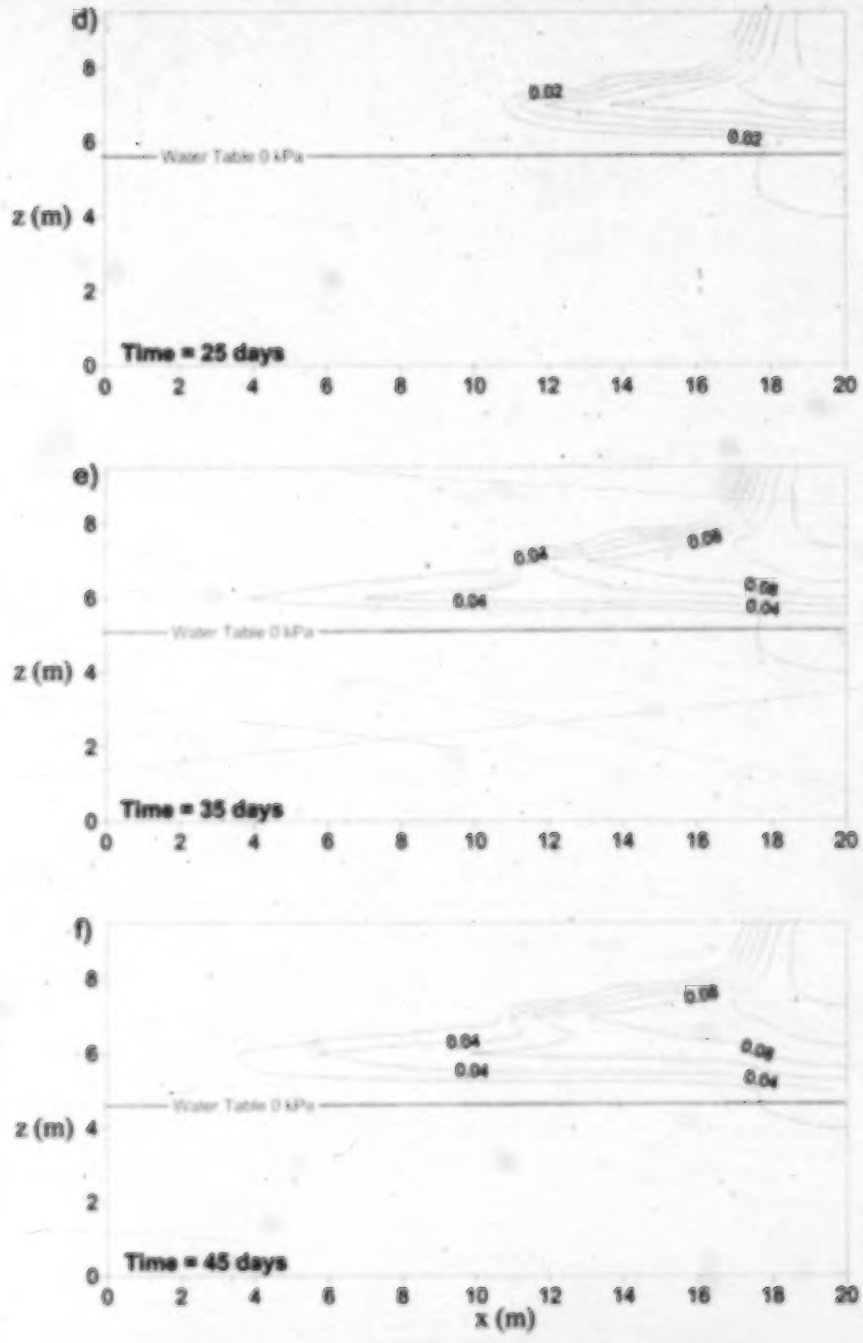

Figure 4.7. Base case simulation results, trapped LNAPL saturation at: d) 25 days; e) 35 days; f) 45 days. Contour interval is 0.02.

4.2 Sensitivity Analysis

A sensitivity analysis is performed to examine the effects of various characteristics of the base case on the LNAPL migration pathways and resulting trapped distribution. A comparison is first made with simulation results for a second numerical model, NAPL Simulator. Next, the effect of specifying a residual water saturation value greater than 0.0 is considered. The importance of the water table gradient is illustrated followed by consideration of the importance of the water table fluctuation. The influences of heterogeneity are also discussed and simulations presented for illustrative purposes. Finally, a discussion of the results and more complex issues related to the direction of water table fluctuation and repetitive cycles of fluctuation are presented.

4.2.1 Numerical Model: NAPL Simulator

The base case simulation is repeated using NAPL Simulator (Guarnaccia et al., 1997) to compare the predictions of migration and trapping behaviour between two finite-element numerical models. Slight differences in the numerical implementation of the boundary value problem between the numerical models are necessary, and are discussed as they arise.

Initial Water Distribution

The water distribution for the base case is calculated by MOFAT directly from the gas-water capillary pressure curve. The NAPL Simulator does not allow for such a calculation and requires that the domain be initially saturated with water. The desired head boundary condition is then applied to allow the water table to drop progressively through the domain, stabilizing at the same locale as in the base case, to generate an initial water and gas distribution. A comparison of the initial water distribution above the water table for the base case simulation, solid square points, and the NAPL Simulator simulation, outline square points, is shown in Figure 4.8 prior to LNAPL infiltration.

The second difference between the two models is that the trapped water saturation, S_{wt}, is defined differently. MOFAT treats S_{wt} as a constant value regardless of the water

saturation history at a particular node. However, NAPL Simulator considers the trapped water saturation to be a path-dependant variable, the value of which scales between 0 and the maximum irreducible water saturation, S_{wr}, depending difference between the current water saturation and the maximum water saturation at that point in space. This results in a difference in the initial water saturation between simulations of ranging from 0.01 and 0.03.

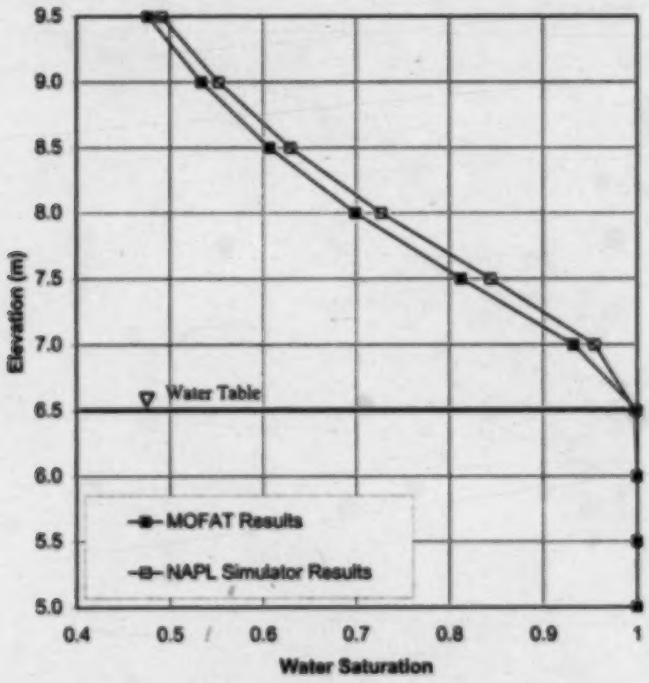

Figure 4.8. Initial water distribution for base case simulation using MOFAT and the comparison case with NAPL Simulator, x = 20 m.

The other difference in implementation between the two models is in the assignment of time-dependent boundary conditions. In MOFAT, boundary conditions can be linearly scaled through time between two values: this is how the basal water pressure boundary is implemented in the base case simulation. The NAPL simulator does not have a comparable utility, so that during the falling water table period the water pressures at the base are incrementally reduced every simulation day by 0.05 m. No apparent

discrepancies are observed between the models as a result of this different implementation.

Infiltration

The phase distributions for the NAPL Simulator simulation are displayed in Figure 4.9. Following the 2 day infiltration period (Figure 4.9a) the distributions look quite similar to the base case (Figure 4.5a). The water saturated region is depressed the same extent, and the saturations with the region immediately beneath the source area are comparable. However, the LNAPL slug in the NAPL Simulator case has not spread laterally along the water table to the same extent as in the MOFAT base case results. This is a general difference between the models, present in the remainder of the results and is likely related to the mass balance error in MOFAT discussed in the base case. The portion of the domain where LNAPL is migrating along the water table is a region where all three phases are mobile and as such is inherently numerically difficult to simulate.

Redistribution

At the end of the unstressed redistribution phase (5 days; Figure 4.9b), the LNAPL contaminated region has a lenticular shape similar to the base case simulation results at 5 days. Prior to the simulation time of 25 days, the pattern of LNAPL look very similar between the base case with MOFAT (Figure 4.5b and c) and the case with NAPL Simulator (Figure 4.9b and c) except for the extended lateral migration along the water table in the base case. The MOFAT results also have a region of slightly higher LNAPL saturation directly beneath the source area, which is also likely a result of numerical error within the MOFAT model. The size of the discrepancy increases with time, reaching a maximum at the end of the simulation period, 45 days.

Comparison plots between the results from MOFAT and NAPL simulator are shown at 25 days (Figure 4.10) and 45 days (Figure 4.11). The upper two plots (a and b) are the results from MOFAT, the lower two plots (c and d) are the results from NAPL Simulator. Plots a and c show the LNAPL saturation, water saturation, and water table location. Plots b and d show the trapped LNAPL saturation. At 25 days (Figure 4.10) the overall

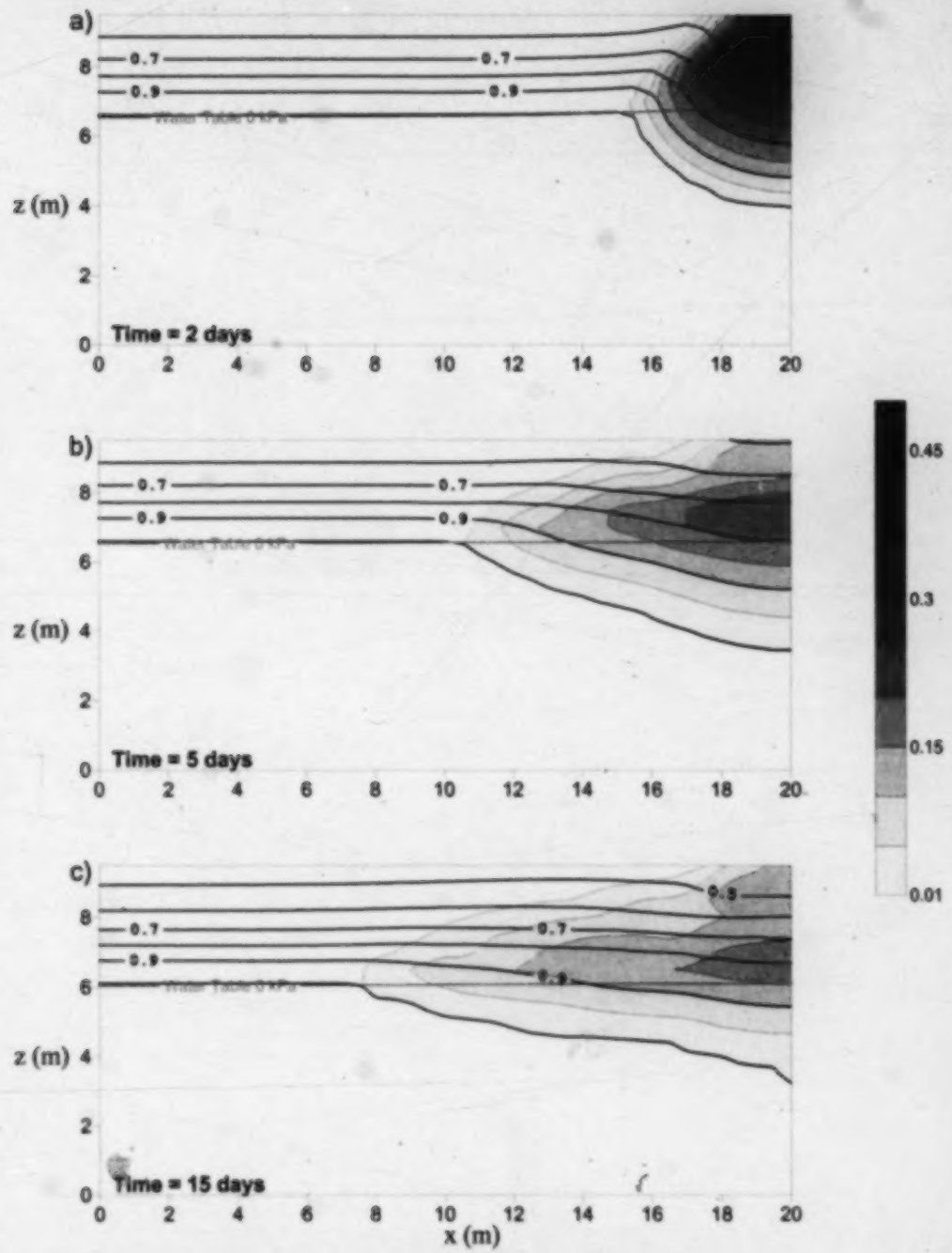

Figure 4.9. NAPL Simulator results, LNAPL and water saturations at a) 2 days; b) 5 days; c) 15 days. Contours and shading as per Figure 4.5.

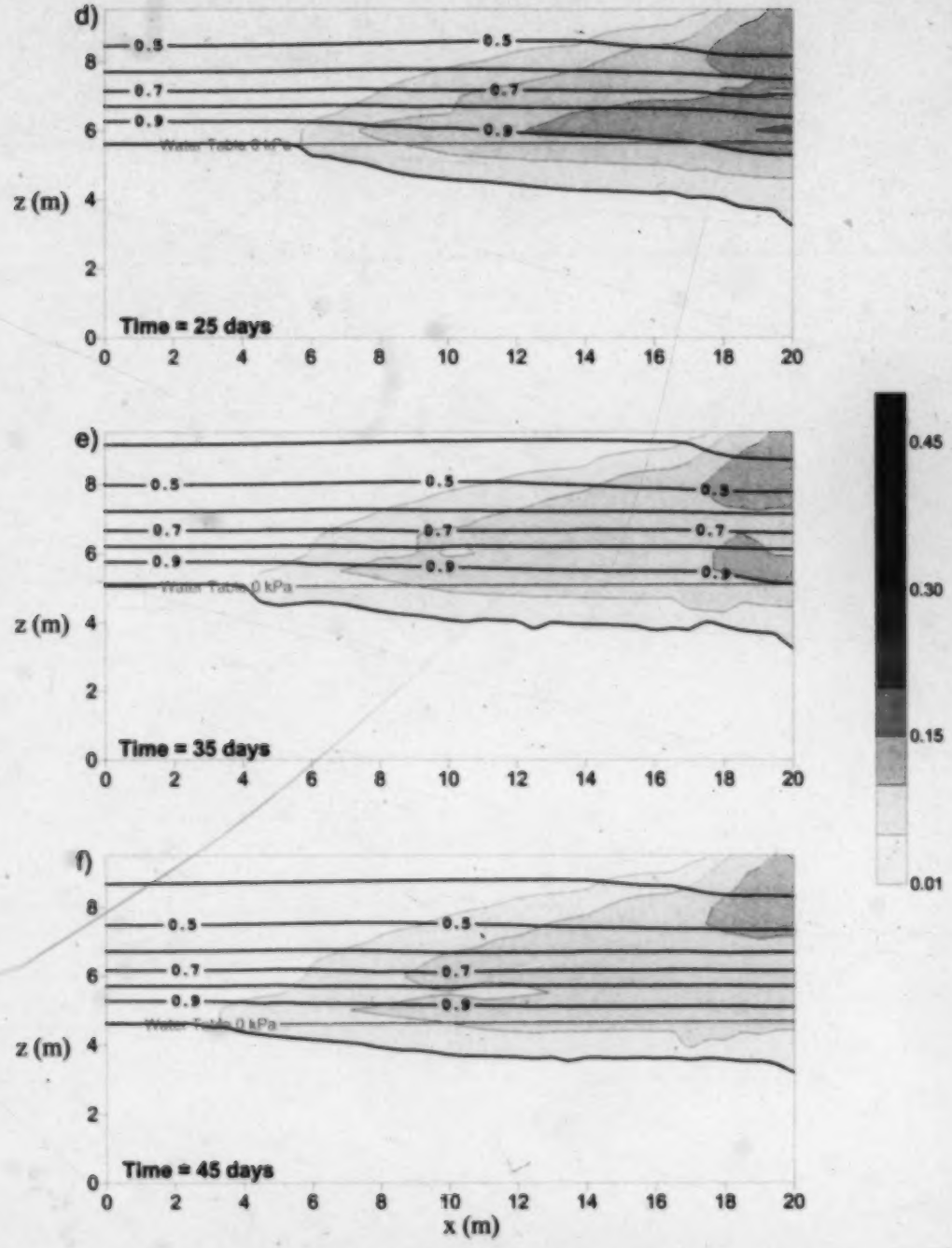

Figure 4.9. NAPL Simulator results, LNAPL and water saturations at d) 25 days; e) 35 days; f) 45 days. Contours and shading as per Figure 4.5.

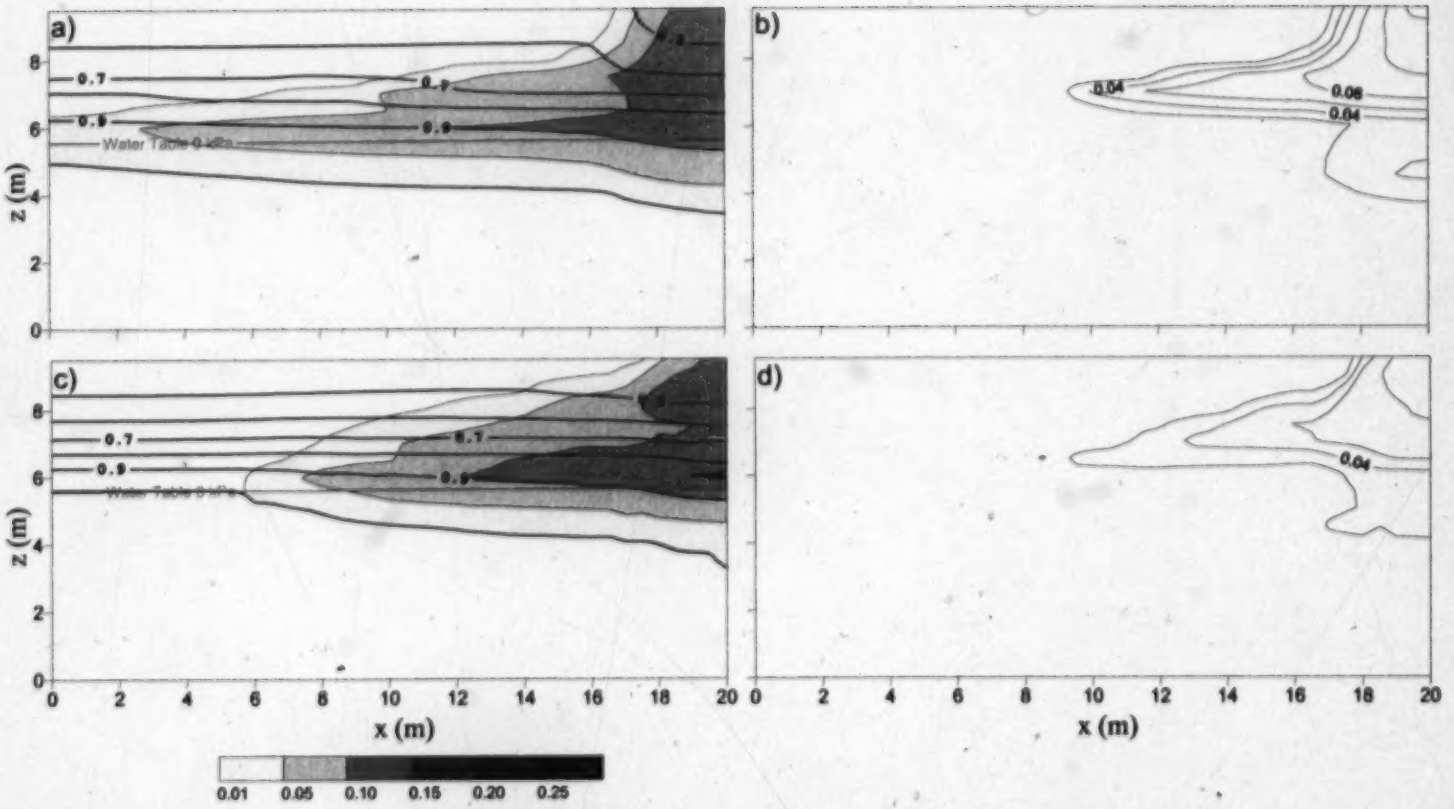

Figure 4.10. Comparison between base case results and NAPL Simulator results, 25 days a) and c) LNAPL and water saturation Contours and shading are as per Figure 4.5.; b) and d) Trapped LNAPL saturation - Contour interval is 0.02.

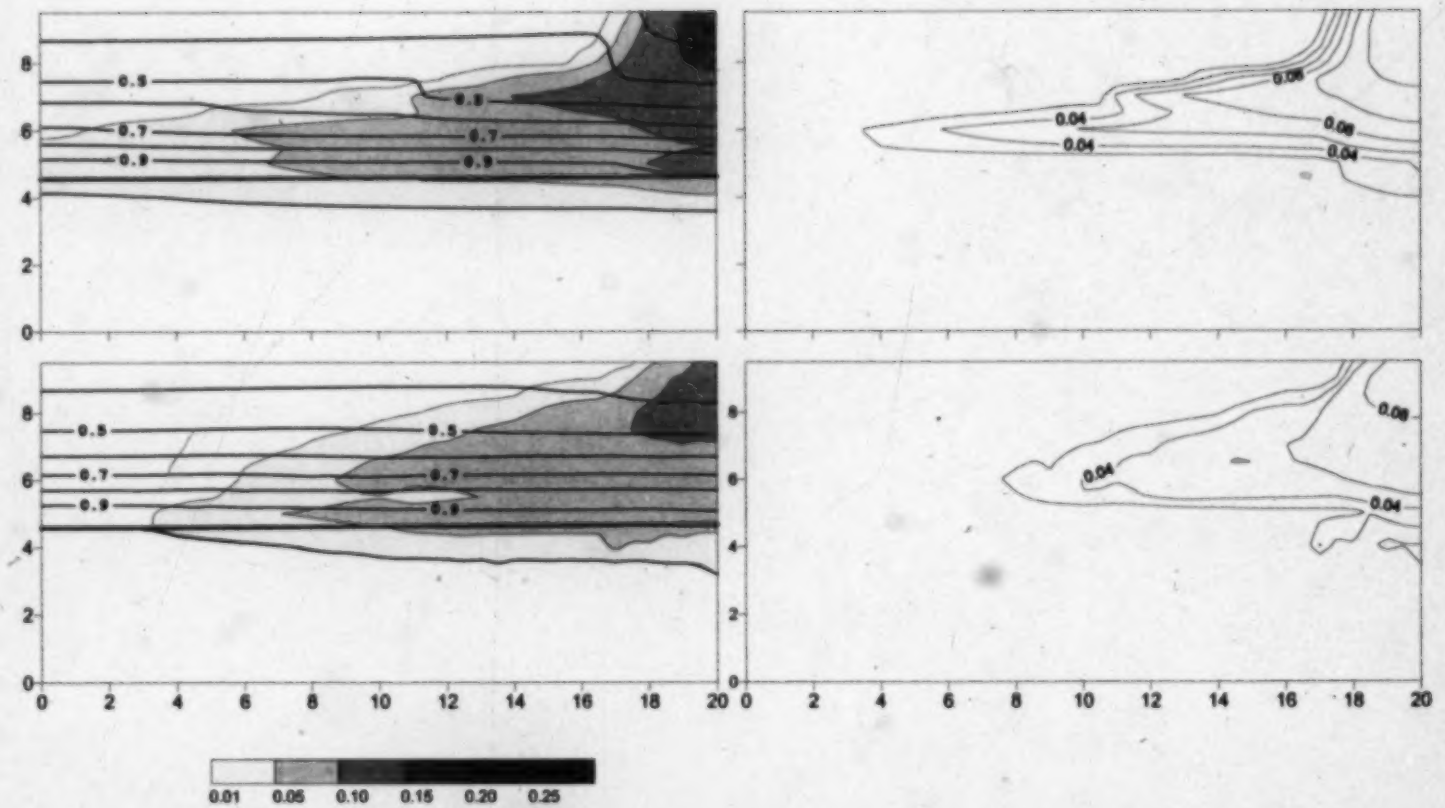

Figure 4.11. Comparison between base case results and NAPL Simulator results, 45 days a) and c) LNAPL and water saturation Contours and shading are as per Figure 4.5.; b) and d) Trapped LNAPL saturation - Contour interval is 0.02.

pattern of the two distributions of trapped LNAPL saturation are the same. Immediately below the source area in the unsaturated zone is the region of highest trapped saturation, ranging up to between 0.12 to 0.14 in MOFAT and between 0.08 to 0.10 in NAPL Simulator. Both sets of results show the same region of low saturations of trapped LNAPL where the water saturated region is depressed by the infiltrating LNAPL. At 45 days (Figure 4.11) the overall pattern is again quite similar between the two cases.

The mass balance error in NAPL Simulator observed in Chapter 3 is present in this simulation, but the impact on the solution is reduced, due to the homogeneous nature of the problem. The increase in LNAPL mass over the simulation period is 2.5%, considerably less than the 13% observed in the base case simulation with MOFAT.

Overall, both numerical models generate similar patterns for migration and trapping behaviour. The differences present are due in part to the treatment of the residual water saturation, residual LNAPL saturation, and numerical error.

4.2.2 Non-Zero Residual Water Saturation

In this simulation the influence of specifying a non-zero residual water saturation, S_{wr}, is investigated using the MOFAT model. A residual water saturation of 0.2 is selected, instead of 0.0 used in the base case simulation. Firstly, the differences in the initial water distribution are examined and explained. Then the LNAPL saturations, migration pathways, and trapping are compared and discussed.

Initial Water Distribution

The initial water saturation distribution prior to LNAPL infiltration for the case of residual water saturation equal 0.20 is shown in Figure 4.12 as the solid triangles. In this case, the water saturation ranges from 0.58 at the top boundary to 1.0 at the water table. The water saturation with no residual is also shown for comparisons. The difference between the two curves is a result of the effect that the residual water saturation, S_{wr}, has on the calculation of water saturation as a function of capillary head. At the top of the

domain, 9.5 m elevation, the difference in the water saturation between this scenario and the base case is 0.1.

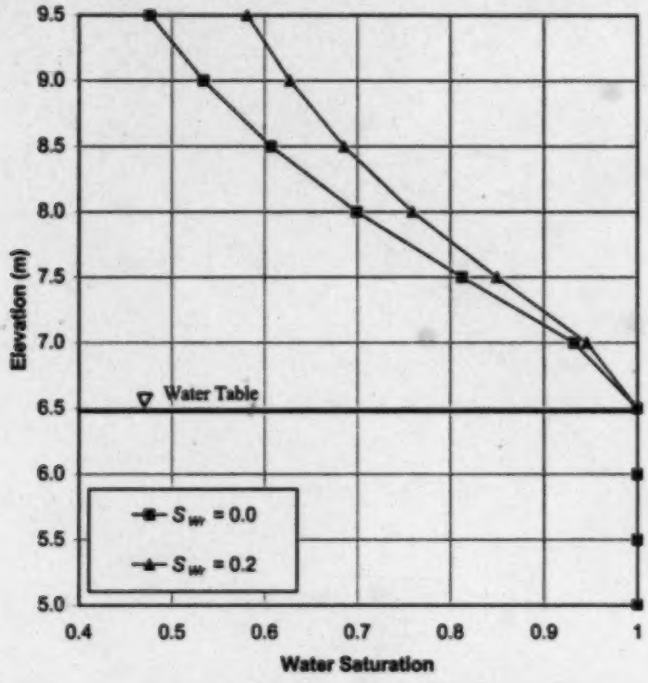

Figure 4.12. Initial water distribution for base case simulation and the comparison case with residual water saturations of 0.2, x = 20 m.

Results

The LNAPL and water distributions for the base case and the case with a non-zero residual saturation are shown in Figure 4.13 and Figure 4.14. The base case results at 25 days are displayed in Figure 4.13a and b, while results from the simulation with a non-zero residual saturation are displayed in Figure 4.13c and d. Figures 4.13a and c show the LNAPL and water saturations, while Figures 4.13b and d show the trapped LNAPL saturations. In the modified simulation, the 0.05 LNAPL saturation contour has progressed futher down gradient compared to the base case results. In the near-source region the LNAPL saturations are lower in the modified simulation, in the range of 0.15-0.20 compared to 0.20-0.25 for the base case. The trapped LNAPL distribution for this

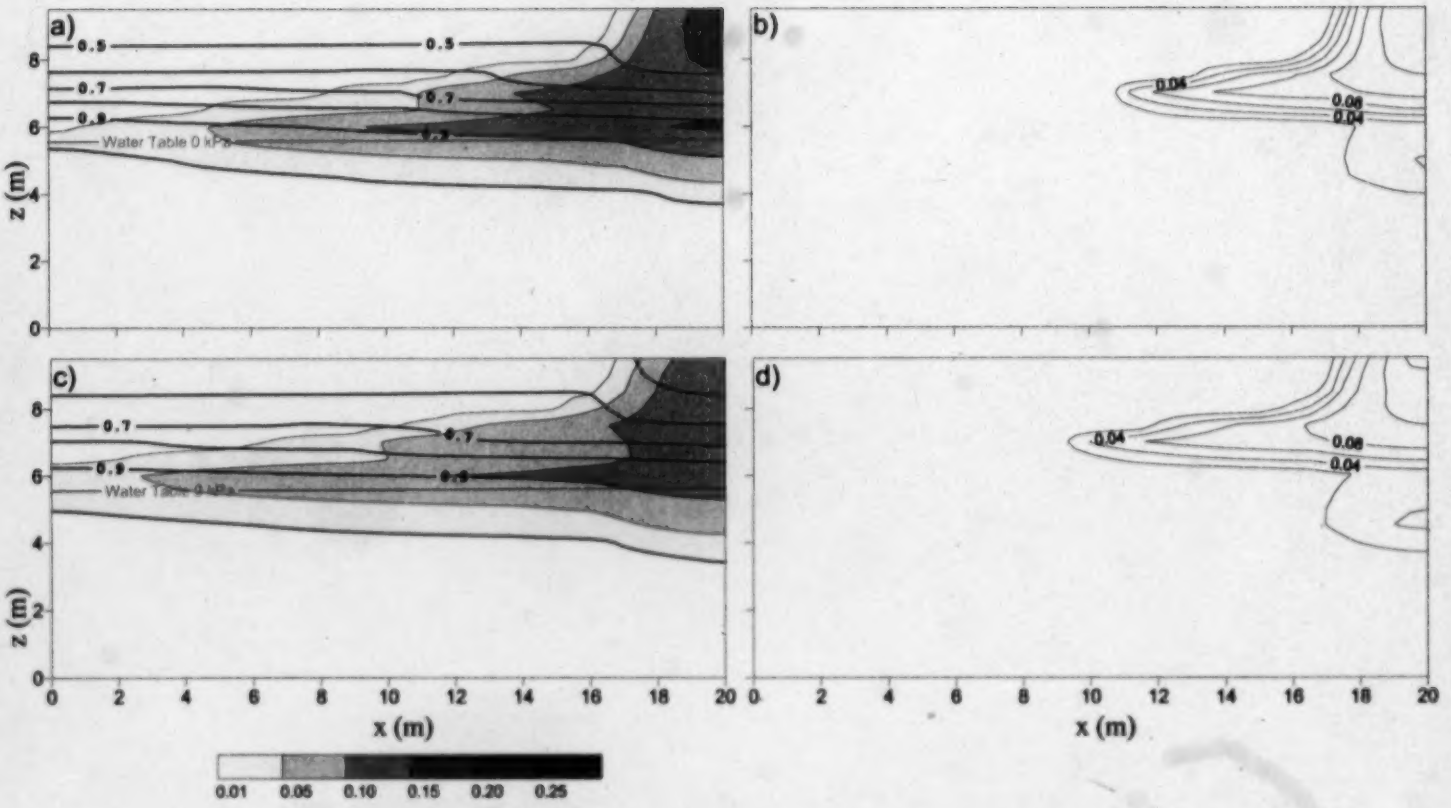

Figure 4.13. Comparison between base case and Swr=0.20 cases, 25 days a) and c) LNAPL and saturation. Contours and shading as per Figure 4.5; b) and d) Trapped LNAPL saturation. Countour interval is 0.02.

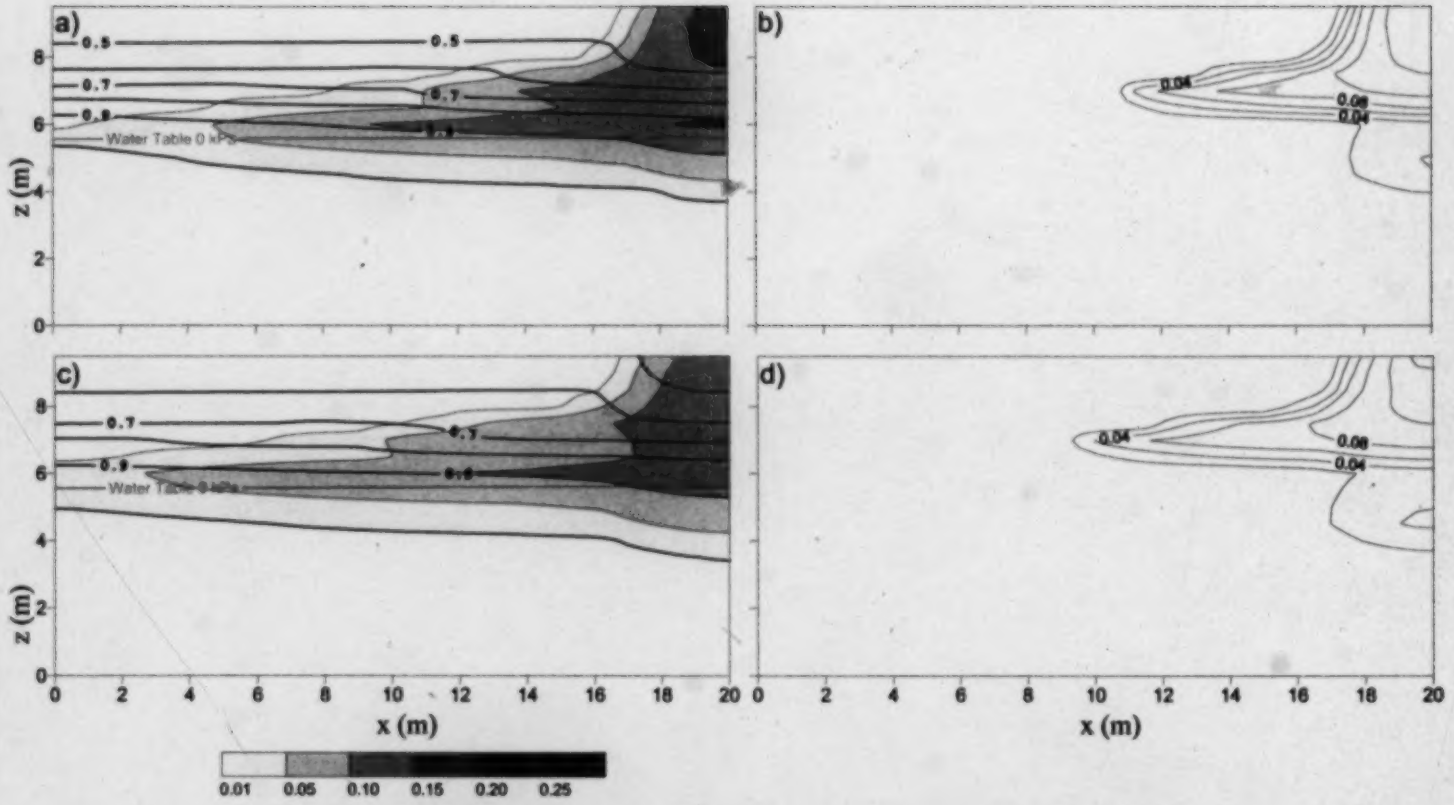

Figure 4.13. Comparison between base case and Swr=0.20 cases, 25 days a) and c) LNAPL and saturation. Contours and shading as per Figure 4.5; b) and d) Trapped LNAPL saturation. Countour interval is 0.02.

sensitivity scenario reflects these differences in that the 0.02 contour has progressed further down gradient and the source region has lower trapped saturations than in the base case. At the end of the simulation, 45 days, the same patterns are evident (Figure 4.14). The 0.05 LNAPL contour has progressed down gradient, more pronounced fingering is present, and the source zone saturations are lower.

These differences between the two simulations are caused by the presence of the trapped water phase. The residual water saturation affects both the area available for LNAPL flow and the constitutive relationships relating capillary pressure, saturation, and relative permeability. Trapped water reduces the available pore space into which the LNAPL can invade, thereby increasing the lateral and vertical spreading of the LNAPL region, which must occur for the specified 0.8 m^3 of LNAPL to infiltrate. Because the relative permeability relationships employ the effective phase saturations, the presence of the trapped water phase causes an increase in the relative permeability at the same absolute LNAPL saturation. Therefore, LNAPL can migrate faster and further through the domain than if no trapped water is present.

4.2.3 Water Table Gradient

The water table plays a crucial role in the lateral migration of LNAPL. The impact of the water table gradient on LNAPL behaviour is examined in this section. Figure 4.15 shows a comparison between the base case simulation results at 45 days, with a water table gradient of 0.005 m/m, and results with no water table gradient (*i.e.*, 0.0 m/m). In the case with no gradient, the water table is at an elevation of 6.6 m. A value of 0.0 was used for the residual water saturation, S_{wr}. The lower water table gradient results in less lateral spreading; a spatial shift in the 0.02 saturation contour is evident. The contour is retarded by approximately 1.5 m when there is no gradient on the water table. In the regions of higher trapped saturation, the contours are more closely space when no gradient is present. This reduction in lateral spreading results in higher LNAPL heads above the water table beneath the source zone, an increased depression of the top of the water saturated region by LNAPL, and more trapping of LNAPL in region beneath the water table.

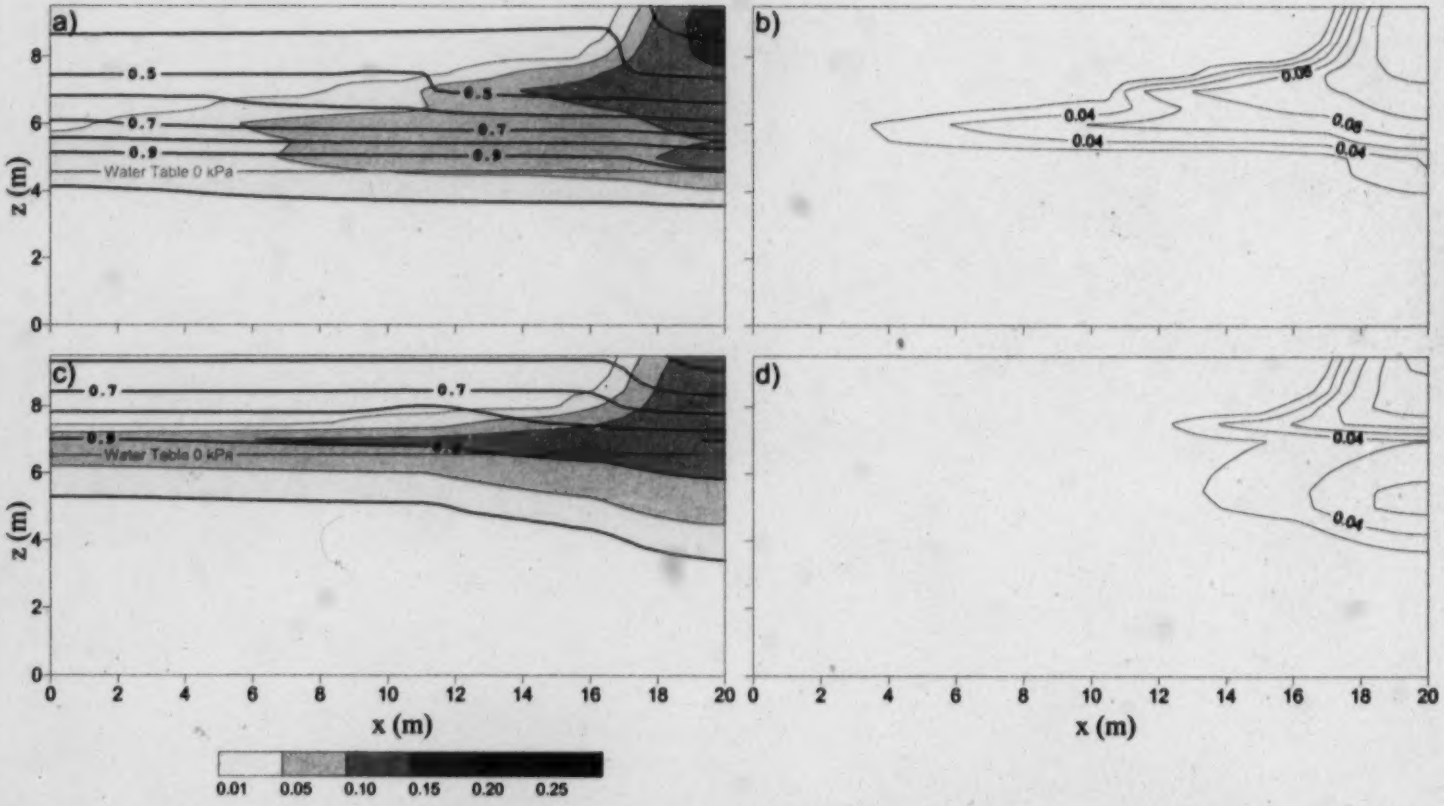

Figure 4.17. Comparison between base case and stable water table cases, 45 days a) and c) LNAPL and water saturation. Contours and shading as per Figure 4.5; b) and d) Trapped LNAPL saturation. Contour interval is 0.02

LNAPL infiltrating into the subsurface in sizeable volumes will pool on the water table, causing depression of the water saturations. Therefore the gradient of the water table will influence the migration of the free-phase product. The amount of lateral spreading is dependent on the gradient, but spreading will still occur as a result of capillary gradients along the edges of the LNAPL pool.

Again, the degree of difference between a gradient of 0.005 and 0.0 m/m is influenced by the representation of the capillary pressure-saturation-relative permeability function employed by the numerical model. The van Genuchten functional relationship causes the LNAPL front to spread out, and likely reduces the importance of the water table gradient, by increasing the relative importance of the capillary driving force.

High water table gradients, with increased spreading, result in a thinner LNAPL pulse migrating quickly away from source zone (results not shown). The degree of depression of the water saturated region will be reduced due to the increased lateral migration.

4.2.4 Water Table Fluctuation

The rate of the water table fluctuation is important for trapping and migration. Figure 4.16 shows a comparison between the phase distributions and the trapped LNAPL distribution for the base case and for a static water table at 45 days. The static water table results in a thin, laterally extensive plume of mobile LNAPL. The flow regimes are markedly different in these two cases. In the base case, the LNAPL pulse follows the water table downwards, and the extent of depression of the water saturated region is smaller than in the static water table case. The reduced depression is controlled by the relative permeability relationships: the water near the water table is much more mobile than the LNAPL, so it migrates downward and the LNAPL follows.

Although the initial LNAPL distribution after infiltration is identical, more LNAPL is trapped beneath the water table in the 4 to 6 m interval in the static water table case at 25 days. This is because the water saturated region is rebounding, and it rebounds more in the static case because the water table is higher at 25 days. By 45 days (Figure 4.17)

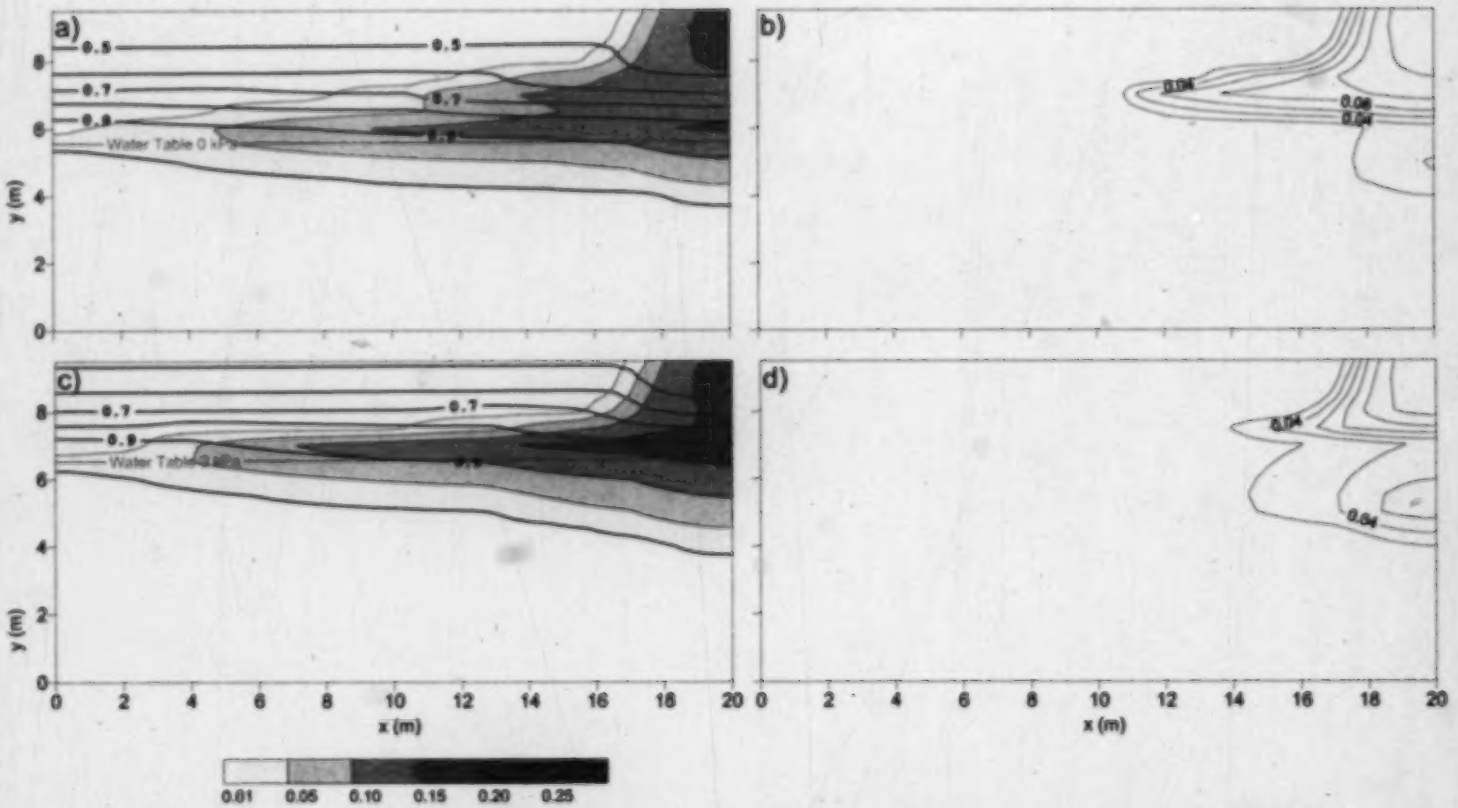

Figure 4.16. Comparison between base case and stable water table cases, 25 days a) and c) LNAPL and water saturation. Contours and shading as per Figure 4.5; b) and d) Trapped LNAPL saturation. Contour interval is 0.02

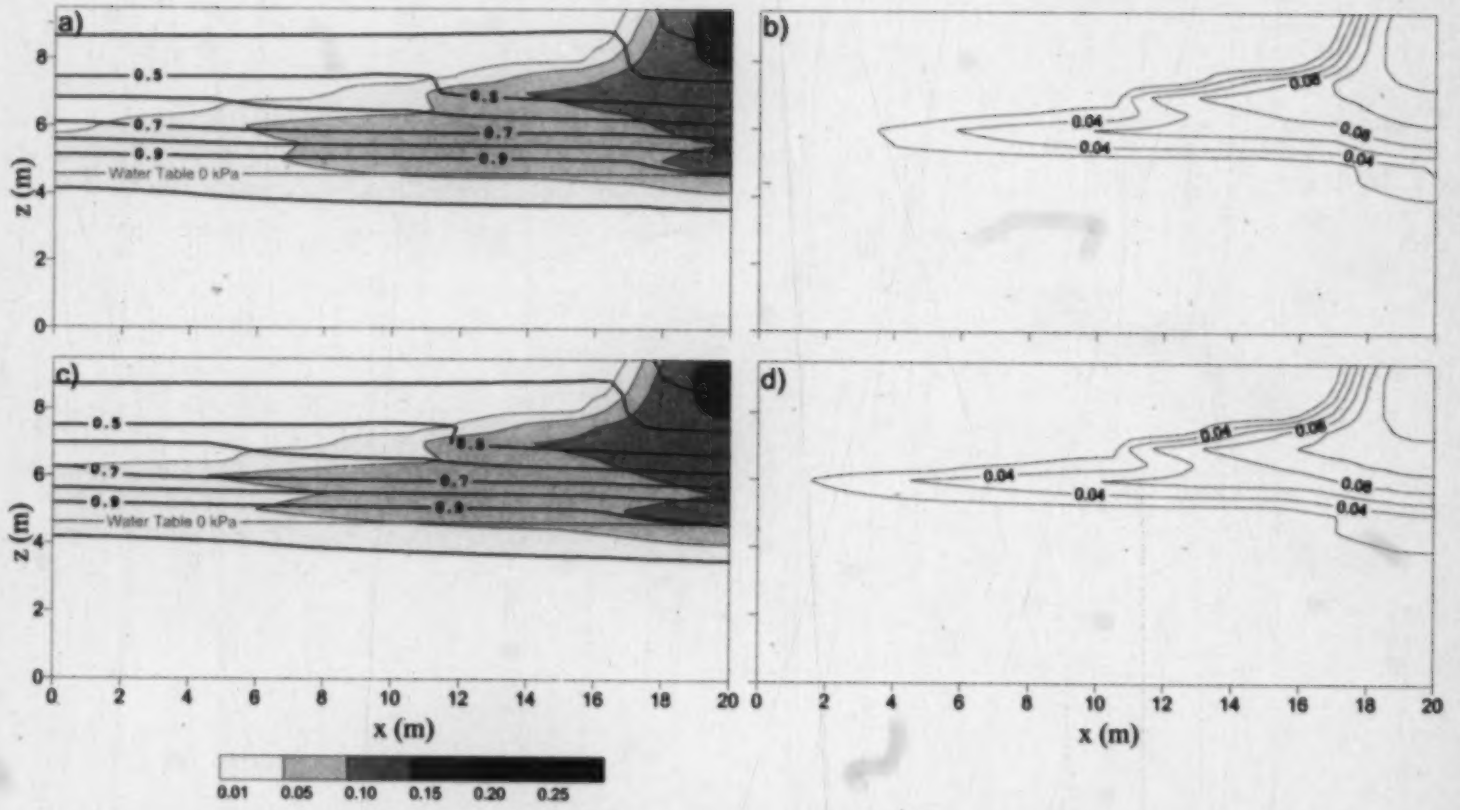

Figure 4.15. Comparison between base case and flat water table, 45 days a) and c) LNAPL and water saturation. Contours and shading as per Figure 4.5; b) and d) Trapped LNAPL saturation. Contour interval is 0.02.

similar quantities are trapped in this region, but in different configurations. At 45 days, a much larger fraction of the LNAPL is still mobile in the situation of a static water table. The region of trapped LNAPL is still focused in the near source area, but it is evident from the profile that through time the LNAPL distribution will evolve predominantly along the water table location.

Increasing the rate at which the water table falls causes the mobile and immobile LNAPL profiles to be more vertically extensive. Rapidly rising water tables have the potential to effectively isolate larger bulbs of LNAPL at mobile saturations due minor heterogeneities and flow channeling.

4.2.5 Heterogeneity

The presence of heterogeneity in the subsurface can play a significant role in fluid behaviour. Multiphase flow problems are particularly sensitive to heterogeneities, since pores sizes affect both flow rate (permeability) and accessibility (capillary pressure). This portion of the study examines the impact of simple heterogeneities, specifically a single lens, within a homogeneous host medium. The effects of these heterogeneities emphasize the importance of attempting to quantify porous media distributions.

The behaviour of a lens is dependent not only on relative intrinsic porous media properties, but also on the water saturation at the given point in time. In a three-phase system, lenses can act as either a sink for the LNAPL phase with respect to the surrounding medium or as capillary barriers, depending on the water saturation within the lens, which is a function of the capillary pressure-saturation curve and the water table location. This is because the LNAPL phase has intermediate wettability: it is more wetting than the gas phase, but less wetting than the water phase.

Figure 4.18 shows four different scenarios of lenses and water table locations. The distribution of gravity and capillary forces vectors for the each lens situation is depicted. In each scenario, the gravity vector is directed downward: into the lens on the top and out of the lens at the base. In contrast, the capillary vectors point either inwards or outwards

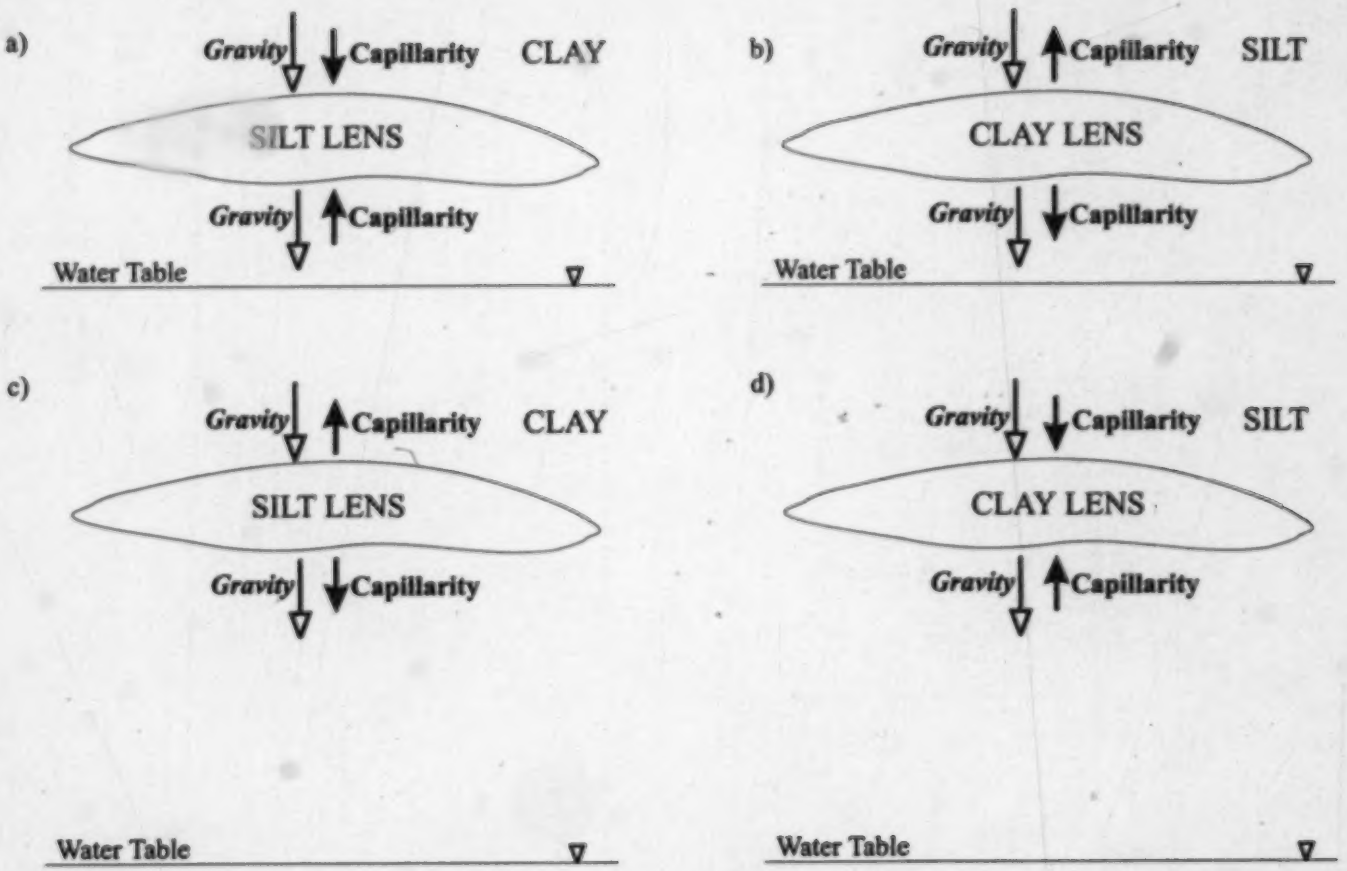

Figure 4.18. Orientation of gravity and capillary force vectors adjacent to lenses: a) and c) are coarser grained lenses within a finer material; b) and d) are finer grained lenses within a coarser material. a) and b) represent situations with the water table near the lens; c) and d) represent situations with the water table far beneath the lens.

from the lens, regardless of the position along the lens interface. In Figure 4.18a, a coarser grained lens is located near the water table. The capillary force vector at the top of the lens is directed inwards. Thus, in this instance the lens will act as a sink for the LNAPL with respect to the surrounding porous medium. At the base of the lens, the inward vector causes pooling to occur at the base of the lens.

The same lens is shown in Figure 4.18c, but the water table is located significantly beneath the lens. In this case the capillary vectors are directed outward from the lens, and it will act as a capillary barrier. A finer-grained lens located near the water table, Figure 4.18b, will act in a similar manner. The same finer-grained lens high above the water table, Figure 4.18d, will act as a sink, as the capillary force vectors are directed inward.

The direction of the capillary vectors, and subsequently the lens behaviour changes because LNAPL is the intermediate wetting phase. LNAPL is the wetting phase when a two-phase gas-LNAPL system is considered, and the non-wetting phase when a two-phase LNAPL-water system is considered. Near the water table, the water saturations of both the fine-grained and coarse-grained soils is essentially unity prior to LNAPL arrival. Therefore the infiltrating LNAPL is the non-wetting phase and the infiltration in the lens is a drainage process. Under drainage conditions significantly more LNAPL can invade the pores of a coarse-grained material than a fine-grained material at the same capillary pressure. As a result, a coarse-grained lens near the water table will act as a sink for LNAPL with respect to the surrounding medium (Figure 4.18a) and a fine-grained lens will act as a barrier (Figure 4.18b).

High above the water table, the situation is reversed, both media are substantially desaturated of water. In the coarse-grained material, any water present is immobile. Therefore LNAPL acts as the wetting phase, with respect to the gas already in the pores. The invasion of LNAPL is therefore an imbibition process, and the fine-grained lens acts as a sink with respect to the surrounding medium (Figure 4.18d) and the coarse-grained lens acts as a barrier (Figure 4.18c).

This concept was demonstrated for an infiltrating oil spill by Schroth et al. (1998a,b) for a sloping interface between finer material overlying coarse material. Their work was strictly interested in the water saturation above the interface, which was controlled by varying the influx rate of water along the top of the model domain.

To illustrate this behaviour, a number of scenarios are considered below using the MOFAT model. Firstly, a fine-grained lens is incorporated into the base case simulation domain and comparisons are made to the LNAPL migration pathways and the trapped LNAPL saturation pattern. The permeability of the lens, k, is 3.54×10^{-13} m^2, the van Genucthen parameter a is 0.3 m and the van Genucthen parameter n is 1.5. Properties for the surrounding porous media are as for the base case (Table 1). The initial water table is at the same location as in the base case.

Three subsequent cases are then presented. In these cases it was desired to increase the contrast in capillary behaviour between the lens and surrounding medium. The van Genuchten parameters, a and n, for the coarse-grained material are set to 1.2 m and 2.4, respectively. The primary drainage capillary pressure-saturation relationships are shown in Figure 4.19 for the coarse-grained (a) and fine-grained porous media (b). The permeability of the fine-grained material is increased to 1.77×10^{-12} m^2. The residual water saturation, S_{wr}, is changed from 0 to 0.2 for both porous media. In these cases the source area and the lens are shifted laterally towards the centre of the domain to reduce boundary effects, and the grid discretization is refined so that elements are now 0.25 m by 0.25 m and the entire domain is only 4.75 m tall and 10 m wide.

Fine-Grained Lens

The simulation results from the case of a fine-grained lens placed directly beneath the source area are shown in Figure 4.20 at 45 days simulation time. The simulation scenario is the same as for the base case: the LNAPL is allowed to infiltrate into the domain as describe above until 0.8 m^3 invaded. As with the base case simulation, the infiltration period took 2 days.

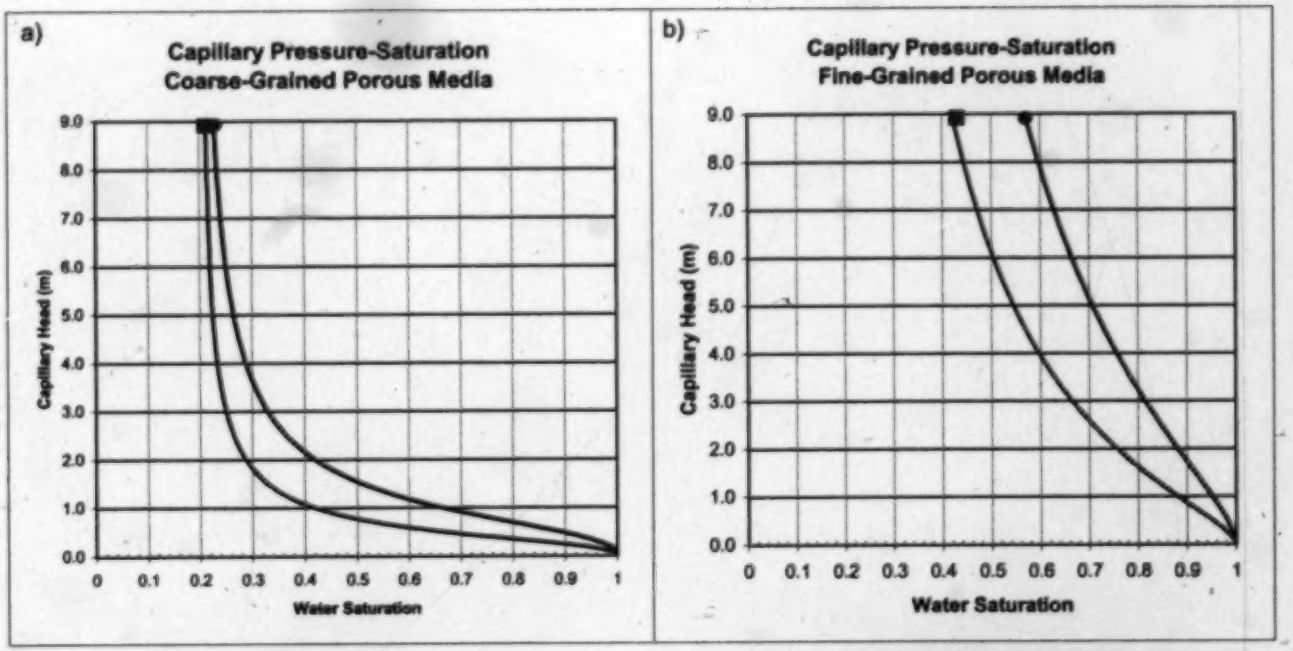

Legend
Gas-Water
Gas-LNAPL, LNAPL-Water

van Genuchten Parameters		
	Coarse-Grained	Fine-Grained
a	1.2	0.3
n	2.4	1.5
S_{wr}	0.2	0.2
S_{nr}	0.2	0.2

Figure 4.19. Primary drainage capillary pressure-saturation relationship for: a) coarse-grained porous media; and b) fine-grained porous media

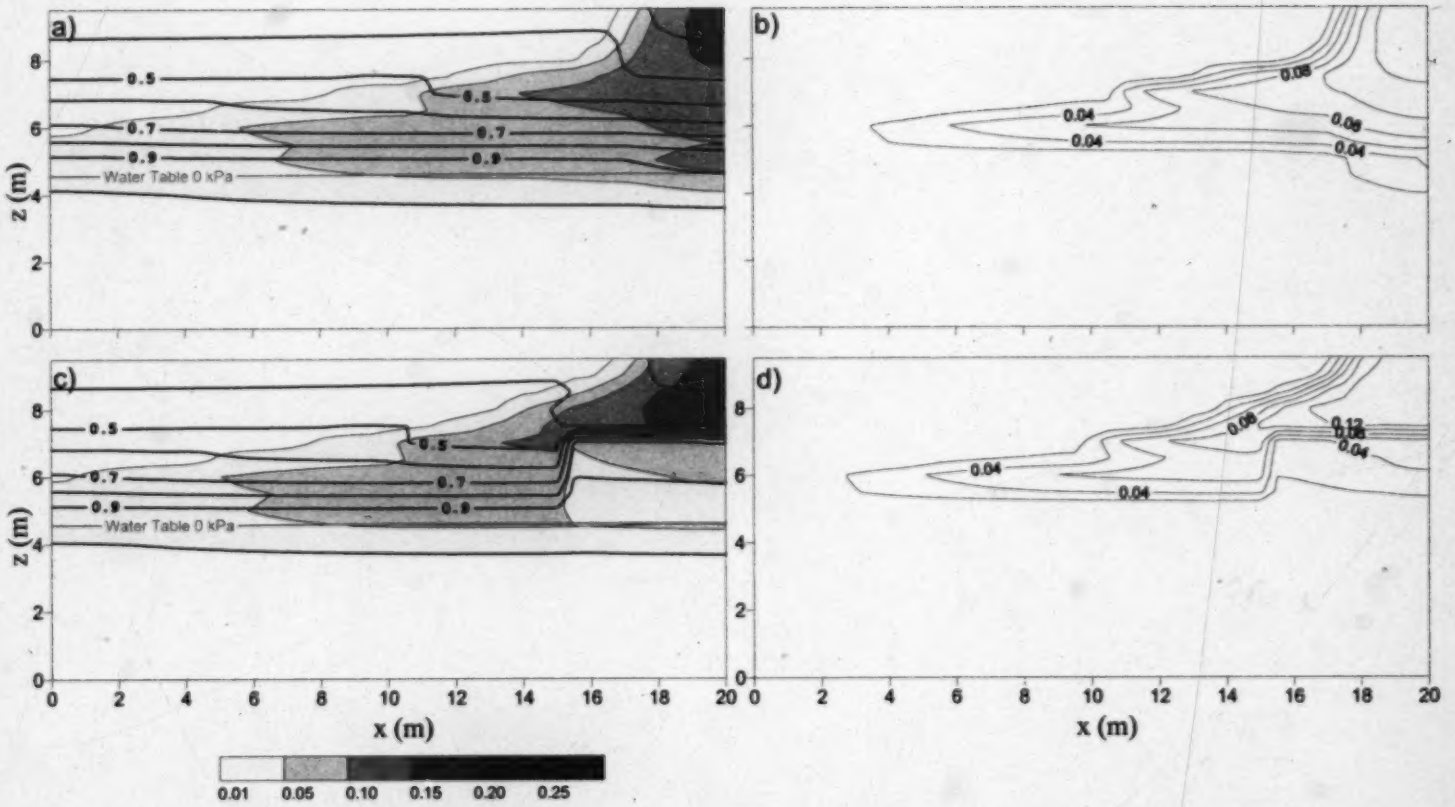

Figure 4.20. Comparison between base base and fine-grained lens, 45 days a) and c) LNAPL and water saturation. Contours and shading as per Figure 4.5; b) and d) Trapped LNAPL saturation. Contour interval is 0.02.

Figure 4.20c shows the distribution of LNAPL and water at the end of 45 days simulation period. The LNAPL, migrating down beneath the source area, encounters the top of the fine-grained lens and is diverted along the interface. Once the edge of the lens is encountered, the free-phase product begins its vertical descent again. Within the host porous medium, fingering of the LNAPL distribution is evident, similar to the base case.

A comparison between the trapped LNAPL distribution for the base case simulation and this simulation is shown in Figure 4.20b and d. Higher trapped saturations are present directly beneath the source area, as a result of the higher maximum LNAPL saturations in this area, caused by the lens acting as barrier. The top edge of the lens is evident where the trapped saturation contours are very close together. The side of the lens is located at 15 m, where the contours bend from horizontal to almost vertical. Across the lens interface, the difference in trapped saturation is 0.04 to 0.12 on the top and 0.02 to 0.08 along the left side of the lens.

To illustrate the different behaviour of a fine-grained lens, the refined grid discussed above is used. Figure 4.21 shows results from a simulation with a similar fine-grained lens, with silty-clay properties, encased in a coarse-grained material, with fine sand properties, where the water table is located 6 m below the base of the domain. In this simulation the permeability of the fine-grained lens is increased to 1.77×10^{-12} m^2. To enhance the capillary effects, the properties of the coarse-grained material are modified as follows: a is increased to 1.2 m and n is increased to 2.4.

The initial water saturation profile with depth is shown in Figure 4.22a. The water saturation in the coarse grained material above the lens is 0.23, while the top of the fine-grained lens is 0.66.

The LNAPL migration behaviour, and subsequent trapping behaviour, in this case is quite different than previously illustrated. The infiltrating LNAPL still migrates downward

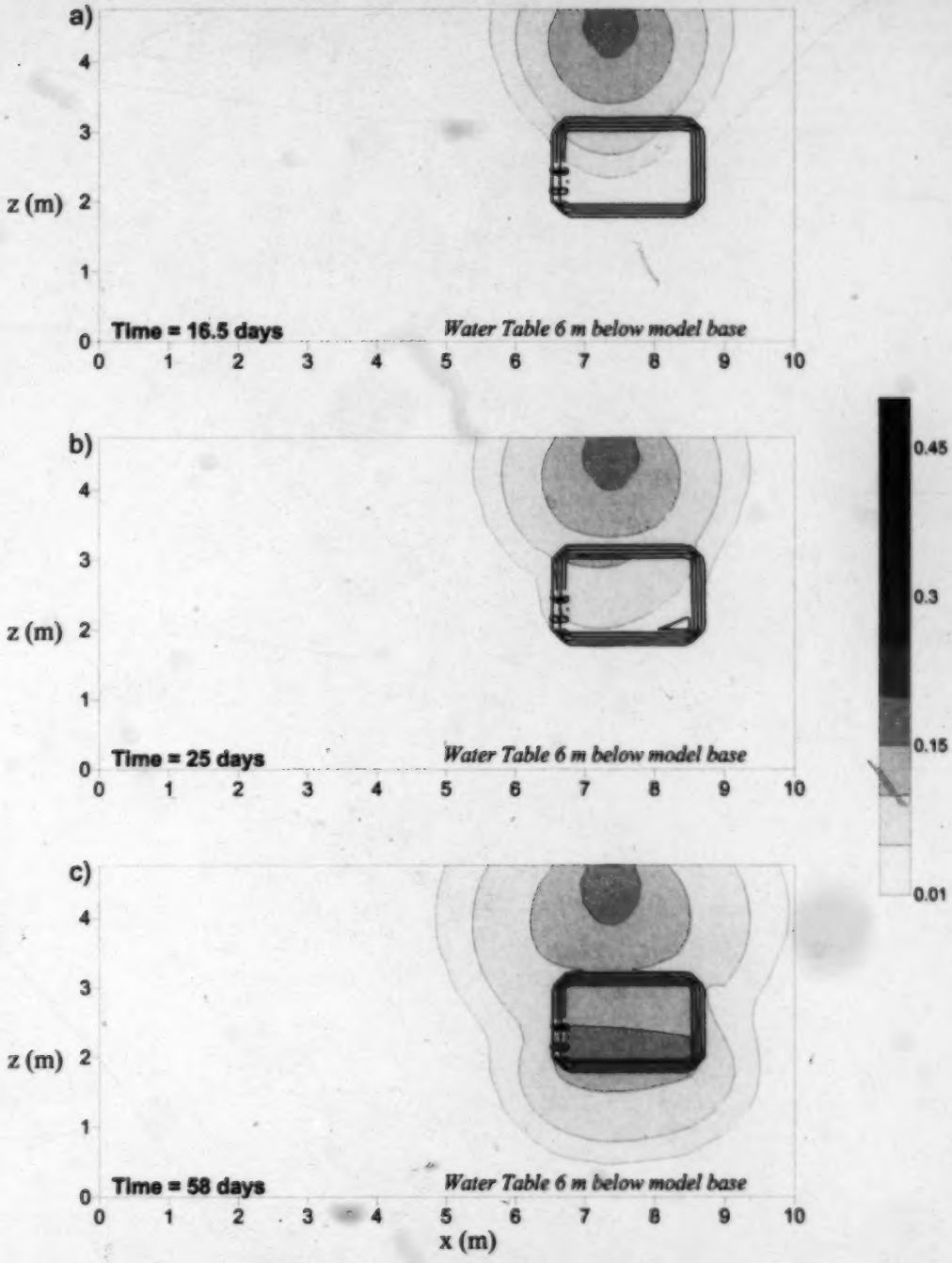

Figure 4.21. Fine-grained lens far above the water table: LNAPL and water saturation: a) 16.5 days; b) 25 days; c) 58 days

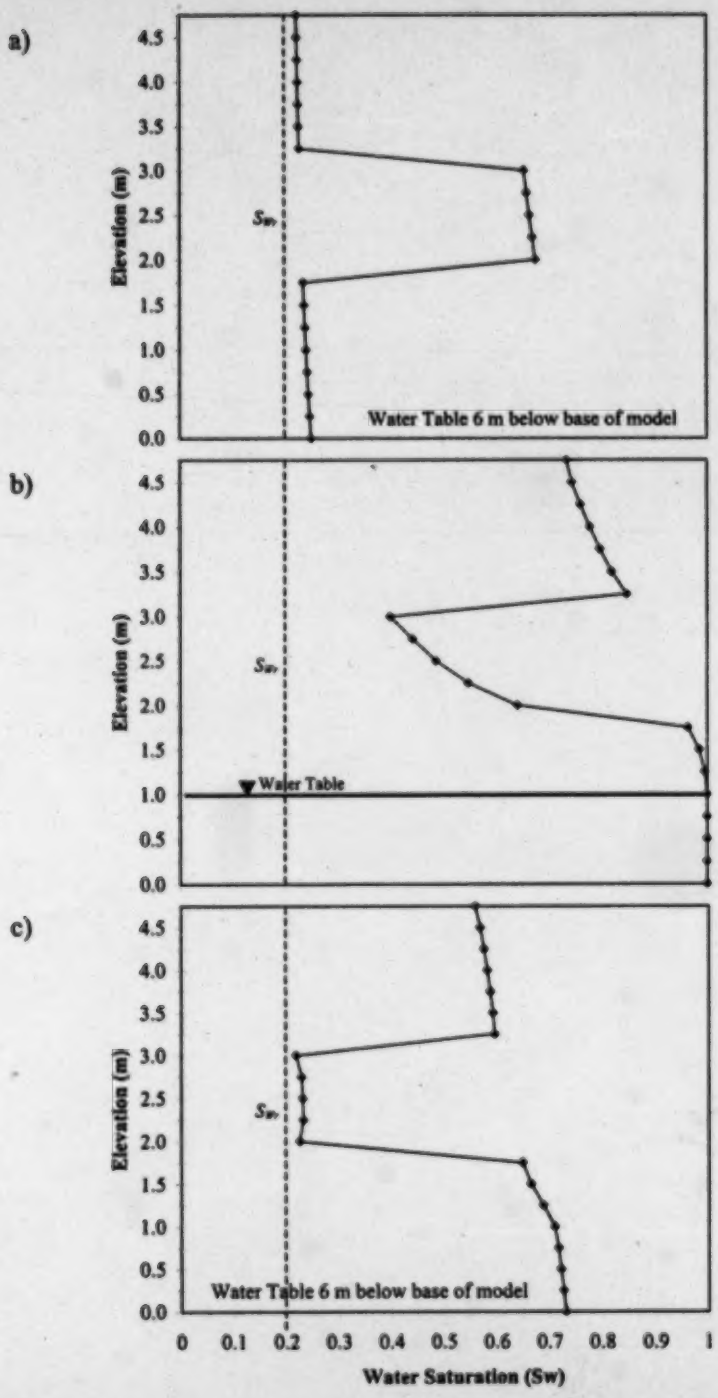

Figure 4.22. Initial water distribution: a) fine-grained lens high above water table; b) coarse-grained lens near water table; c) coarse-grained lens high above water table.

from the source area under gravity forces. However, bending of the LNAPL saturation contours is evident, near the top and sides of the lens, as the LNAPL preferentially flows into, rather than around, the fine-grained material. The fine-grained lens behaves as a sink for the LNAPL contaminant. A pool of higher LNAPL saturation also forms at the base of the fine-grained lens in this scenario.

Coarse-Grained Lenses

Similarly, the LNAPL migration behaviour in the presence of a coarse-grained lens is examined. In these two simulations the porous media properties are reversed from the previous example. Firstly, the case where the coarse material lens is close to the water table is examined. The water table is located 1 m above the bottom of the domain. In this case the initial water saturation (Figure 4.22b) is 0.38 at the top of the lens.

The resulting phase distributions are shown in Figure 4.23a, b, and c. It is apparent that the coarse-grained lens acts a sink, or trap, for the migrating LNAPL, by focusing flow into it. A pool forms at the base of the lens. The LNAPL can be seen to be moving into the lens, initially forming a slight pool at the top, and then migrating down to the based of the lens. A pool of LNAPL is visible at the base of the lens (Figure 4.23c) due to the presence of high water saturations in the fine-grained material beneath the lens. The distribution of trapped LNAPL shows a similar pattern, with the highest trapped saturations within the lens.

The results from a simulation with the same coarse-grained lens placed high above the water table are shown in Figure 4.24. In this case, the water table is again located 6 m below the base of the domain. The water saturations (Figure 4.22c) show the lens is significantly desaturated compared to the surrounding material: water saturations in the lens are approximately 0.22, while the matrix ranges from 0.56 to 0.73.

The simulation results shown in Figure 4.24 illustrates how the coarse-grained lens can act as a capillary barrier to LNAPL migration when it is sufficiently desaturated. As the infiltrating LNAPL reaches the top of the coarse grained lens, much of it is diverted t

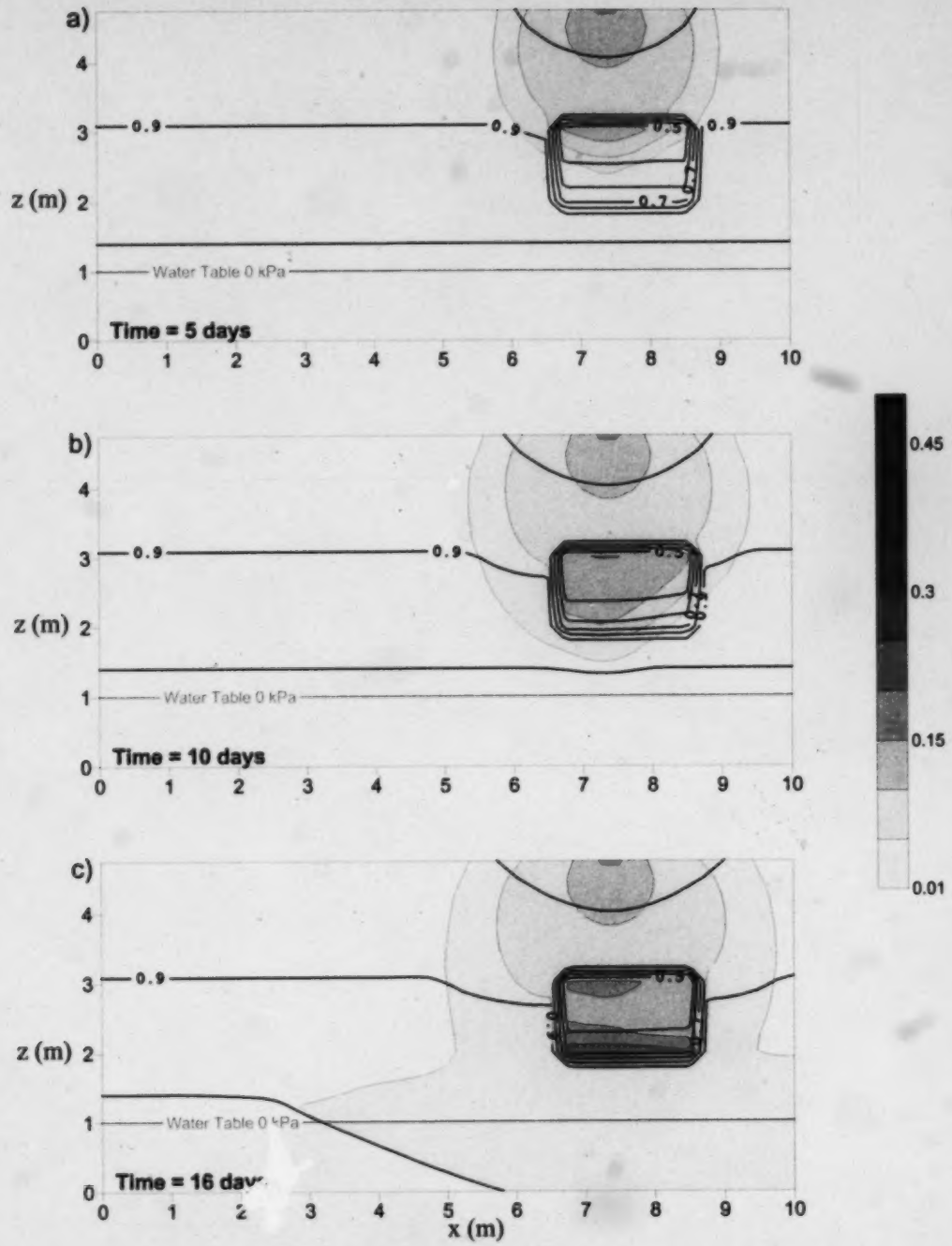

Figure 4.23. Coarse-grained lens near the water table: LNAPL and water saturation
a) 2 days; b) 5 days; c) 16 days

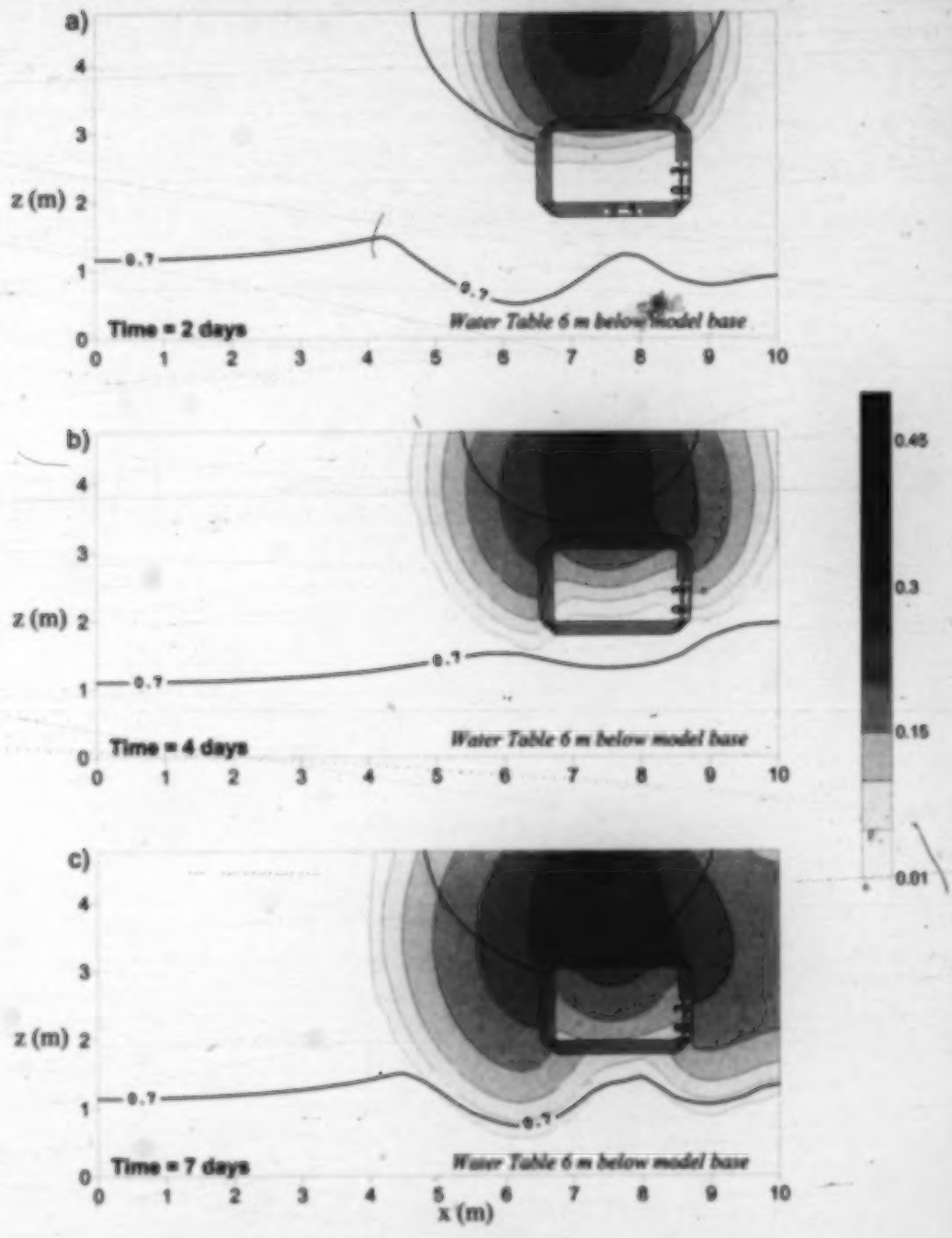

Figure 4.24. Coarse-grained lens high above the water table: LNAPL and water saturation at: a)2 days; b) 4 days; c) 7 days

laterally along the lens (Figure 4.24a). At 4 days (Figure 4.24b) the diversion is evident along the left side of the lens. Diversion is somewhat slower along the right side of the lens due to the effect of the no-flow boundary, which is evident by the slight buildup of water saturation near the lower right corner of the domain.

A large portion of the infiltrating LNAPL has been diverted around the sides of the lens, but some LNAPL has migrated into the lens (Figure 4.24c). Penetration of the lens is likely enhanced by two factors. Firstly, the interface between the lens and the surrounding porous medium is horizontal. If the interface was sloped or dome shaped, as is typical in natural settings, diversion might be enhanced. Here, the entire component of the gravity force on the LNAPL acts directly into the lens. Secondly, the use of the van Genuchten functional relationship for capillary pressure-saturation-relative permeability enhances penetration due to the lack of a distinct entry pressure.

4.3 DISCUSSION

The base case simulation presented above detailed the LNAPL behaviour during infiltration from a surface pool, and migration and trapping within the subsurface. It was shown that infiltrating LNAPL migrates down to the water table, causes depression of the water saturated region, and migrates laterally along the water table, under the influence of capillary forces and gravity due to the gradient of the water table. As the water table was lowered through the domain, the LNAPL migrated vertically as well as laterally, resulting in a laterally and vertically extensive region of trapped LNAPL saturation.

Factors such as the numerical model employed, a non-zero residual water saturation, the water table gradient, a falling water table, and heterogeneities were examined in a sensitivity analysis. Results of the simulation using NAPL Simulator showed that the overall migration and trapping behaviour during infiltration and redistribution above a falling water table is quite similar to that observed in the base case simulation using MOFAT. The simulation scenario employing a non-zero residual water saturation illustrated that lower LNAPL saturations are present and faster migration occurs, due to

the increased LNAPL effective saturations. Correspondingly, the trapped LNAPL saturations are reduced throughout the domain.

The water table gradient was shown to influence the lateral spreading and penetration of the water table by the LNAPL: lower gradients cause less lateral spreading and greater penetration. Conversely, a higher water table gradient will lead to more lateral spreading and less penetration. Lowering of the water table was shown to dramatically increase the vertical smearing of an LNAPL pulse.

The LNAPL migration behaviour in the vicinity of heterogeneities, either fine-grained or coarse-grained lenses, is dependent on the water table location relative to the lens. Either type of lens can as a barrier to LNAPL migration or as a sink with respect to the surrounding porous media, depending on the water saturation.

Heterogeneity Implications

These results clearly indicate that predicting LNAPL migration behaviour in the unsaturated zone based solely on soil type can result in incorrect conclusions. Lenses composed of coarser materials, like gravel, sand, or silt will not always act as conduits for free-phase migration. In cases where the water table is substantially below the lens position, resulting in water saturations near the irreducible water saturation, such lenses will acts as barriers to free-phase migration, diverting the LNAPL away from and around the lens through the finer soils surrounding the lens. Conversely, a lens composed of finer grained porous media can act as either a conduit or sink for free-phase migration when the water table is low.

Depending on the magnitude of seasonal water table fluctuation and the nature of the capillary pressure curve for the lens material, the behaviour of the lens could alternate between acting a conduit and acting as a barrier to free-phase migration. For instance, in the case of a coarse sand lens with a very abrupt capillary pressure curve and low entry pressure, water table fluctuations on the order of one or two metres could cause the migration potential of the lens to flip. Water table position at time of spill is important.

However, for old spills, the year of the spill, let alone the time of year the spill might have occurred is often unknown. Or for a site with multiple spills through time, one spill could be at a time of low water table and one could be at a time of high water table. This altered behaviour considerably increases the complexity of site investigations.

Direction of Water Table Fluctuation

The direction of water table movement is important for predicting the migration and degree of trapping of LNAPLs in the subsurface. In terms of a heterogeneous system, the direction controls whether a lens is water saturated when LNAPL reaches it or partially gas saturated. Combined with the importance of water saturation, illustrated above, and depending on the height of the LNAPL pancake and the contrast in capillary pressure parameters within the two media, a lens could act as either a barrier or a sink for the LNAPL phase.

Particularly with a rising water table, the top of water saturated region can move at different rates, as illustrated in Figure 4.25. Beneath the region of LNAPL contamination, the top of the water saturated region moves slower, compared to if the LNAPL was not present, due to the relative mobility of the gas and LNAPL phases. Down gradient of the spill, the water saturated region can rise faster, as the gas is more mobile than LNAPL. This process will retard the lateral spreading on the LNAPL during the period of rising water table.

A rising water table involves the water phase displacing the LNAPL upwards against gravity. Conversely, a falling water table involves the LNAPL simply following the water saturated region downwards, or falling with gravity

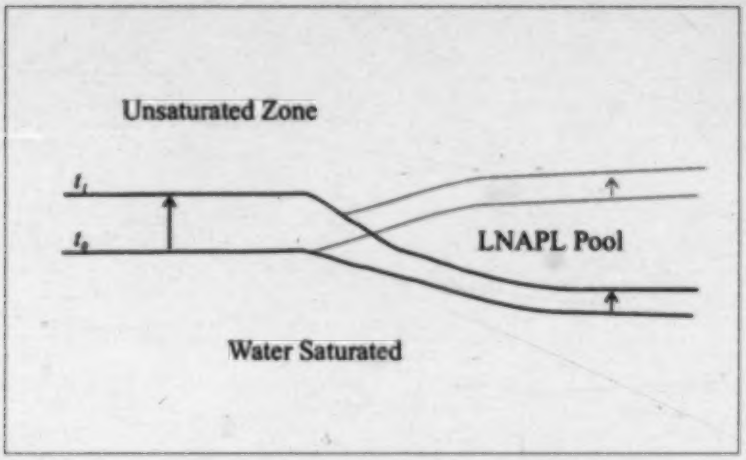

Figure 4.25. Differential upward movement of the water saturated region as the water table rises in the vicinity of a LNAPL pool.

Repetitive Cycles of Water Table Fluctuation

Repetitive cycles of water table fluctuation are extremely difficult to simulate numerically for three-phase flow due to mass balance issues. A falling water table is a situation of two two-phase flow regimes. At the top of the water saturated zone, the problem is one of water-LNAPL flow. At the top of the LNAPL zone, basically only LNAPL and gas are mobile. Changing the direction of water table movement results in changing the flow directions of all three phases, reversing from vertically down and laterally to vertically up and laterally. The situation of a rising water table also involves more regions of three-phase flow where the water, LNAPL, and gas are all mobile in the same location, which is numerically very difficult to simulate.

The influence of repetitive cycles of water table fluctuation will be to increase lateral spreading, increase the trapping of LNAPL, as the phase will be invading more pore regions not previously invaded. Trapping beneath water table, either as residual or as discontinuous larger bulbs due to minor heterogeneity will occur with rising water table conditions. All these changes in the flow patterns will act to spread out the region of trapped LNAPL saturation, and allow for more partitioning to the vapour and aqueous phases.

Chapter 5

Conclusions and Recommendations

The primary objective of this study was to examine the controls on the migration and trapping of light-non-aqueous-phase-liquids (LNAPL) in heterogeneous domains subjected to water table fluctuations. Cases of fractured porous media, homogeneous porous media, and lenses within porous media were considered.

Two finite-element numerical models were used to simulate the simultaneous flow of water, gas, and LNAPL under varying conditions. MOFAT was used to simulate the movement of these phases in a homogenous porous media domain, and then examine the impact of heterogeneity, water table location, and water table fluctuation parameters. NAPL Simulator was used as a comparison model and to examine the migration of LNAPL within a fracture network.

NAPL Simulator was used to study LNAPL migration in fractured porous media. The fractures were treated as one-dimensional porous media within the two-dimensional matrix, resulting in orthogonal bands of heterogeneity. Because nodal spacing across the fractures is much larger than the actual fracture aperture, the assigned permeabilities and porosities for the fracture were volume weighted to account for the volume differences. Furthermore, the capillary-pressure-saturation curve for the fractures was subdued compared to actual fracture curves, leading to a smaller change in saturation for a given

change in capillary pressure. This representation was employed because of the somewhat large nodal spacing necessary to simulate a domain of realistic size. These simulation results still capture the essence of the problem; however, these approximations manifest themselves by reducing LNAPL saturations within a given pore volume, resulting in lowering trapped saturations, and reducing LNAPL relative permeabilities.

Other modifications to the conceptual model were made that are specific to NAPL Simulator, but which would be advantageous in any attempt at representing fractures as one-dimensional porous media within a two-dimensional matrix under certain conditions. Specifically, these modifications can be employed when the phase of interest will be mostly constrained with the fracture network, and phase partitioning to matrix fluids is not being considered. Setting the matrix properties of porosity and permeability to the same as fractures results in a numerically simpler problem and faster solution, but does not significantly alter the LNAPL behaviour within the fracture planes. The aspect ratio was constrained to 1.0 due to an observed interaction between planes of heterogeneity and nodal numbering directions causing non-convergence behaviour on the pressure equation, a result of the numerical method used in NAPL Simulator.

A base case simulation was developed based on the Nordegg Gas Plant fractured aquifer. The 4.8 m by 4.8 m domain, rotated 30° from horizontal, contains two fracture sets. A water table is developed within the domain and LNAPL injected and allowed to redistribute. The base case simulation results show that LNAPL injected remains within the fracture network, even given the large saturation and pressure gradients between matrix and fractures. When the LNAPL is injected near the water table it migrates both up-dip and down-dip through fractures. Up-dip migration is stronger than down-dip migration due to buoyancy and the lower relative permeability. At fracture intersections, further migration is observed to occur through all segments, both up-dip and down-dip. By this process the LNAPL spreads laterally through the fracture network and penetrates beneath the water table.

The results from the simulations appear reasonable, but a significant mass balance error was observed in the NAPL Simulator results for the base case simulation. The error is systematic and consistently of the same sign for a given simulation. During the 80,000 seconds following injection, when the oil mass should be constant, the oil mass increased by 11%. The mass balance error responds to changes in the capillary pressure-saturation-relative permeability parameters, the magnitude of the small number cut-off in the code, and the solver choice; however, it can only marginally be improved.

The cause of this error appears to be a feature of the Hermite Collocation method employed within the NAPL Simulator, which imposes continuous gradients from node to node. In the problem being addressed, namely LNAPL migration in fractured porous media, the combination of a three-phase flow regime and the severe heterogeneity between the fractures and matrix means that there are numerous, expected, discontinuities in the gradients. As a result, the large mass balance error in the LNAPL phase develops.

LNAPL migration and trapping in porous media was examined using MOFAT and NAPL Simulator. The migration and trapping of LNAPLs in the subsurface is influenced by many factors. Trapped immobile LNAPL saturations are dependent on migration pathways. These factors emphasize the importance of quantifying heterogeneity and water table behaviour through time, and incorporating that knowledge into site investigations where LNAPL releases are suspected.

Numerical results of the homogeneous porous media base case simulation illustrated how LNAPL migrates predominantly vertically from the source to the water table, and then displaces the top of the water saturated region downwards. Once LNAPL reaches the water table, it moves laterally due to the water table gradient and capillary effects, becoming a lenticular shaped body. Lowering of the water table causes vertical spreading of the mobile LNAPL, in addition to the lateral spreading caused by the water table gradient and capillarity. This generates an extensive region of relatively low trapped LNAPL saturation, extending from above the initial water table location to slightly above the final water table location. Lateral fingering of the total LNAPL

saturation is present in the homogeneous domain, caused by the interplay of the trapped and mobile saturations.

Comparisons between the numerical results with MOFAT and NAPL Simulator show that the two models predict similar LNAPL distributions through time. The NAPL Simulator calculates less lateral spreading directly atop the water table, which is interpreted as a numerical error in MOFAT. The MOFAT solutions also have a higher LNAPL mass balance error, upwards of 13% after the 45 day simulation period, evident in the near source region later in the simulation period. The NAPL Simulator solutions have a LNAPL mass balance error of 2.5% after the same period of time.

Simulating a non-zero residual water saturation into the MOFAT model causes higher water saturations within the unsaturated zone than in the base case. The residual water saturation results in an increase in the effective LNAPL saturation, and faster lateral migration, lower LNAPL saturations, and, therefore, lower trapped LNAPL saturations.

Simulation results highlighted the importance of water table location history on the capillary behaviour of heterogeneities. Both fine-grained and coarse-grained lenses were shown to act as sinks for LNAPL, with respect to the surrounding porous medium, and as capillary barriers, depending on location of water table and contrast in capillary properties. A fine-grained lens, which typically acts as a barrier for LNAPL near the water table, located far above the water table acts instead as a trap for the migrating LNAPL. A coarse-grained lens, located far above the water table acts as a barrier to LNAPL migration, in contrast to the behaviour when the lens is near the water table and acting as a trap. As a result, the location of the water table at the time of a spill is crucial for determining migration pathways.

Simulation results showed that water table gradients of 0.005 and 0.0 did not produce substantially different solutions. This is partially due to the use of the van Genuchten model for capillary .pressure-saturation-relative permeability in the MOFAT model, which does not employ a displacement pressure term.

The importance of accounting for the lowering of the water table was illustrated in the modeling results. Compared to a falling water table condition, a static water table results in a much thinner, more laterally extensive migration pathway for the LNAPL, and therefore results in thinner, longer regions of trapped saturation. Increasing the rate of water table drop increases the vertical extent and decreases the lateral extent of contamination.

The direction of water table movement is also important for the migration of LNAPL. In the case of a dropping water table, LNAPL moves downwards under the influence of capillary and gravity forces. In the case of a rising water table, capillary forces push the LNAPL upwards, but gravity still acts downwards.

Depending on the contrast in capillary parameters between a lens and the surrounding porous medium, the lens can behave as either a sink or barrier, depending on the direction that the water table is moving. Repetitive cycles of water table fluctuation are difficult to simulate numerically, because changing the direction of water table movement results in changing the direction of LNAPL movement and because all three phases are mobile within the same pore volume. The influence of repetitive cycles is to increase lateral spreading, and increase the trapping of LNAPL, as the phase is invading more areas previously unoccupied.

Recommendations

A numerical model explicitly representing the fracture planes should be used for three-phase migrations studies of fractured aquifers. The representation as porous media is inherently difficult, and numerical models not written specifically for the task are likely to have problems. Development of a problem specific numerical model, although more time intensive, would result in more accurate and representative simulation results. Discretization requirements in such a scenario would be onerous.

The Hermite Collocation method, and numerical models employing this method, should be avoided when heterogeneity and / or multiphase flow problems are being addressed.

References

Abdul, A.S., 1988. Migration of petroleum products through sandy hydrogeologic systems. *Groundwater Monitoring Review*, **8**(4), 73-81.

Anderson, M.P. and Woessner, W.W., 1992. *Applied Groundwater Modeling: Simulation of Flow and Advective Transport*. Academic Press, Inc., Academic Press, Inc.

Andersson, J. and Dverstorp, B., 1987. Conditional simulations of fluid flow in three-dimensional networks of discrete fractures. *Water Resources Research*, **23**(10), 1876-1886.

Barenblatt, G.I., Zheltov, I.P. and Kochina, I.N., 1960. Basic concepts in the theory of seepage of homogeneous liquids in fissured rock (strata). *PMM*, **24**(5), 1286-133.

Bear, J., 1972. *Dynamics of fluids in porous media*. Dover Publications, Inc., Dover Publications, Inc., 764.

Bear, J., 1993. Modeling flow and contaminant transport in fractured rock. In: Bear, J., Tsang, C. and de Marsily, G. (Eds), Flow and contaminant transport in fractured rock. Academic Press, Inc., Academic Press, Inc., 1-37.

Brooks, R.H. and Corey, A.T., 1964. Hydraulic properties of porous media. Colorda State Univeristy Hydrology Paper, Colorda State Univeristy Hydrology Paper, 27.

Brown, S.R., 1987. Fluid flow through rock joints: The effect of surface roughness. *Journal of Geophysical Research*, **92**(B2), 1337-1347.

Cacas, M.C., Ledoux, E., de Marsily, G., Barbreau, A., Calmels, P., Gaillard, B. and Margritta, R., 1990a. Modeling fracture flow with a stochastic discrete fracture network: Calibration and validation 1.The transport model. *Water Resources Research*, **26**(3), 479-489.

Cacas, M.C., Ledoux, E., de Marsily, G., Tillie, B., Barbreau, A., Durand, E., Feuga, B. and Peaudecerf, P., 1990b. Modeling fracture flow with a stochastic discrete fracture network: Calibration and validation 1.The flow model. *Water Resources Research*, **26**(3), 479-489.

Corey, A.T., 1994. *Mechanics of Immiscible Fluids in Porous Media*. Water Resources Publications, Water Resources Publications, 252.

David, T.W., Michener, S.R., Dolan, T.J. and Cavagrotti, R.R., 1999. An integrated approach to the characterization and remediation of gasoline in a fractured, sedimentary bedrock setting. *Proceedings of the 2000 petroleum hydrocarbons and organic chemicals in ground water; prevention, detection, and remediation conference and exposition*, 316-330.

Dullien, F.A.L., 1992. *Porous Media: Fluid Transport and Pore Structure*. Academic Press, Inc., Academic Press, Inc., 574.

Dyksen, W.R. and Rice, J.R., 1986. The importance of scaling for the Hermite bicubic collocation equations. *SIAM Journal on Scientific and Statistical Computing*, 7707-719.

Esposito, S.J. and Thomson, N.R., 1999. Two-phase flow and transport in a single fracture-porous medium system. *Journal of Contaminant Hydrology*, **37**, 319-341.

Essaid, H.I., Herkelrath, W.N. and Hess, K.M., 1993. Simulation of fluid distributions observed at a crude oil spill site incorporating hysteresis, oil entrapment, and spatial variability of hydraulic properties. *Water Resources Research*, **29**(6), 1753-1770.

Feenstra, S., Cherry, J.A. and Parker, B.L., 1996. Conceptual Models for the Behaviour of Dense Non-Aqueous Phase Liquids (DNAPLs) in the Subsurface. In: Pankow, J.F. and Cherry, J.A. (Eds), Dense Chlorinated Solvents and other DNAPLs in Groundwater. Waterloo Press, Waterloo Press, 53-88.

Fetter, C.W., 1999. *Contaminant Hydrogeology*. Prentice Hall, Prentice Hall, 500.

Freeze, R.A. and Cheery, J.A., 1979. *Groundwater*. Prentice-Hall, Inc., Prentice-Hall, Inc.

Fung, L.S.K., 1991. Simulation of block-to-block processes in naturally fractured reservoirs. *SPE Reservoir Engineering*, **6**(Nov), 477-484.

Ge, S., 1997. A governing equation for fluid flow in rough fractures. *Water Resources Research*, **33**(1), 53-61.

Guarnaccia, J., Pinder, G. and Fishman, M., 1997. NAPL : Simulator Documentation. U.S. Environmental Protection Agency, Office of Research and Development, U.S. Environmental Protection Agency, Office of Research and Development.

Hardisty, P.E., 1996. Characterization, occurrence and behaviour of light nonaqueous phase liquids in fractured rocks. Ph.D. Thesis, University of London, 240 pp.

Hardisty, P.E. and Johnston, P.M., 1993. Characterization of occurrence and distribution of LNAPL in fractured rocks. *Ground Water Management*, **17**, 113-129.

Hardisty, P.E., Ross, S.D., Dabrowski, T.L. and Brown, A., 1995. Remediation of LNAPL in fractured rock: Theory and application. *Proceedings, International Association of Hydrogeologists 1995 congress*, no pages numbers. Edmonton, AB.

Hardisty, P.E., Ross, S.D. and Johnston, P.M., 1994a. Characterization of LNAPL in fractured sedimentary rock: Techniques, behaviour, and implications for remediation. *4th Annual Symposium on Groundwater and Soil Remediation, GASReP*. Calgary, AB.

Hardisty, P.E., Wheater, H., Johnston, P.M. and Dabrowski, T.L., 1994b. Mobility of LNAPL in fractured sedimentary rocks: Implications for remediation. *API/NGWA Conference on Hydrocarbons and Organic Chemicals in Groundwater*, 473-493. Houston, TX.

Hardisty, P.E., Wheater, H.S., Johnson, P.M. and Bracken, R.A., 1998. Behaviour of light immiscible liquid contaminants in fractured aquifers. *Geotechnique*, **48**(6), 747-760.

Harrison, B., Sudicky, E.A. and Cherry, J.A., 1992. Numerical analysis of solute migration through fractured clayey deposits into underlying aquifers. *Water Resources Research*, **28**(2), 515-526.

Heise, M.D., 1999. Simulation of coupled aqueous and non-aqueous phase flow and transport in a fracture. M.Sc. Thesis, University of Alberta, 114 pp.

Kaluarachchi, J.J. and Parker, J.C., 1992. Multiphase flow with a simplified model for oil entrapment. *Transport in Porous Media*, **7**, 1-14.

Katyal, A.K., Kaluarachchi, J.J. and Parker, J.C., 1991. MOFAT: A two-dimensional finite-element program for multiphase flow and multicomponent transport. U.S. Environmental Protection Agency, U.S. Environmental Protection Agency.

Kazemi, H. and Gilman, J.R., 1993. Multiphase flow in fractured petroleum reservoirs. In: Bear, J., Tsang, C. and de Marsily, G. (Eds), Flow and contaminant transport in fractured rock. Academic Press, Inc., Academic Press, Inc., 267-323.

Kemblowski, M.W. and Chiang, C.Y., 1990. Hydrocarbon thickness fluctuations in monitoring wells. *Ground Water*, **28**(2), 244-252.

Kueper, B.H. and McWhorter, D.B., 1991. The behaviour of dense, non-aqueous phase liquids in fractured clay and rock. *Ground Water*, **29**(5), 716-728.

Kueper, B.H. and McWhorter, D.B., 1996. Physics Governing the Migration of Dense Non-Aqueous Phase Liquids (DNAPLs) in Fractured Media. In: Pankow, J.F. and Cherry, J.A. (Eds), Dense Chlorinated Solvents and other DNAPLs in Groundwater. Waterloo Press, Waterloo Press, 89-128.

Land, C.S., 1968. Calculation of imbibition relative permeability for two- and three-phase flow from rock properties. *Society of Petroleum Engineers Journal*, **243**, 149-156.

Lenhard, R.J., Johnson, T.G. and Parker, J.C., 1993. Experimental observations of nonaqueous-phase liquid subsurface movement. *Journal of Contaminant Hydrology*, **12**, 79-101.

Lenhard, R.J. and Parker, J.C., 1987. A model for hysteretic constitutive relations governing multiphase flow 2. Permeability-saturation relations. *Water Resources Research*, **23**(12), 2197-2206.

Leverett, M.C., 1941. Capillary behaviour in porous media. *Trans. AIME*, **142**, 152-169.

Leverett, M.C. and Lewis, W.B., 1941. Steady flow of gas-oil-water mixtures through unconsolidated sands. *Trans. Soc. Pet. Eng. AIME*, **142**, 107-116.

Long, J.C.S., J.S., R., Wilson, C.R. and Witherspoon, P.A., 1982. Porous media equivalents for networks of discontinuous fractures. *Water Resources Research*, **18**(3), 645-658.

Mayer, A.S., Mitchell, R.J., Carriere, P.P.E., Hein, G.L., Rabideau, A.J. and Wojick, C.L., 1995. Groundwater quality. *Water Environment Research*, **67**(4), 629-685.

McCrory, T.A., 1997. Fracture control of free-product migration at an emergency response, Blue Ridge, Georgia. *Abstracts with Programs - Geological Society of America*, **29**(6), 386-387.

Mercer, J.W. and Cohen, R.M., 1990. A review of immiscible fluids in the subsurface: Properties, models, characterization, and remediation. *Journal of Contaminant Hydrology*, **6**, 107-163.

Minssieux, L., 1994. Hysteresis effects in water/gas flow in porous media. *Computational Methods in Water Resources X*, 959-966. Heidelberg, Federal Republic of Germany.

Mualem, Y. and Dagan, G., 1975. A dependent domain model of capillary hysteresis. *Water Resources Research*, **11**(3), 452-460.

Oostrom, M. and Lenhard, R.J., 1998. Comparison of relative permeability-saturation-pressure parametric models for infiltration and redistribution of a light nonaqueous-phase liquid in a sandy porous media. *Advances in Water Resources*, **21**(2), 145-157.

Parker, B.L., Gillham, R.W. and Cherry, J.A., 1994. Diffusive disappearance of immiscible-phase organic liquids in fractured geologic media. *Ground Water*, **32**(5), 805-820.

Parker, J.C., 1989. Mulitphase flow and transport in porous media. *Reviews of Geophysics*, **27**(3), 311-328.

Parker, J.C., Katyal, A.K. and Zhu, J.L., 1991. Free product recovery with fluctuating water tables. *Ground Water Management*, **5**, 291-305.

Parker, J.C. and Lenhard, R.J., 1987. A model for hysteretic constitutive relations governing multiphase flow. 1. Saturation-Pressure Relations. *Water Resources Research*, **23**(12), 2187-2196.

Parker, J.C., Lenhard, R.J. and Kuppusamy, T., 1987. A parametric model for constitutive properties governing multiphase flow in porous media. *Water Resources Research*, **23**(4), 618-624.

Peng, C.P., Yanosik, J.L. and Stephenson, R.E., 1990. A generalized compositional model for naturally fractured reservoirs. *SPE Reservoir Engineering*, **5**(May), 221-226.

Persoff, P. and Pruess, K., 1995. Two-phase flow visualization and relative permeability measurements in natural rough-walled rock fractures. *Water Resources Research*, **31**(5), 1175-1186.

Pruess, K. and Tsang, Y.W., 1990. On two-phase relative permeability and capillary pressure of rough-walled rock fractures. *Water Resources Research*, **26**(9), 1915-1926.

Reitsma, S. and Kueper, B.H., 1994. Laboratory measurement of capillary pressure - saturation relationships in a rock fracture. *Water Resources Research*, **30**(4), 865-878.

Rossen, R.H. and Shen, E.I.C., 1989. Simulation of gas/oil drainage and water/oil imbibition in naturally fractured reservoirs. *SPE Reservoir Engineering*, 4(Nov), 464-470.

Schroth, M.H., Istok, J.D. and Selker, J.S., 1998a. Three-phase immiscible fluid movement in the vicinity of textural interfaces. *Journal of Contaminant Hydrology*, 32, 1-23.

Schroth, M.H., Istok, J.D., Selker, J.S., Oostrom, M. and White, M.D., 1998. Multifluid flow in bedded porous media: laboratory experiments and numerical simulations. *Advances in Water Resources*, 22(2), 169-183.

Schwartz, F.W. and Smith, L., 1988. A continuum approach for modeling mass transport in fractured media. *Water Resources Research*, 24(8), 136-1372.

Schwille, F., 1988. *Dense chlorinated solvents in porous and fracture media: Model experiments*. Lewis Publishers, Inc., Lewis Publishers, Inc.

Slough, K.J., Sudicky, E.A. and Forsyth, P.A., 1999. Importance of rock matrix entry pressure on DNAPL migration in fractured geologic materials. *Ground Water*, 37(2), 237-244.

Steffy, D.A., Johnston, C.D. and Barry, D.A., 1995. A field study of the vertical immiscible displacement of LNAPL associated with a fluctuating water table. *Groundwater Quality: Remediation and Protection*, 49-57. Prague.

Sudicky, E.A. and McLaren, R.G., 1992. The Laplace transform galerkin technique for large-scale simulation of mass transport in discretely fractured porous formations. *Water Resources Research*, 28(2), 499-514.

Sullivan, C.R., Zinner, R.E. and Hughes, J.P., 1988. The occurence of hydrocarbon on an unconfined aquifer and implications for liquid recovery. *Conference on Petroleum Hydrocarbons and Organic Chemicals in Groundwater*, 135-155. Houston, TX.

Therrien, R. and Sudicky, E.A., 1996. Three-dimensional analysis if variably-saturated flow and solute transport in discretely-fractured porous media. *Journal of Contaminant Hydrology*, 23, 1-44.

Tidwell, V.C. and Glass, R.J., 1995. Laboratory investigation of matrix imbibition from a flowing fracture. *Geophysical Research Letters*, **22**(11), 1405-1408.

van Genuchten, M.T., 1980. A closed-form equation for predicting the hydraulic conductivity of unsaturated soils. *Soil Science Society of America Journal*, **44**, 892-898.

Wang, J.S.Y. and Narasimhan, T.N., 1985. Hydrologic mechanisms governing fluid flow in a partially saturated, fractured, porous media. *Water Resources Research*, **21**(12), 1861-1874.

Warren, J.E. and Root, P.J., 1963. The behaviour of naturally fractured reservoirs. *Society of Petroleum Engineers Journal*, **3**, 245-255.

White, M.D. and Lenhard, R.J., 1993. Numerical analysis of a three-phase system with a fluctuating water table. *13th Annual AGU Hydrology Days*, 219-236. Colorado State University, Fort Collins, CO.

Witherspoon, P.A., Wang, J.S.Y., Iwai, K. and Gale, J.E., 1980. Validity of cubic law for fluid flow in a deformable rock fracture. *Water Resources Research*, **16**(6), 1016-1024.